

Partonic Structure of Light Nuclei

W. R. Armstrong, J. Arrington, I. Cloët, K. Hafidi[†], M. Hattawy[†], D. Potterveld,
P. Reimer, S. Riordan, Z. Yi

Argonne National Laboratory, Lemont, IL 60439, USA

J. Ball, M. Defurne, M. Garçon, H. Moutarde, S. Procureur, F. Sabatié
CEA, Centre de Saclay, Irfu/Service de Physique Nucléaire, 91191 Gif-sur-Yvette, France

W. Cosyn

*Department of Physics and Astronomy, Proeftuinstraat 86, Ghent University, 9000 Ghent,
Belgium*

M. Mazouz

Faculté des Sciences de Monastir, 5000 Tunisia

J. Bettane, R. Dupré[†], M. Guidal, D. Marchand, C. Muñoz, S. Niccolai, E. Voutier
*Institut de Physique Nucléaire, CNRS-IN2P3, Univ. Paris-Sud, Université Paris-Saclay,
91406 Orsay Cedex, France*

K. P. Adhikari, J. A. Dunne, D. Dutta, L. El Fassi, L. Ye
Mississippi State University, Mississippi State, MS 39762, USA

M. Amarian, G. Charles, G. Dodge

Old Dominion University, Norfolk, VA 23529, USA

V. Guzey

*Petersburg Nuclear Physics Institute, National Research Center "Kurchatov Institute",
Gatchina, 188300, Russia*

N. Baltzell[†], F. X. Girod, S. Stepanyan

Thomas Jefferson National Accelerator Facility, Newport News, VA 23606, USA

[†]Spokesperson

B. Duran, S. Joosten, Z.-E. Meziani[‡], M. Paolone[†], M. Rehfuss, N. Sparveris
Temple University, Philadelphia, PA 19122, USA

F. Cao, K. Joo, A. Kim, N. Markov
University of Connecticut, Storrs, CT 06269, USA
S. Scopetta
Università di Perugia, INFN, Italy

W. Brooks, A. El-Alaoui
Universidad Técnica Federico Santa María, Valparaíso, Chile

S. Liuti
University of Virginia, Charlottesville, VA 22903, USA

a CLAS Collaboration Proposal

[‡]Contact person

Nuclear Exclusive and Semi-inclusive Measurements with a New CLAS12 Low Energy Recoil Tracker

ALERT Run Group[†]

EXECUTIVE SUMMARY

In this run group, we propose a comprehensive physics program to investigate the fundamental structure of the ^4He nucleus. An important focus of this program is on the coherent exclusive Deep Virtual Compton Scattering (DVCS) and Deep Virtual Meson Production (DVMP) with emphasis on ϕ meson production. These are particularly powerful tools enabling model-independent nuclear 3D tomography through the access of partons' position in the transverse plane. These exclusive measurements will give the chance to compare directly the quark and gluon radii of the helium nucleus. Another important measurement proposed in this program is the study of the partonic structure of bound nucleons. To this end, we propose next generation nuclear measurements in which low energy recoil nuclei are detected. The tagging of recoil nuclei in deep inelastic reactions is a powerful technique, which will provide unique information about the nature of medium modifications through the measurement of the EMC ratio and its dependence on the nucleon off-shellness. Finally, we propose to measure incoherent spectator-tagged DVCS on light nuclei (d, ^4He) where the observables are sensitive to the Generalized Parton Distributions (GPDs) of a quasi-free neutron for the case of the deuteron, and bound proton and neutron for the case of ^4He . The objective is to study and separate nuclear effects and their manifestation in GPDs. The fully exclusive kinematics provide a novel approach for studying final state interactions in the measurements of the beam spin asymmetries and the off-forward EMC ratio.

At the heart of this program is the Low Energy Recoil Tracker (ALERT) combined with the CLAS12 detector. The ALERT detector is composed of a stereo drift chamber for track reconstruction and an array of scintillators for particle identification. Coupling these two types of fast detectors will allow ALERT to be included in the trigger for efficient

[†]Contact Person: Kawtar Hafidi (kawtar@anl.gov)

background rejection, while keeping the material budget as low as possible for low energy particle detection. ALERT will be installed inside the solenoid magnet instead of the CLAS12 Silicon Vertex Tracker and Micromegas tracker. We will use an 11 GeV longitudinally polarized electron beam (80% polarization) of up to 1000 nA on a gas target straw filled with deuterium or ^4He at 3 atm to obtain a luminosity up to 6×10^{34} nucleon $\text{cm}^{-2}\text{s}^{-1}$. In addition we will need to run hydrogen and ^4He targets at different beam energies for detector calibration. The following table summarizes our beam time request:

Configurations	Proposals	Targets	Beam time request	Beam current	Luminosity*
			days	nA	$\text{n}/\text{cm}^2/\text{s}$
Commissioning	All [†]	^1H , ^4He	5	Various	Various
A	Nuclear GPDs	^4He	10	1000	6×10^{34}
B	Tagged EMC & DVCS	^2H	20	500	3×10^{34}
C	All [†]	^4He	20	500	3×10^{34}
TOTAL			55		

*This luminosity value is based on the effective part of the target. When accounting for the target's windows, which are outside of the ALERT detector, it is increased by 60%.

[†]“All” includes the four proposals of the run group: Nuclear GPDs, Tagged EMC, Tagged DVCS and Extra Topics. Note that the beam time request is only driven by the three first proposals.

Abstract

We propose to study the partonic structure of ${}^4\text{He}$ by measuring the Beam Spin Asymmetry (BSA) in coherent Deeply Virtual Compton Scattering (DVCS) and the differential cross-section of the Deeply Virtual Meson Production (DVMP) of the ϕ . Despite its simple structure, a light nucleus such as ${}^4\text{He}$ has a density and a binding energy comparable to that of heavier nuclei. Therefore, by studying ${}^4\text{He}$ nucleus, one can learn typical features of the partonic structure of atomic nuclei. In addition, due to its spin-0, only one chiral-even GPD, H_A , parameterizes the ${}^4\text{He}$ partonic structure at twist-2 allowing for a much simpler extraction of its tomography from data.

A major goal of this proposal is to cover a wide kinematical range and collect high statistics leveraging the knowledge obtained during the CLAS experiment E08-024 (eg6 run), where, for the first time, exclusive coherent DVCS off ${}^4\text{He}$ was successfully measured. The real and imaginary parts of the ${}^4\text{He}$ Compton form factors (CFFs) will be extracted in a model independent way from the experimental asymmetries, allowing us to access the nuclear transverse spatial distributions of quarks.

An equally important focus of this proposal is to study the gluonic structure of nuclei through the measurement of exclusive coherent ϕ meson electroproduction off a ${}^4\text{He}$ target. The kinematic regime to be explored includes very low $|t|$ up to the first diffractive minimum as found in elastic scattering off ${}^4\text{He}$ ($|t'| \simeq 0.6 \text{ GeV}^2$). The ϕ meson will be detected primarily through the charged K^+K^- channel, with the neutral $K_S^0K_L^0$ channel also available through $K_S \rightarrow \pi^+\pi^-$. Differential cross-sections for ϕ electroproduction off ${}^4\text{He}$ will be measured for the first time.

The combination of CLAS12 and the ALERT detector provides a unique opportunity to study both the quark and gluon structure of a dense light nucleus. Coherent exclusive DVCS off ${}^4\text{He}$ will probe the transverse spatial distribution of quarks in the nucleus as a function of the quarks' longitudinal momentum fraction, x . In parallel, the average spatial transverse gluon density of the ${}^4\text{He}$ nucleus will be extracted within a GPD framework using the measured longitudinal cross-section of coherent ϕ production in a similar range of longitudinal momentum x as that of the quarks. Additionally, threshold effects of ϕ production can be explored by exploiting the ALERT detector's large acceptance for low $|t|$ events.

Contents

Abstract	5
Introduction	8
1 Physics Motivations	10
1.1 DVCS Measurement	10
1.2 Deep Virtual ϕ Production Measurement	12
2 Formalism and Experimental Observables	14
2.1 Generalized Partons Distributions	14
2.2 Coherent DVCS	16
2.2.1 Accessing the Quark GPD	16
2.2.2 Experimental Status	19
2.3 Coherent ϕ Production	25
2.3.1 Accessing the Gluon GPD	25
2.3.2 Experimental Status	26
3 Experimental Setup	28
3.1 The CLAS12 Spectrometer	29
3.2 Available options for a Low Energy Recoil Detector	29
3.2.1 CLAS12 Central Detector	31
3.2.2 BONuS12 Radial Time Projection Chamber	31
3.2.3 Summary	33
3.3 Design of the ALERT Detector	33
3.3.1 The Drift Chamber	34
3.3.2 The Scintillator Array	39
3.3.3 Target Cell	41
3.4 Simulation of ALERT and reconstruction	43
3.4.1 Simulation of ALERT	43
3.4.2 Track Fitting	43
3.4.3 Particle identification in ALERT	44
3.5 Drift chamber prototype	47

3.6	Technical contributions from the research groups	48
3.6.1	Argonne National Laboratory and Temple University	50
3.6.2	Institut de Physique Nucléaire d'Orsay	50
3.6.3	Jefferson Laboratory	51
4	Proposed Measurements	52
4.1	Exclusive Coherent DVCS	52
4.1.1	Event Generator	60
4.1.2	Projections	61
4.1.3	Systematic uncertainties	63
4.2	Exclusive ϕ Electroproduction	67
4.2.1	Production and Background Rates	67
4.2.2	Event Generator	70
4.2.3	Projections	71
4.3	Parton Distributions in the Transverse plane	74
	Summary and Answers to PAC44	77
	Answer to PAC44 issues	77
	Summary and Beam Time Request	80
	Relation to other proposals	81
A	Twist-2 $e^4He \rightarrow e^4He \gamma$ cross section	82
B	Projections using Bethe-Heitler cross sections	85

Introduction

The general evidence on nuclei strongly supports the view that the α particle is of primary importance as a unit of the structure of nuclei in general and particularly of the heavier elements. It seems very possible that the greater part of the mass of heavy nuclei is due to α particles which have an independent existence in the nuclear structure.

— Rutherford, Chadwick, and Ellis (1930)
Radiations from Radioactive Substances^a

^aThis was the first textbook on nuclear physics and notably published two years before the discovery of the neutron.

Inclusive deep inelastic scattering (DIS) experiments have been instrumental in advancing our understanding of the QCD structure of nuclei and the effect of nuclear matter on the structure of hadrons. A great example is the observation by the European Muon Collaboration (EMC) of a deviation of the deep inelastic structure function of a nucleus from the sum of the structure functions of the free nucleons, the so-called EMC effect [1]. It became clear that even in a DIS process characterized by high locality of the probe-target interaction region, a different picture emerges from the nucleus other than a collection of quasi-free nucleons. On the theory side, despite decades of theoretical efforts [2, 3, 4, 5, 6] with increased sophistication, a unifying physical picture of the origin of the EMC effect is still a matter of intense debate. To reach the next level of our understanding of nuclear QCD and unravel the partonic structure of nuclei, experiments need to go beyond the inclusive measurements and focus on exclusive and semi-inclusive reactions.

Hard exclusive experiments such as Deep Virtual Compton Scattering (DVCS) and Deep Virtual Meson Production (DVMP) provide an important new probe that will allow us to discern among the different interpretations of nuclear effects on the structure of embedded nucleons in the nuclear medium. By introducing a new framework to describe both the intrinsic motion of partons and their transverse spatial structure in nuclei [4, 5, 6, 7, 8, 9], valuable information can be obtained from the measurement of the nuclear Generalized Parton Distributions (GPDs) representing the soft matrix elements for these processes. The GPDs correspond to the coherence between quantum states of different (or same) helicity, longitudinal momentum, and transverse position. In an impact parameter space,

they can be interpreted as a distribution in the transverse plane of partons carrying a certain longitudinal momentum [10, 11, 12]. A crucial feature of GPDs is the access to the transverse position of partons which, combined with their longitudinal momentum, leads to the total angular momentum of partons [13]. This information is not accessible to inclusive DIS which measures probability amplitudes in the longitudinal plane.

A high luminosity facility such as Jefferson Lab offers a unique opportunity to map out the three-dimensional quark and gluon structure of nucleons and nuclei. While most of submitted proposals to JLab Program Advisory Committee (PAC) have focused on the studies of the 3D nucleon structure considered as one of the main motivations for the JLab 12 GeV upgrade, we propose here to extend the measurements to light nuclei. While this proposal focuses on ${}^4\text{He}$ nucleus, we also plan to measure few deuteron GPDs¹. Pioneering measurements of exclusive coherent DVCS off ${}^4\text{He}$ have been successfully conducted during the JLab 6 GeV era (E08-024) using the CLAS detector enhanced with the radial time projection chamber (RTPC) for the detection of low energy recoils and the inner calorimeter for the detection of forward high energy photons. However, the experiment covered only limited kinematic range and the results were dominated by statistical uncertainties [14].

We propose a new measurement of hard exclusive DVCS and deeply virtual ϕ production off ${}^4\text{He}$ nuclei. The focus of this proposal is on the coherent DVCS (DVMP) channel where the scattered electron, the produced photon (the ϕ meson) and the recoil ${}^4\text{He}$ are all detected in the final state. We propose to use CLAS12 because of its large acceptance. In addition to the coherent DVCS and DVMP off ${}^4\text{He}$, the CLAS12-ALERT setup will allow us to mine the data collected in this experiment for other final states as well, such as the π^0 , ρ and ω mesons and other reaction channels described in the accompanying proposals of the ALERT run group¹. The novelty of the proposed measurements is the use of a new low energy recoil tracker (ALERT) in addition to CLAS12. The ALERT detector is composed of two types of fast detectors: a stereo drift chamber for track reconstruction and an array of scintillators for particle identification. ALERT will be included in the trigger for efficient background rejection, while keeping the material budget as low as possible to detect low energy particles. This was not possible with the previous GEM based RTPC due to the long drift time.

¹See the 4th proposal of the ALERT run group which summarizes additional measurements we plan to perform with no additional beam time.

Chapter 1

Physics Motivations

A wealth of information on the QCD structure of hadrons lies in the correlations between the momentum and spatial degrees of freedom of the constituent partons. Such correlations are accessible via GPDs which, more specifically, describe the longitudinal momentum distribution of a parton located at any given position in the plane transverse to the longitudinal momentum of the fast moving nucleon. Various GPDs extracted from measurements of hard exclusive reactions with various probe helicities and target spin configurations are necessary to identify this subset of the hadronic phase-space distribution, known as the Wigner distribution. The processes which are most directly related to GPDs are DVCS and DVMP corresponding to the exclusive electroproduction of a real photon or a meson in the final state respectively, see Figure 1.1.

The number of GPDs needed to parametrize the partonic structure of a nucleus depends on the different configurations between the spin of the nucleus and the helicity direction of the struck quark. For example, for a target of spin s , the number of chiral-even GPDs is equal to $(2s + 1)^2$ for each quark flavor. DVCS off spin 0 nuclear targets, such as ${}^4\text{He}$, is simpler to study since only one chiral-even GPD, H_A , is present at leading twist.

The ${}^4\text{He}$ nucleus is a well studied few-body system in standard nuclear physics. It is characterized by a strong binding energy and relatively high nuclear core density similar to some more complex nuclei. Inclusive scattering off ${}^4\text{He}$ shows a large EMC effect. By measuring quark and gluon GPDs in nuclei, one also accesses transverse spatial degrees of freedom, by which one can infer space dependent nuclear modifications directly from data.

1.1 DVCS Measurement

The ${}^4\text{He}$ nucleus provides a textbook case for DVCS measurements since it has only one chiral-even GPD. Therefore, by measuring coherent exclusive DVCS, one can, in a model independent way at leading twist, access the single Compton form factor and subsequently

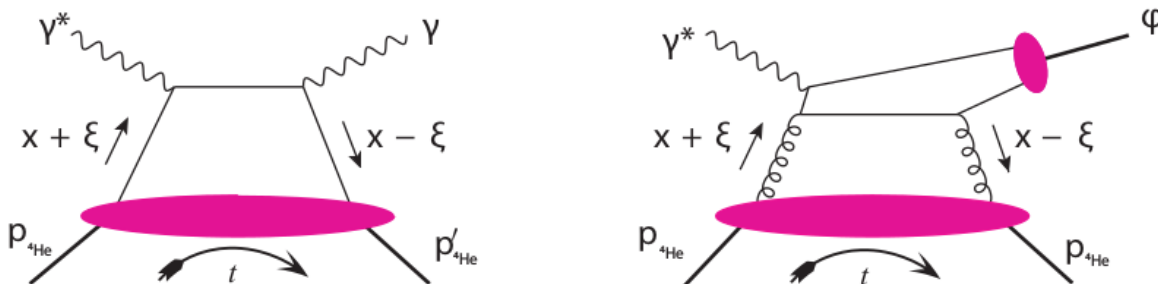


Figure 1.1: Left figure: DVCS process in the handbag approximation. Right figure: DVMP diagram at the lowest order, dominated by two-gluon exchange.

extract the transverse spatial distribution of quarks in the fast moving nucleus. It is also an ideal target to isolate higher twist effects as is proposed in the 4th proposal of the ALERT run group.

The DVCS process off nuclear targets differs from single proton scattering in that it can occur via either the coherent or incoherent channels. In this proposal, we will consider the coherent channel where the target nucleus remains intact and recoils as a whole while emitting a real photon ($eA \rightarrow e'A'\gamma$). This process allows one to measure the nuclear GPDs, which contain information on the parton correlations and the nuclear forces in the target [4, 15]. We propose to measure coherent DVCS Beam Spin Asymmetries (BSA) in order to extract in a model independent way both the real and imaginary parts of the ^4He nuclear Compton form factor H_A . This will lead the way toward the determination of the nucleus 3D picture in terms of its basic degrees of freedom, namely valence quarks in this case. In addition, the comparison between the coherent nuclear BSA and the free proton ones will allow us to study a variety of nuclear medium effects, such as the modification of quark confinement size in the nuclear medium. In fact, configuration size modifications have been advocated as responsible for the behavior of the EMC ratio in the intermediate x_B region [17, 18, 19, 20]. The generalized EMC effect *i.e.* the modification of the nuclear GPDs with respect to the free nucleon ones, normalized to their respective form factors was studied in Refs. [21, 22, 23, 24]. Measurements in the intermediate x_B range between 0.1 and 0.6, and for an appropriate t -range are crucial for both establishing the role of partonic configuration sizes in nuclei, and for discerning among the several competing explanations of the EMC effect. As shown in Ref. [21], the role of partonic transverse degrees of freedom, both in momentum and coordinate space, could be important in the generalized EMC effect, thus predicting an enhancement of signals of nuclear effects with respect to the forward case (Figure 1.2).

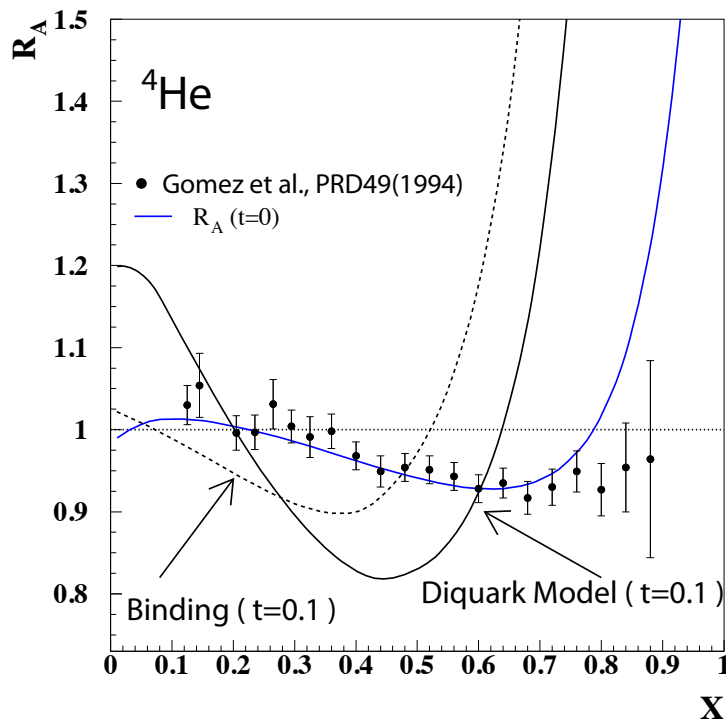


Figure 1.2: Theoretical expectations for Off-forward EMC effect in ${}^4\text{He}$. Predictions at $t = 0.1 \text{ GeV}^2$ from both “conventional” binding models and within a diquark picture for nuclear modifications are shown. For comparison, the effect at $t = 0$ is given by experimental data and theory (blue curves) on the ratio of inelastic structure functions [16] (adapted from Ref. [4]).

1.2 Deep Virtual ϕ Production Measurement

As we mentioned in the previous section, over the last two decades, there has been an increasing interest in multidimensional imaging of the structure of the nucleon. Through measurements of exclusive processes off the nucleon, information on Compton form factors and subsequently GPDs has been obtained successfully. Through these GPDs, the transverse parton density of the nucleon in the infinite momentum frame is obtained by a Fourier transform of the momentum transfer dependence leading to a transverse spatial parton density description of the nucleon.

In contrast with DVCS, which is sensitive to the charge distribution, exclusive ϕ production provides an access to the gluon GPDs. The leading order diagrams of these processes, shown in Figure 1.1, illustrate nicely this feature. In the DVCS case, the scattering is facilitated through quark exchange, while in the exclusive ϕ production, the mostly strange

ϕ , interacts with the mostly up-down nucleus via a two-gluon exchange.

A recently approved proposal using the CLAS12 detector, E12-12-007 [25], aims to extract the transverse gluon distribution of the proton and its gluonic size. In analogy, this proposal uses a very similar framework to the one discussed in E12-12-007 but focuses on the gluon GPD for a tightly bound spin zero nucleus, namely ${}^4\text{He}$, thus extending the investigation of quark GPDs in a nucleus to the case of gluons. An experiment to extract gluon distributions on heavy nuclei through coherent ϕ electroproduction at the EIC has already been proposed in the most recent EIC white paper [26]. JLab 12 GeV can start such an investigation at large x initiating a full three-dimensional partonic structure investigation of a nucleus for the first time.

Gluons are the salient partners of the quarks in a nucleon as well as in a nucleus. We know they are responsible for the confinement of quarks and for their own confinement, and represent a large fraction of the energy or the mass of the nucleon. However, gluons are charge neutral and cannot be probed directly using the electromagnetic probe. For example we know the charge distribution of ${}^4\text{He}$ and how to interpret it through the charge of nucleons. For instance, the diffraction minima in the measured charge distribution of ${}^4\text{He}$ tell us that nucleons are the appropriate degrees of freedom to consider when describing the electromagnetic properties of a nucleus. In fact we have yet to see unambiguously the elusive signature of quarks in elastic scattering off a nucleus even though we know they must be there as the building blocks of nucleons. Similarly, we do not know where the gluons are distributed in the nucleon and how they participate in the long and short-range nucleon-nucleon correlations that are responsible for the structure of the nucleus. One can ask whether in a nucleus the gluons are localized in the confined volume defined by the nucleons or spread beyond the size of the nucleons. Considering only the gluonic matter in a nucleus, a natural question arises, is a nucleus the sum of localized gluon density corresponding to that of free nucleons, or else? It would be of paramount importance to test our naive understanding of the charge neutral gluonic matter when we discuss the size of the nucleon and that of the nucleus. Among the interesting questions one might ask is whether there is evidence that the gluon transverse spatial distribution is homogeneous, or does it appear to be affected by the location of the bound nucleons? In the same spirit of the discussion of quarks which was carried in the previous section, the discussion of the gluons is at least as relevant to our understanding of nuclei from basic principles.

Measuring the gluon distributions in the nucleon is an important step and will be carried by the approved experiment E12-12-007 [25]. Understanding how these distributions are modified to provide the binding and structure in a nucleus is as fascinating of a question and an integral part of our quest of using QCD to explore nuclear matter. The future Electron Ion Collider will have the tools to address these questions using heavier mesons like J/Ψ and Υ . At JLab 12 GeV we can use the lighter vector mesons, namely the ϕ , to initiate this physics program and provide a glimpse into the salient features of nuclear matter.

Chapter 2

Formalism and Experimental Observables

The observables which are sensitive to ^4He 's quark and gluon GPDs are noticeably different, and therefore, so are the techniques for extracting the quark and gluon information. In this chapter we first discuss how the GPDs relate to the proposed measurements. In 2.2 the methods by which we extract the quark GPD H_A from the DVCS beam spin asymmetry are presented and the current experimental status is discussed. In section 2.3 we show how the gluon GPD H_g is extracted from the angular distribution of the ϕ meson decay.

2.1 Generalized Partons Distributions

GPDs are universal non-perturbative objects, entering the description of hard exclusive electroproduction processes. They are defined for each quark flavor f and gluon as matrix elements of light cone operators [27] describing the transition between the initial and final states of a hadron. The GPDs depend on two longitudinal momentum fraction variables (x, ξ) and on the momentum transfer t to the target. At twist-2 order, ξ can be calculated as $x_B/(2 - x_B)$, where $x_B (= Q^2/2M_p\nu)$ is the Bjorken variable, and -2ξ is the longitudinal fraction of the momentum transfer Δ , with $\Delta^2 = (p - p')^2 = t$. x is the average longitudinal momentum fraction of the parton involved in the process.

In the limit $\xi \rightarrow 0$, the 2-dimensional Fourier transform yields impact parameter GPDs

$$f(x, \mathbf{b}_\perp) = \int \frac{d^2 \Delta_\perp}{4\pi^2} F(x, \xi = 0, \Delta) e^{-i\mathbf{b}_\perp \cdot \Delta_\perp} \quad (2.1)$$

where $F \in H, E, \tilde{H}, \tilde{E}$. With azimuthal symmetry in the transverse plane this reduces to the Hankel transform

$$f(x, b) = \int_0^\infty J_0(b\Delta_\perp) F(x, 0, \Delta_\perp^2) \frac{d\Delta_\perp}{\pi} \quad (2.2)$$

$$= \int_0^\infty J_0(b\sqrt{t}) F(x, 0, t) \sqrt{t} \frac{dt}{2\pi} \quad (2.3)$$

where J_0 is a Bessel function of the first kind. In this limit the impact parameter GPDs can be interpreted as the probability distribution of finding a parton with longitudinal momentum fraction x at a transverse position b with respect to the nucleus' center of momentum [28].

GPDs can also be considered as the off-forward kinematic generalizations of the standard Parton Distributions Functions (PDFs) from inclusive DIS. PDFs can be recovered from GPDs in the limit of zero momentum transfer between the initial and final protons (the forward limit), with no target spin flip. Similar to DIS, higher twist terms describe quark-gluon-quark correlations which are suppressed by powers of $1/Q$, we elaborate in the 4th proposal of the run group on possible methods to study these effects.

The spin zero of the ^4He target allows for a simple parametrization of its partonic structure characterized at leading twist by one chirally-even GPD H_A . In the forward limit ($t \rightarrow 0$), this GPD reduces to the usual parton densities of ^4He measured in DIS. The polynomiality property of GPDs leads to interesting consequences: the first Mellin moment provides an explicit link with the electromagnetic form factor F_A of the nucleus

$$\sum_f e_f \int_{-1}^1 dx H_A^f(x, \xi, t) = F_A(t), \quad (2.4)$$

and the second moment yields the relationship

$$\int_{-1}^1 dx x H_A^f(x, \xi, t) = M_2^{f/A}(t) + \frac{4}{5} \xi^2 d_A^f(t) \quad (2.5)$$

which constrains the ξ -dependence of the GPDs. At $t \rightarrow 0$, the first term of the right-hand side of Eq. (2.5) is the momentum fraction of the target carried by a given quark. The second term of Eq. (2.5) is the so-called D -term which was shown to encode information about the spatial distribution of forces experienced by quarks and gluons inside hadrons [15].

2.2 Coherent DVCS

2.2.1 Accessing the Quark GPD

The handbag diagram in Figure 2.1 displays a hard part which is calculable in perturbative QCD, and a soft, non-perturbative, part which contains the fundamental partonic structure of the nucleus. However, because of the loop in the handbag diagram, the x variable is not directly accessible in the DVCS process, so we access the Compton Form Factor (CFF), noted \mathcal{H}_A , and expressed in terms of the GPD as

$$\Re(\mathcal{H}_A) = \mathcal{P} \int_0^1 dx [H_A(x, \xi, t) - H_A(-x, \xi, t)] C^+(x, \xi), \quad (2.6)$$

$$\Im(\mathcal{H}_A) = H_A(\xi, \xi, t) - H_A(-\xi, \xi, t), \quad (2.7)$$

with \mathcal{P} as the Cauchy principal value integral, and $C^+(x, \xi)$ a coefficient function ($= \frac{1}{x-\xi} + \frac{1}{x+\xi}$) [29].

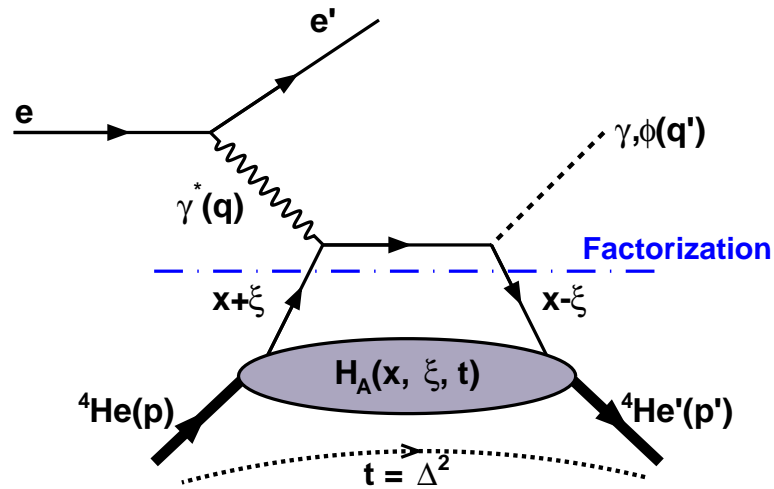


Figure 2.1: Lowest order (QCD) amplitude for the DVCS and DVMP processes, the so-called handbag diagram. q, q' represent the the four-momentum of the virtual and real photons or mesons, and p, p' are the initial and final four-momentum of the target nucleus.

Experimentally, the DVCS reaction is indistinguishable from the Bethe-Heitler (BH) process, which is the reaction where the final photon is emitted either from the incoming or the outgoing leptons. The BH process is not sensitive to GPDs and does not carry information about the partonic structure of the hadronic target. The BH cross section is calculable from

the well-known electromagnetic FFs. The DVCS amplitude is enhanced through the interference with the BH process. Figure 2.2 shows the world measurements of the ${}^4\text{He}$ $F_A(t)$ along with theoretical calculations. Following the ${}^4\text{He}$ $F_A(t)$ parametrization by R. Frosch and his collaborators [30] (valid at the small values of $-t$ which are of interest in this work), Figure 2.3 shows the calculated BH as a function of the azimuthal angle between the leptonic and the hadronic planes (ϕ), using 11 GeV electron beam on a ${}^4\text{He}$ target.

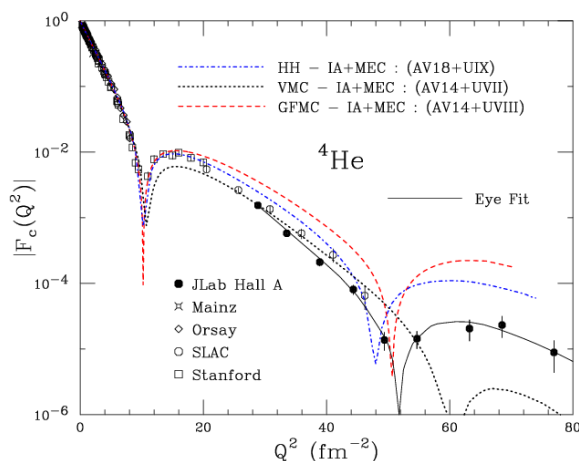


Figure 2.2: ${}^4\text{He}$ charge form factor measurements at Stanford, SLAC, Orsay, Mainz and JLab Hall A compared with theoretical calculations. The figure is from [31].

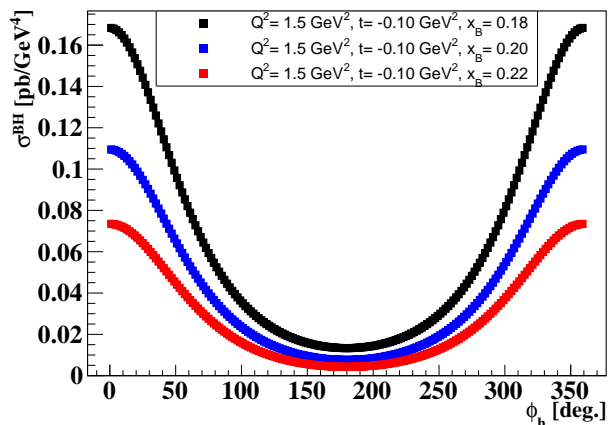


Figure 2.3: The calculated BH cross section as a function of ϕ on a ${}^4\text{He}$ target at three values of x_B and fixed values of Q^2 and t . ($t = -0.1 \text{ GeV}^2/c^2$ corresponds to $Q^2 \approx 2.57 \text{ fm}^{-2}$ on figure 2.2).

The differential cross section of lepton production of photons for a longitudinally-polarized electron beam ($\lambda = \pm 1$) and an unpolarized ${}^4\text{He}$ target can be written as:

$$\frac{d^5\sigma^\lambda}{dx_A dQ^2 dt d\phi_e d\phi} = \frac{\alpha^3}{16\pi^2} \frac{x_A y}{Q^4 \sqrt{1 + \varepsilon^2}} \frac{|\mathcal{T}_{BH}|^2 + |\mathcal{T}_{DVCS}^\lambda|^2 + \mathcal{I}_{BH^*DVCS}^\lambda}{e^6} \quad (2.8)$$

where $y = \frac{p \cdot q}{p \cdot k}$, $\varepsilon = \frac{2x_A M_A}{Q}$, $x_A = \frac{Q^2}{2p \cdot q}$, \mathcal{T}_{DVCS} is the pure DVCS scattering amplitude, \mathcal{T}_{BH} is the pure BH amplitude and $\mathcal{I}_{BH^*DVCS}^\lambda$ represents the interference amplitude. Similarly to a nucleon target one can write out the azimuthal angle, ϕ , dependence for the nuclear BH, DVCS and interference terms in the cross section: each modulation in ϕ is multiplied by a structure function containing the GPDs of interest. The different amplitudes are written as

[32],

$$|\mathcal{T}_{BH}|^2 = \frac{e^6(1+\varepsilon^2)^{-2}}{x_A^2 y^2 t \mathcal{P}_1(\phi) \mathcal{P}_2(\phi)} \left[c_0^{BH} + c_1^{BH} \cos(\phi) + c_2^{BH} \cos(2\phi) \right] \quad (2.9)$$

$$|\mathcal{T}_{DVCS}|^2 = \frac{e^6}{y^2 Q^2} \left[c_0^{DVCS} + \sum_{n=1}^2 \left(c_n^{DVCS} \cos(n\phi) + \lambda s_n^{DVCS} \sin(n\phi) \right) \right] \quad (2.10)$$

$$\mathcal{I}_{BH^*DVCS} = \frac{\pm e^6}{x_A y^3 t \mathcal{P}_1(\phi) \mathcal{P}_2(\phi)} \left[c_0^I + \sum_{n=0}^3 \left(c_n^I \cos(n\phi) + \lambda s_n^I \sin(n\phi) \right) \right], \quad (2.11)$$

The explicit expressions of the coefficients can be found in Appendix A. It is convenient to use the beam-spin asymmetry as DVCS observable because most of the experimental normalization and acceptance issues cancel out in an asymmetry ratio. The beam-spin asymmetry is measured using a longitudinally polarized lepton beam (L) on an unpolarized target (U) and defined as:

$$A_{LU} = \frac{d^5\sigma^+ - d^5\sigma^-}{d^5\sigma^+ + d^5\sigma^-}. \quad (2.12)$$

where $d^5\sigma^+(d^5\sigma^-)$ is the DVCS differential cross section for a positive (negative) beam helicity. At leading twist, the beam-spin asymmetry (A_{LU}) with the two opposite helicities of a longitudinally-polarized electron beam (L) on a spin-zero target (U) can be written as:

$$A_{LU} = \frac{x_A(1+\varepsilon^2)^2}{y} s_1^{INT} \sin(\phi) \Big/ \left[\sum_{n=0}^{n=2} c_n^{BH} \cos(n\phi) + \frac{x_A^2 t (1+\varepsilon^2)^2}{Q^2} \mathcal{P}_1(\phi) \mathcal{P}_2(\phi) c_0^{DVCS} + \frac{x_A(1+\varepsilon^2)^2}{y} \sum_{n=0}^{n=1} c_n^{INT} \cos(n\phi) \right]. \quad (2.13)$$

where $\mathcal{P}_1(\phi)$ and $\mathcal{P}_2(\phi)$ are the Bethe-Heitler propagators. The factors: $c_{0,1,2}^{BH}$, c_0^{DVCS} , $c_{0,1}^{INT}$ and s_1^{INT} are the Fourier coefficients of the BH, the DVCS and the interference amplitudes for a spin-zero target [9, 32]. The beam-spin asymmetry (A_{LU}) can be rearranged as

$$A_{LU}(\phi) = \frac{\alpha_0(\phi) \Im m(\mathcal{H}_A)}{\alpha_1(\phi) + \alpha_2(\phi) \Re e(\mathcal{H}_A) + \alpha_3(\phi) (\Re e(\mathcal{H}_A)^2 + \Im m(\mathcal{H}_A)^2)} \quad (2.14)$$

where $\Im m(\mathcal{H}_A)$ and $\Re e(\mathcal{H}_A)$ are the imaginary and real parts of the CFF \mathcal{H}_A associated to the GPD H_A . The α_i 's are ϕ -dependent kinematical factors that depend on the nuclear form factor F_A

and the independent variables Q^2 , x_B and t . These factors are simplified as:

$$\alpha_0(\phi) = \frac{x_A(1+\varepsilon^2)^2}{y} S_{++}(1) \sin(\phi) \quad (2.15)$$

$$\alpha_1(\phi) = c_0^{BH} + c_1^{BH} \cos(\phi) + c_2^{BH} \cos(2\phi) \quad (2.16)$$

$$\alpha_2(\phi) = \frac{x_A(1+\varepsilon^2)^2}{y} (C_{++}(0) + C_{++}(1) \cos(\phi)) \quad (2.17)$$

$$\alpha_3(\phi) = \frac{x_A^2 t (1+\varepsilon^2)^2}{y} \mathcal{P}_1(\phi) \mathcal{P}_2(\phi) \cdot 2 \frac{2 - 2y + y^2 + \frac{\varepsilon^2}{2} y^2}{1 + \varepsilon^2} \quad (2.18)$$

Where $S_{++}(1)$, $C_{++}(0)$, and $C_{++}(1)$ are the Fourier harmonics in the leptonic tensor. Their explicit expressions can be found in Appendix A. Using the α_i factors, one can obtain in a model-independent way $\Im m(\mathcal{H}_A)$ and $\Re e(\mathcal{H}_A)$ from fitting the experimental A_{LU} as a function of ϕ for given values of Q^2 , x_B and t .

From a practical point of view, to access the quarks' density distributions of the target, we need to extract H_A from the CFF \mathcal{H}_A , that appear directly in the cross section expressions. With the assumption that the anti-quark contribution is small in our kinematical region, $H_A(\xi, \xi, t) = \Im m(\mathcal{H}_A)$ is a good approximation. Reference [29] suggests that it is a 10% to 20% correction that can be applied to the data.

2.2.2 Experimental Status

The study of coherent nuclear DVCS is still in its infancy due to the challenging detection of the low energy recoil nucleus. The deuterium was investigated at HERMES [33] and JLab Hall A [34], and the HERMES experiment was the only one to study heavier nuclei (^4He , N, Ne, Kr, and Xe) [33]. In the latter, the DVCS process was measured by identifying the scattered lepton and the real photon in the forward spectrometer. Sizable asymmetries (Figure 2.4) have been reported in the missing mass region $-1.5 < M_X < 1.7$ GeV mass, while they generally vanish at higher masses [33]. These asymmetries are further separated into coherent and incoherent asymmetries taking advantage of the different t -dependence of the electromagnetic form factors: in the ^4He case, for example, the coherent channel was assumed to dominate below $-t = 0.05$ GeV². The selection of the different regions in t (below and above) is then used to define coherent enriched and incoherent enriched data samples. The A -dependence of the ratio of the nuclear BSA to the proton BSA, over all the measured nuclei, is reported to be 0.91 ± 0.19 . Within the precision of the measurements, no obvious A -dependence of the BSA is observed: the coherent enriched ratio is compatible with unity, which is contradicting the predictions of different models [21, 22, 35]. The incoherent

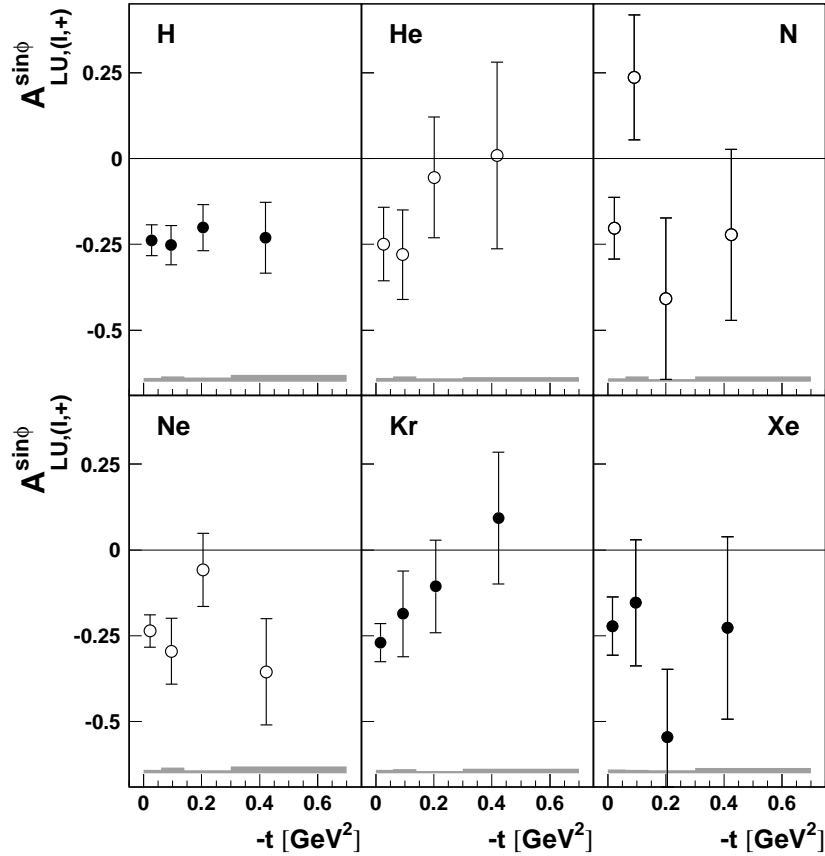


Figure 2.4: The t -dependence of the BSA on H, He, N, Ne, Kr, and Xe expressed in terms of the coefficient $A_{LU}^{\sin(\phi)}$ of the $\sin(\phi)$ contribution to A_{LU} [33]; we note that in the context of the HERMES fitting procedure $A_{LU}^{\sin(\phi)} \equiv A_{LU}$ i.e. the denominator of Eq. (2.14) was neglected.

enriched ratio, 0.93 ± 0.23 , is also compatible with unity as one would expect from an impulse approximation approach [22].

The CLAS collaboration has performed a new measurement (E08-024) of coherent exclusive DVCS on ^4He , where all the products of the reaction have been detected including the low energy recoil ^4He nucleus. This measurement was possible due to the high luminosity available at JLab, the large acceptance of CLAS spectrometer enhanced with the inner calorimeter (IC) and the addition of the newly built GEM based radial time projection chamber (RTPC). The IC was used to extend the photon detection to smaller angles and the RTPC was used to detect the recoil ^4He nucleus. The data analysis and the corresponding internal review by the CLAS collaboration are completed [14], and a first publication draft

is being finalized. The results indicate that the collaboration has been successful in measuring the exclusive DVCS both for the coherent and incoherent channels. Figure 2.5 shows the BSA A_{LU} as a function of the azimuthal angle ϕ for different bins in Q^2 (top panel), x_B (middle panel) and $-t$ (lower panel). These asymmetries are sizable indicating a strong nuclear DVCS signal.

Figure 2.6 shows the $\sin\phi$ contribution to the coherent BSA A_{LU} , which also correspond to the coefficient $\frac{\alpha_0}{\alpha_1}$ in equation 2.14 as a function of Q^2 , x_B and $-t$. It is clear the kinematic coverage and the statistics are limited, which made multidimensional binning impossible. Within the statistical uncertainties, CLAS data are in reasonable agreement with the model by Liuti et al. [4] for both the x_B and t dependencies, although a better comparison should be made with similar binning in x_B , Q^2 and t . The Liuti et al. model includes dynamical off-shellness of the nucleons taking into account medium modifications beyond the conventional Fermi motion and binding effects, which are included in their spectral function. The model also appears to be consistently giving slightly smaller asymmetries than the data, which might indicate that some of the nuclear effects are still missing in this calculation. The CLAS measurements also agree with the HERMES data, considering HERMES large uncertainties.

As shown in equation 2.14, one can extract both real and imaginary parts of the ^4He CFF \mathcal{H}_A from fitting the beam-spin asymmetry signals. This extraction is fully model-independent at leading twist and, in contrast with the proton's GPD extraction, does not necessitate any assumption on additional GPDs. Figure 2.7 presents the first ever experimental extraction of \mathcal{H}_A from exclusive measurements as a function of Q^2 , x_B , and $-t$. More theoretical effort is needed to develop predictions for \mathcal{H}_A . One can see a difference between the precision of the extracted real and imaginary parts, indicating the fact that the beam-spin asymmetry is mostly sensitive to the imaginary part of the CFF \mathcal{H}_A .

These challenging CLAS measurements were a first step toward a promising program dedicated to nuclear QCD studies. With the 12 GeV upgrade and CLAS12 augmented with the ALERT detector, exclusive nuclear DVCS and DVMP measurements in addition to tagged EMC and tagged DVCS experiments will allow our understanding of nuclear structure and nuclear effects to reach a new frontier.

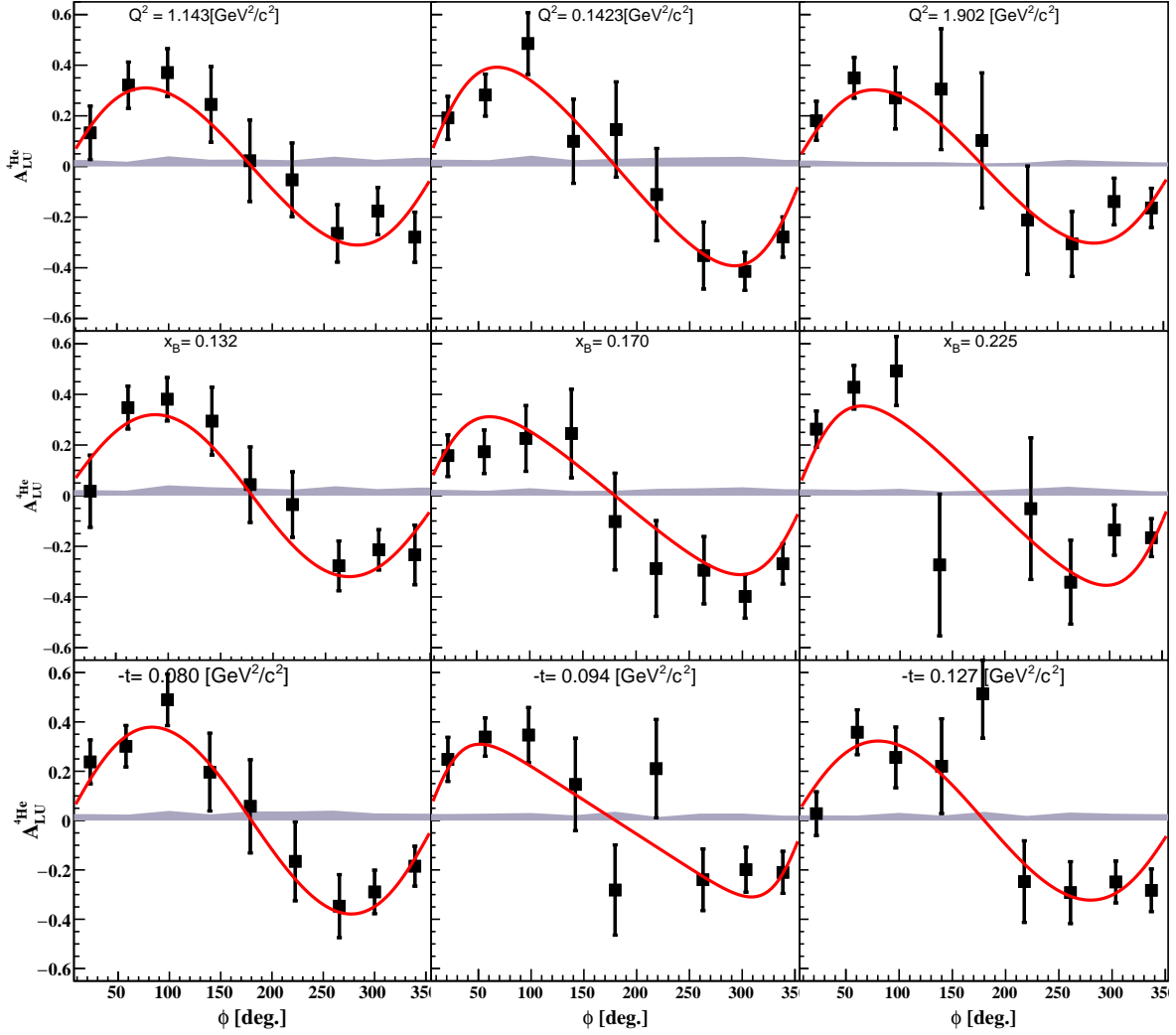


Figure 2.5: [PRELIMINARY] The measured coherent ^4He DVCS A_{LU} , from EG6 experiment, as a function of ϕ and Q^2 (top panel), x_B (middle panel), and $-t$ (bottom panel) bins [14]. The error bars represent the statistical uncertainties. The gray bands represent the systematic uncertainties. The red curves are the results of the fits with the form of equation 2.14.

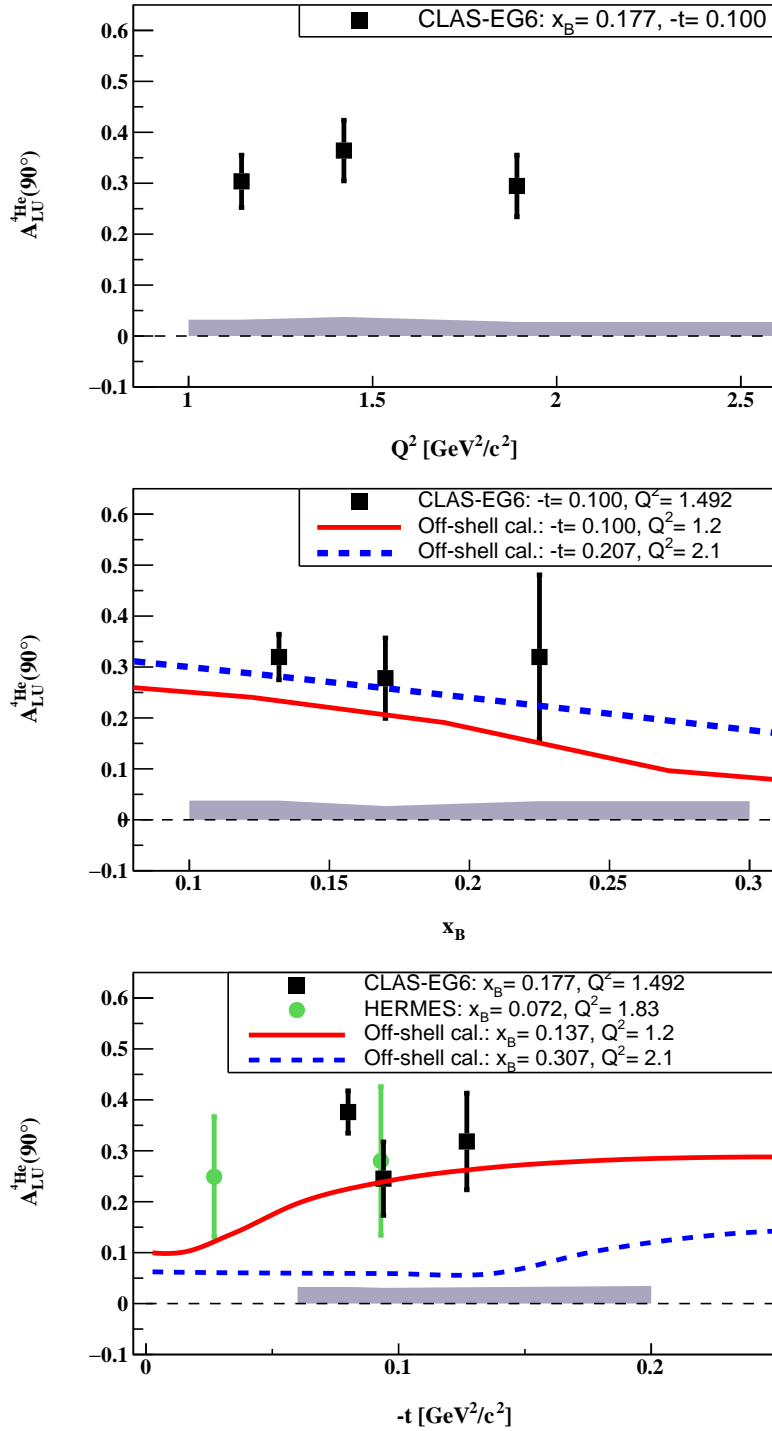


Figure 2.6: [PRELIMINARY] From EG6 experiment, the Q^2 -dependence (top panel), the x_B and the t -dependencies (bottom panel) of the fitted coherent ${}^4\text{He}$ DVCS A_{LU} asymmetry at $\phi = 90^\circ$ (black squares) [14]. The curves are theoretical predictions from [4] for two values of $-t$. The green circles are the HERMES $-A_{LU}$ (a positron beam was used) inclusive measurements[33].

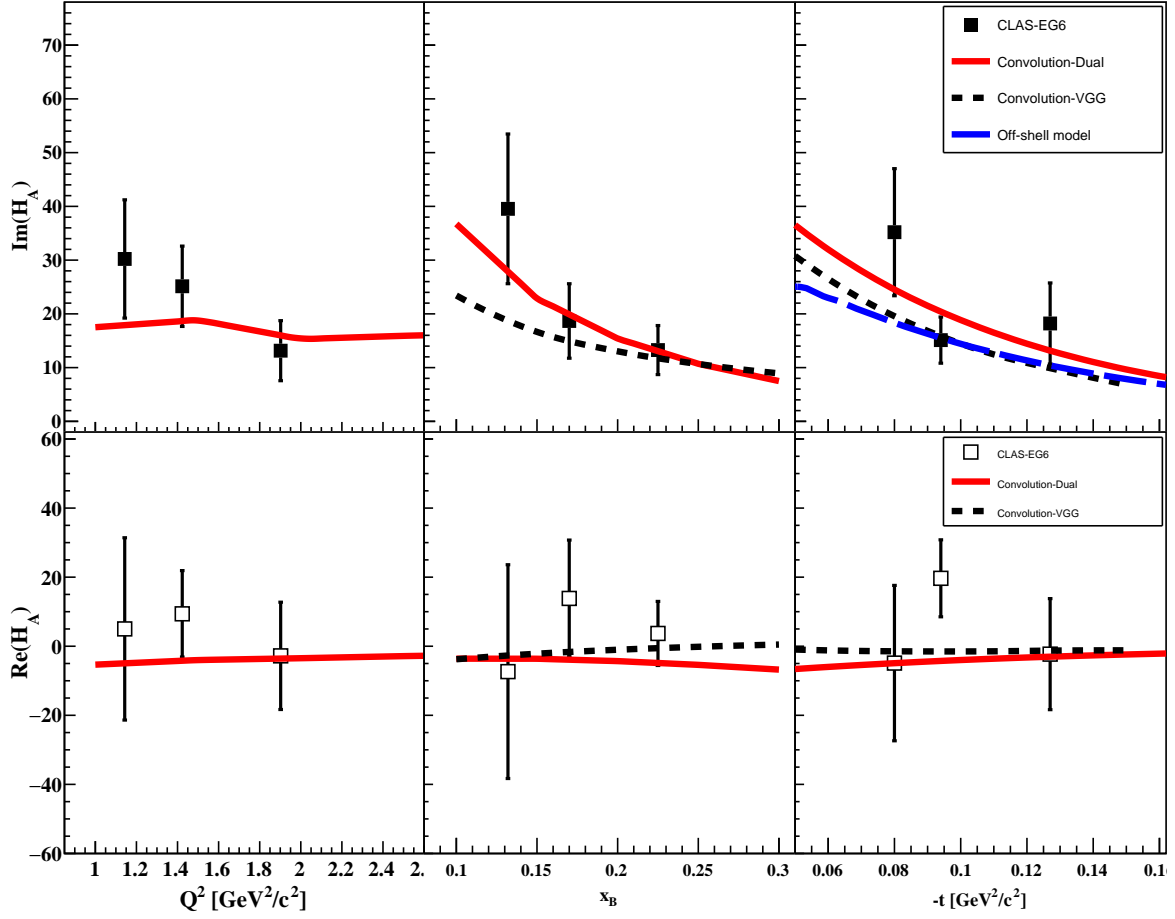


Figure 2.7: [PRELIMINARY] Model-independent extraction of the imaginary (top panel) and real (bottom panel) parts of the ^4He CFF \mathcal{H}_A , from EG6 experiment [14], as functions of Q^2 (right panel), x_B (middle panel), and t (left panel). The full red curves are calculations based on an on-shell model from [36]. The black-dashed curves are calculations from a convolution model based on the VGG model for the nucleons' GPDs [37]. The blue long-dashed curve on the top-right plot is from an off-shell model based on [38].

2.3 Coherent ϕ Production

2.3.1 Accessing the Gluon GPD

The gluon GPDs can be accessed in coherent ϕ production through a measurement of the longitudinal part of the differential cross section. The gluon GPDs for the nucleon are related to the longitudinal differential cross-section for coherent vector meson production [25, 39, 40, 41]:

$$\frac{d\sigma_L(\text{proton})}{dt} = \frac{\alpha_{em}}{Q^2} \frac{x_B^2}{1-x_B} [(1-\xi^2)|\langle H_g \rangle|^2 + \text{terms in } \langle E_g \rangle], \quad (2.19)$$

where α_{em} is a QED coupling constant, ξ is the skewness, and the nucleon GPDs H_g and E_g are relatively unconstrained. Note that the bracket notation $\langle H_g \rangle$ indicates an analog of the CFF for the DVMP, see [42] for complete expressions. However for a spin-0 nucleus, such as ${}^4\text{He}$, with only one leading-twist gluon GPD, the extraction of the gluon GPD greatly simplifies

$$\frac{d\sigma_L({}^4\text{He})}{dt} \propto |\langle H_g \rangle|^2. \quad (2.20)$$

where H_g is the only unknown on the right hand side.

The technique used to determine σ_L , which we quickly outline, is found in [43, 44]. First, the angular distribution of the kaons decay is measured. This angular distribution is used to extract the spin-density matrix element. The angular distribution in the helicity frame of the vector meson is

$$W(\cos\theta_H) = \frac{3}{4} [(1-r_{00}^{04}) + (3r_{00}^{04} - 1)\cos^2\theta_H] \quad (2.21)$$

where r_{00}^{04} is a spin-density matrix element, and θ_H is the decay angle in the rest frame of the ϕ where the z-direction is aligned with the ϕ momentum in the center of momentum system. Equation (2.21) is a result of s-channel helicity conservation and r_{00}^{04} is extract by fitting its $\cos^2\theta_H$ angular dependence. Next, the spin-density matrix element is used to determine the ratio $R = \sigma_L/\sigma_T$, which is the ratio of longitudinal to transverse cross-sections,

$$R = \frac{r_{00}^{04}}{\varepsilon(1-r_{00}^{04})}, \quad (2.22)$$

where ε is the virtual photon polarization.

With R determined from decay distribution of the vector meson, the measured differential cross-section is then used to extract the longitudinal part as

$$\frac{d\sigma_L}{dt} = \frac{1}{(\varepsilon + 1/R)\Gamma(Q^2, x_B, E)} \frac{d^3\sigma}{dQ^2 dx_B dt}, \quad (2.23)$$

where Γ is the virtual photon-flux. Now with $d\sigma_L/dt$ extracted, we can use it in equation (2.20) to study the gluon distribution in ${}^4\text{He}$.

2.3.2 Experimental Status

Like the case with coherent DVCS, the experimental status of coherent ϕ production on nuclear targets is lacking. We are proposing the first measurement of exclusive electroproduction of the ϕ on ${}^4\text{He}$. However, exclusive electroproduction on the nucleon does provide a very useful starting point. We will use the existing data on the proton, which is shown in Figures 2.8 and 2.9, to build up a reasonable model (see 4.2.2) which can be used to estimate production rates.

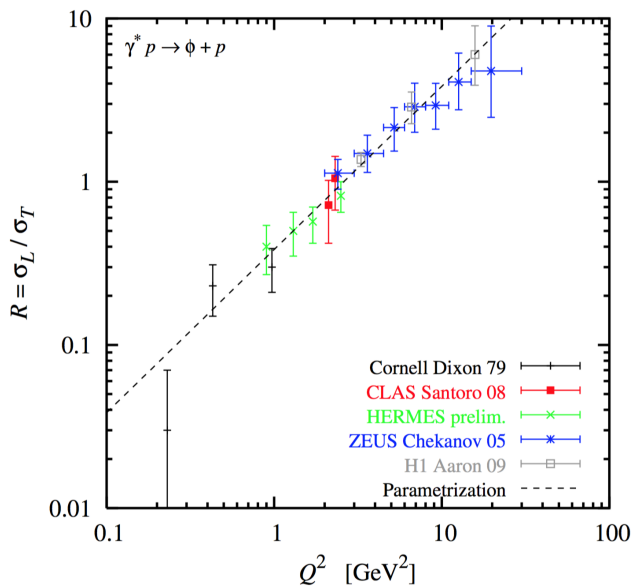


Figure 2.8: Figure come directly from PR12-12-007 [25]. The parametrization of R used to calculate ϕ production off a proton target plotted vs Q^2 against world data. For more information on the world data. See references: CLAS [45, 46], Cornell [47, 48], HERMES [49], NMC [50], ZEUS [51], and H1 [52].

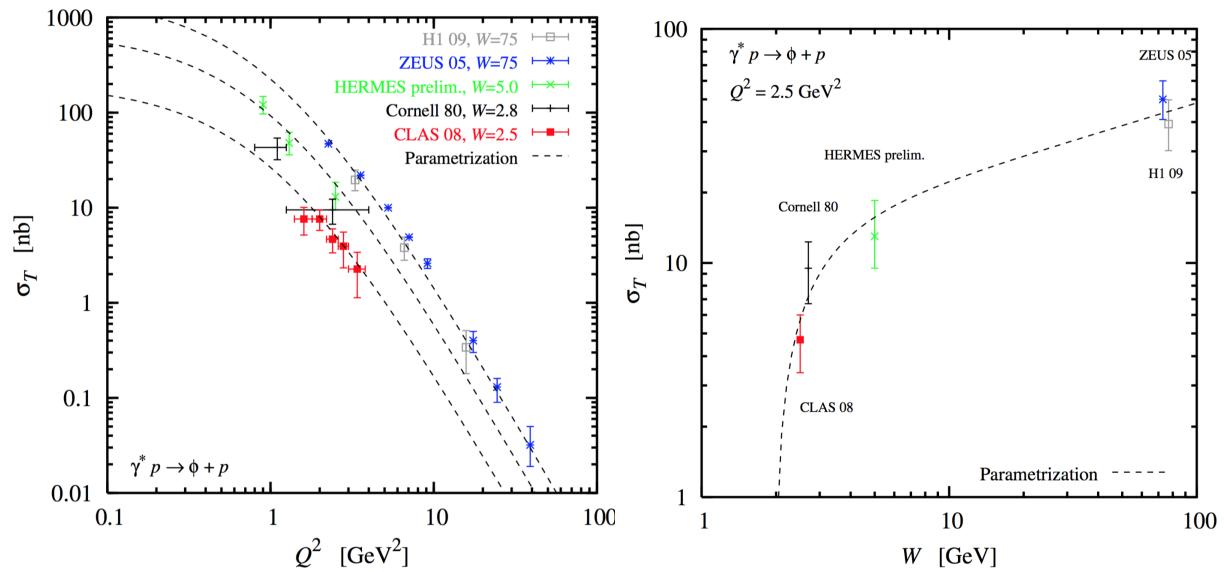


Figure 2.9: Figures come directly from PR12-12-007 [25]. The parametrization in W and Q^2 used for cross-section calculation for ϕ production off a proton target plotted against world data. For more information on the world data, see references: CLAS [45, 46], Cornell [47, 48], HERMES [49], NMC [50], ZEUS [51], and H1 [52]. Reproduced from [25]

Chapter 3

Experimental Setup

All the different measurements of the ALERT run group require, in addition to a good scattered electron measurement, the detection of low energy nuclear recoil fragments with a large kinematic coverage. Such measurements have been performed in CLAS (BONuS and eg6 runs), where the adequacy of a small additional detector placed in the center of CLAS right around the target has shown to be the best solution. We propose here a similar setup using the CLAS12 spectrometer augmented by a low energy recoil detector.

We summarize in Table 3.1 the requirements for the different experiments proposed in the run group. By comparison with previous similar experiments, the proposed tagged measurements necessitate a good particle identification. Also, CLAS12 will be able to handle higher luminosity than CLAS so it will be key to exploit this feature in the future setting in order to keep our beam time request reasonable.

Measurement	Particles detected	p range	θ range
Nuclear GPDs	^4He	$230 < p < 400 \text{ MeV}/c$	$\pi/4 < \theta < \pi/2$ rad
Tagged EMC	p, ^3H , ^3He	As low as possible	As close to π as possible
Tagged DVCS	p, ^3H , ^3He	As low as possible	As close to π as possible

Table 3.1: Requirements for the detection of low momentum spectator fragments of the proposed measurements.

This chapter will begin with a brief description of CLAS12. After presenting the existing options for recoil detection and recognize that they will not fulfill the needs laid out above,

we will describe the design of the proposed new recoil detector ALERT. We will then present the reconstruction scheme of ALERT and show the first prototypes built by our technical teams. Finally, we specify the technical contributions of the different partners.

3.1 The CLAS12 Spectrometer

The CLAS12 detector is designed to operate with 11 GeV beam at an electron-nucleon luminosity of $\mathcal{L} = 1 \times 10^{35} \text{ cm}^{-2}\text{s}^{-1}$. The baseline configuration of the CLAS12 detector consists of the forward detector and the central detector packages [53] (see Figure 3.1). We use the forward detector for electron detection in all ALERT run group proposals, while DVCS centered proposals also use it for photon detection. The central detector's silicon tracker and micromegas will be removed to leave room for the recoil detector.

The scattered electrons and photons will be detected in the forward detector which consists of the High Threshold Cherenkov Counters (HTCC), Drift Chambers (DC), the Low Threshold Cherenkov Counters (LTCC), the Time-of-Flight scintillators (TOF), the Forward Calorimeter and the Preshower Calorimeter. The charged particle identification in the forward detector is achieved by utilizing the combination of the HTCC, LTCC and TOF arrays with the tracking information from the Drift Chambers. The HTCC together with the Forward Calorimeter and the Preshower Calorimeter will provide a pion rejection factor of more than 2000 up to a momentum of 4.9 GeV/c, and a rejection factor of 100 above 4.9 GeV/c. The photons are detected using the calorimeters.

3.2 Available options for a Low Energy Recoil Detector

We explored available solutions for the low-energy recoil tracker with adequate momentum and spatial resolution, and good particle identification for recoiling light nuclei (p, ^3H and ^3He). After investigating the feasibility of the proposed measurements using the CLAS12 Central Detector and the BONuS Detector [54, 55], we concluded that we needed to build a dedicated detector. We summarize in the following the facts that led us to this conclusion.

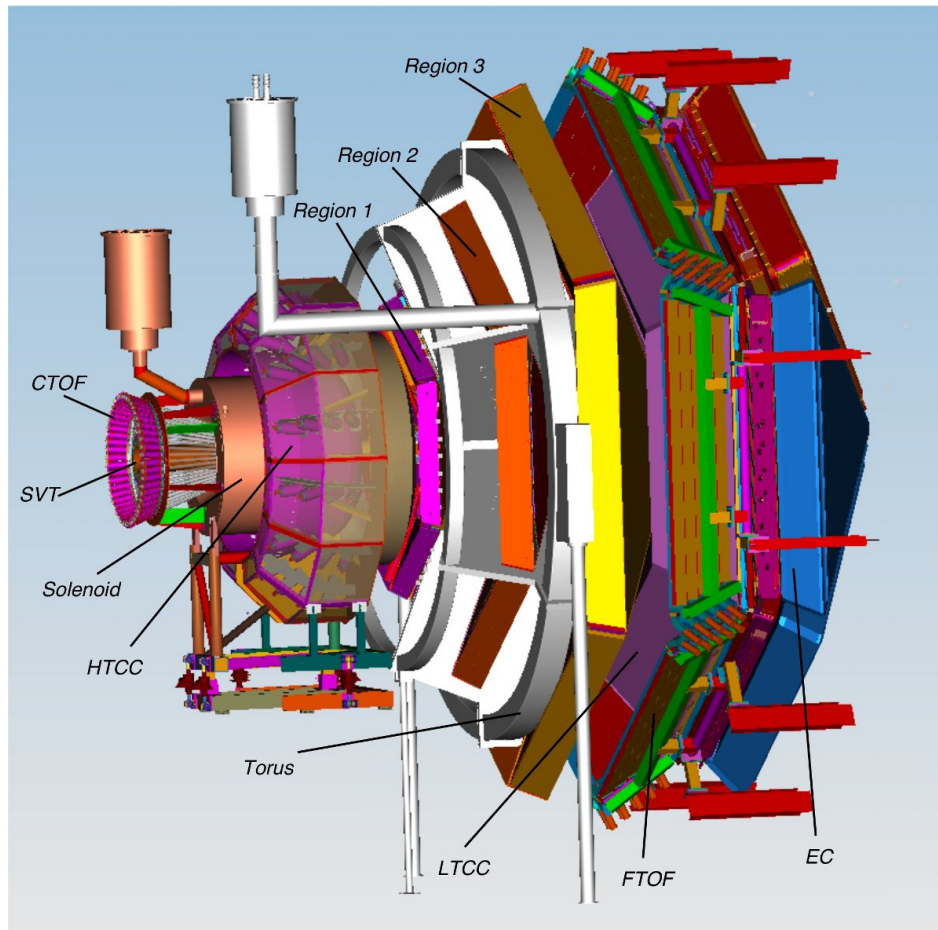


Figure 3.1: The schematic layout of the CLAS12 baseline design.

3.2.1 CLAS12 Central Detector

The CLAS12 Central Detector [53] is designed to detect various charged particles over a wide momentum and angular range. The main detector package includes:

- Solenoid Magnet: provides a central longitudinal magnetic field up to 5 Tesla, which serves to curl emitted low energy Møller electrons and determine particle momenta through tracking in the central detector.
- Central Tracker: consists of 3 double layers of silicon strips and 6 layers of Micromegas. The thickness of a single silicon layer is 320 μm .
- Central Time-of-Flight: an array of scintillator paddles with a cylindrical geometry of radius 26 cm and length 50 cm; the thickness of the detector is 2 cm with designed timing resolution of $\sigma_t = 50$ ps, used to separate pions and protons up to 1.2 GeV/ c .

The current design, however, is not optimal for low energy particles ($p < 300$ MeV/ c) due to the energy loss in the first 2 silicon strip layers. The momentum detection threshold is ~ 200 MeV/ c for protons, ~ 350 MeV/ c for deuterons and even higher for ^3H and ^3He . These values are significantly too large for any of the ALERT run group proposals.

3.2.2 BONuS12 Radial Time Projection Chamber

The original BONuS detector was built for Hall B experiment E03-012 to study neutron structure at high x_B by scattering electrons off an almost on-shell neutron inside deuteron. The purpose of the detector was to tag the low energy recoil protons ($p > 60$ MeV/ c). The key component for detecting the slow protons was the Radial Time Projection Chamber (RTPC) based on Gas Electron Multipliers (GEM). A later run period (eg6) used a newly built RTPC with a new design to detect recoiling α particles in coherent DVCS scattering. The major improvements of the eg6 RTPC were full cylindrical coverage and a higher data taking rate.

The approved 12 GeV BONuS (BONuS12) experiment is planning to use a similar device with some upgrades. The target gas cell length will be doubled, and the new RTPC will be longer as well, therefore doubling the luminosity and increasing the acceptance. Taking advantage of the larger bore (~ 700 mm) of the 5 Tesla solenoid magnet, the maximum

Detector Property	RTPC	ALERT
Detection region radius	4 cm	5 cm
Longitudinal length	~ 40 cm	~ 30 cm
Gas mixture	80% helium/20% DME	90% helium/10% isobutane
Azimuthal coverage	360°	340°
Momentum range	70-250 MeV/c protons	70-250 MeV/c protons
Transverse mom. resolution	10% for 100 MeV/c protons	10% for 100 MeV/c protons
z resolution	3 mm	3 mm
Solenoidal field	~ 5 T	~ 5 T
ID of all light nuclei	No	Yes
Luminosity	3×10^{33} nucleon/cm ² /s	6×10^{34} nucleon/cm ² /s
Trigger	can not be included	can be included

Table 3.2: Comparison between the RTPC (left column) and the new tracker (right column).

radial drift length will be increased from the present 3 cm to 4 cm, improving the momentum resolution by 50% [55] and extending the momentum coverage. The main features of the proposed BONuS12 detector are summarized in Table 3.2.

In principle, particle identification can be obtained from the RTPC through the energy loss dE/dx in the detector as a function of the particle momentum (see Figure 3.2). However, with such a small difference between ^3H and ^3He , it is nearly impossible to discriminate between them on an event by event basis because of the intrinsic width of the dE/dx distributions. This feature is not problematic when using deuterium target, but makes the RTPC no longer a viable option for our tagged EMC and tagged DVCS measurements which require a ^4He target and the differentiation of ^4He , ^3He , ^3H , deuterons and protons.

Another issue with the RTPC is its slow response time due to a long drift time ($\sim 5 \mu\text{s}$). If a fast recoil detector could be included in the trigger it would have a significant impact on the background rejection. Indeed, in about 90% of DIS events on deuteron or helium, the spectator fragments have too low energy or too small angle to get out of the target and be detected. By including the recoil detector in the trigger, we would not be recording these events anymore. Since the data acquisition speed was the main limiting factor for both BONuS and eg6 runs in CLAS, this would be a much needed reduction of the pressure on the DAQ.

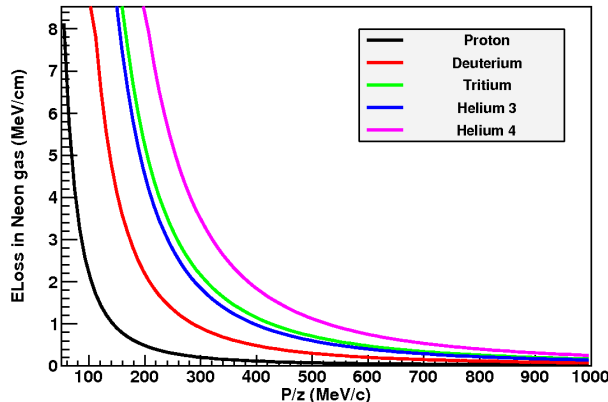


Figure 3.2: Calculation of energy loss in Neon gas as a function of the particle momentum divided by its charge for different nuclei.

3.2.3 Summary

In summary, we found that the threshold of the CLAS12 inner tracker is significantly too high to be used for our measurements. On the other hand, the recoil detector planned for BONuS12, a RTPC, is not suitable due to its inability to distinguish all kind of particles we need to measure. Moreover, as the RTPC cannot be efficiently included in the trigger, a lot of background events are sent to the readout electronics, which will cause its saturation and limit the maximum luminosity the detector can handle. Therefore, we propose a new detector design.

3.3 Design of the ALERT Detector

We propose to build a low energy recoil detector consisting of two sub-systems: a drift chamber and a scintillator hodoscope. The drift chamber will be composed of 8 layers of sense wires to provide tracking information while the scintillators will provide particle identification through time-of-flight and energy measurements. To reduce the material budget, thus reducing the threshold to detect recoil particles at as low energy as possible, the scintillator hodoscope will be placed inside the gas chamber, just outside of the last layer of drift wires.

The drift chamber volume will be filled with a light gas mixture (90% He and 10% C_4H_{10}) at atmospheric pressure. The amplification potential will be kept low enough in order to not

be sensitive to relativistic particles such as electrons and pions. Furthermore, a light gas mixture will increase the drift speed of the electrons from ionization. This will allow the chamber to withstand higher rates and experience lower hit occupancy. The fast signals from the chamber and the scintillators will be used in coincidence with electron trigger from CLAS12 to reduce the overall DAQ trigger rate and allow for operation at high luminosity.

The detector is designed to fit inside the central TOF of CLAS12; the silicon vertex tracker and the micromegas vertex tracker (MVT) will be removed. The available space has thus an outer radius of slightly more than 20 cm. A schematic layout of the preliminary design is shown in Figure 3.3 and its characteristics compared to the RTPC design in Table 3.2. The different detection elements are covering about 340° of the polar angle to leave room for mechanics, and are 30 cm long with an effort made to reduce the particle energy loss through the materials. From the inside out, it is composed of:

- a 30 cm long cylindrical target with an outer radius of 6 mm and target walls 25 μm Kapton filled with 3 atm of helium;
- a clear space filled with helium to reduce secondary scattering from the high rate Møller electrons with an outer radius of 30 mm;
- the drift chamber, its inner radius is 32 mm and its outer radius is 85 mm;
- two rings of plastic scintillators placed inside the gaseous chamber, with total thickness of roughly 20 mm.

3.3.1 The Drift Chamber

While drift chambers are very useful to cover large areas at a moderate price, huge progress has been made in terms of their ability to withstand higher rates using better electronics, shorter distance between wires and optimization of the electric field over pressure ratio. Our design is based on other chambers developed recently. For example for the dimuon arm of ALICE at CERN, drift chambers with cathode planes were built in Orsay [56]. The gap between sense wires is 2.1 mm and the distance between two cathode planes is also 2.1 mm, the wires are stretched over about 1 m. Belle II is building a cylindrical drift chamber very similar to what is needed for this experiment and for which the space between wires is around 2.5 mm [57]. Finally, a drift chamber with wire gaps of 1 mm is being built for the small wheel of ATLAS at CERN [58]. The cylindrical drift chamber proposed for our experiment

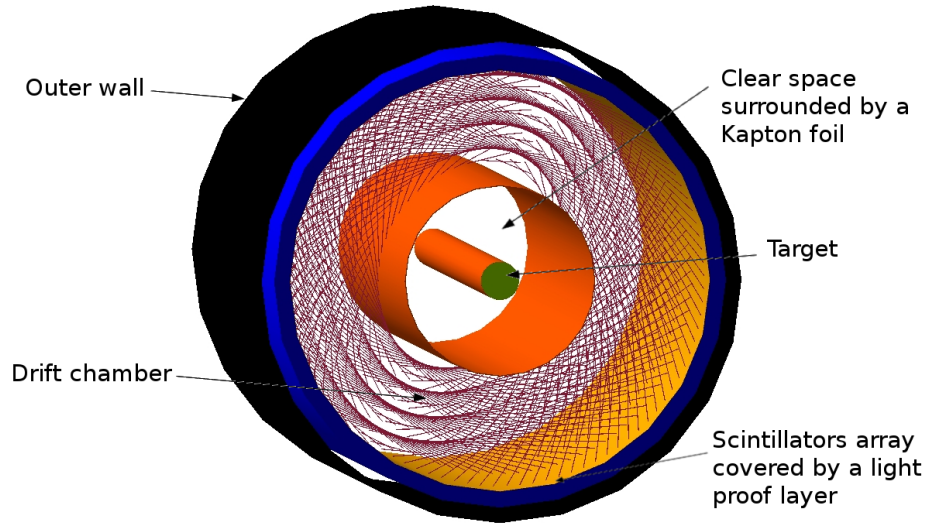


Figure 3.3: The schematic layout of the ALERT detector design, viewed from the beam direction.

is 300 mm long, and we therefore considered that a 2 mm gap between wires is technically a rather conservative goal. Optimization is envisioned based on experience with prototypes.

The radial form of the detector does not allow for 90 degrees x-y wires in the chamber. Thus, the wires of each layer are at alternating angle of $\pm 10^\circ$, called the stereo-angle, from the axis of the drift chamber. We use stereo-angles between wires to determine the coordinate along the beam axis (z). This setting makes it possible to use a thin forward end-plate to reduce multiple scattering of the outgoing high-energy electrons. A rough estimate of the tension due to the ~ 2600 wires is under 600 kg, which appears to be reasonable for a composite end-plate.

The drift chamber cells are composed of one sense wire made of gold plated tungsten surrounded by field wires, however the presence of the 5 T magnetic field complicates the field lines. Several cell configurations have been studied with MAGBOLTZ [59], we decided to choose a conservative configuration as shown in Figure 3.4. The sense wire is surrounded by 6 field wires placed equidistantly from it in a hexagonal pattern. The distance between the sense and field wires is constant and equal to 2 mm. Two adjacent cells share the field wires placed between them. The current design will have 8 layers of cells of similar radius. The simulation code MAGBOLTZ is calculating the drift speed and drift paths of the electrons (Figure 3.4). With a moderate electric field, the drift speed is around 10 microns/ns, the

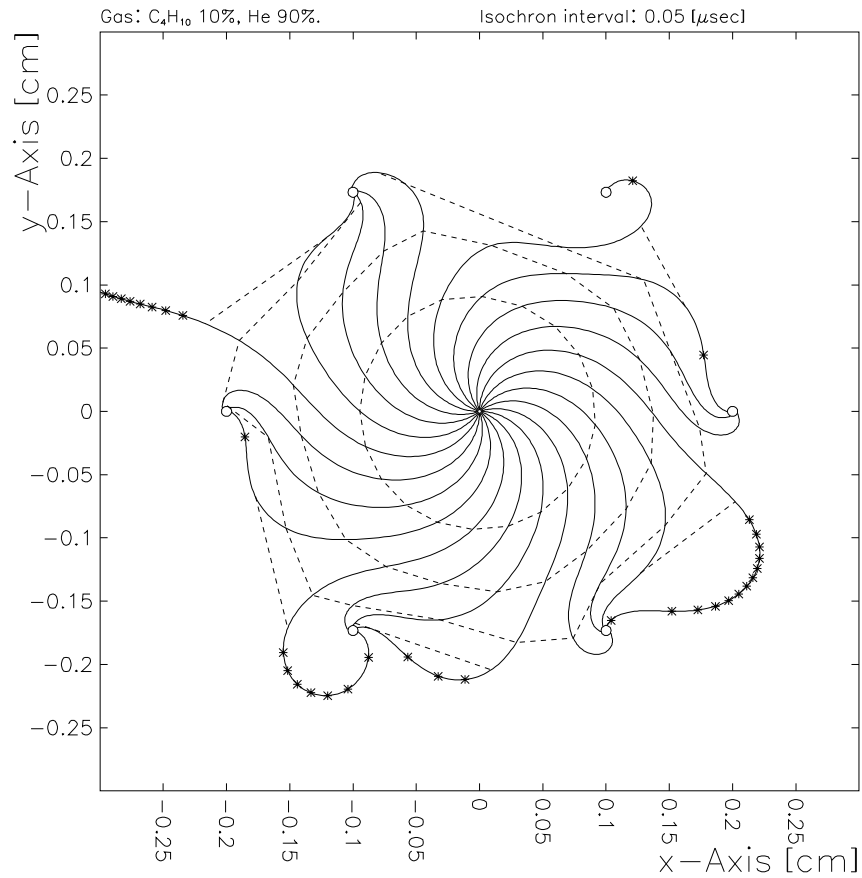


Figure 3.4: Drift lines simulated using MAGBOLTZ [59] for one sense wire (at the center) surrounded by 6 field wires. The two electric field lines leaving the cell disappear when adjusting the voltages on the wires. Dashed lines are isochrones spaced by 50 ns. This shows that the maximum drift time is about 250 ns.

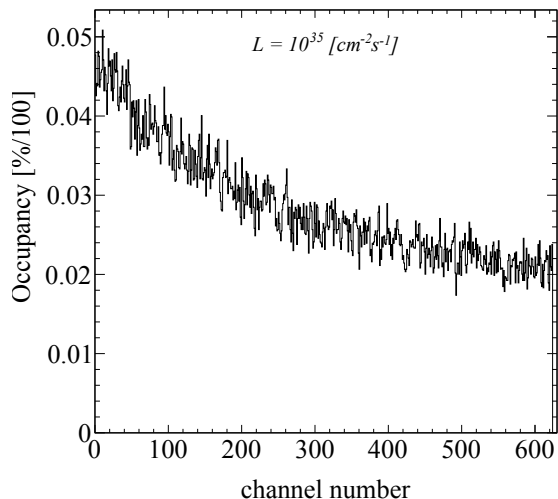


Figure 3.5: A full Geant4 simulation of the ALERT drift chamber hit occupancy at a luminosity of $10^{35} \text{ cm}^{-2}\text{s}^{-1}$. The channel numbering starts with the inner most wires and works outwards.

average drift time expected is thus 250 ns (over 2 mm). Assuming a conservative 10 ns time resolution, the spatial resolution is expected to be around 200 microns due to field distortions and spread of the signal.

The maximum occupancy, shown in Figure 3.5, is expected to be around 5% for the inner most wires at $10^{35} \text{ cm}^{-2}\text{s}^{-1}$ (including the target windows). This is the maximum available luminosity for the baseline CLAS12 and is obtained based on the physics channels depicted in Figure 3.6, assuming an integration time of 200 ns and considering a readout wire separation of 4 mm. This amount of accidental hits does not appear to be reasonable for a good tracking quality, we therefore decided to run only at half this luminosity for our main production runs. This will keep occupancy below 3%, which is a reasonable amount for a drift chamber to maintain high tracking efficiency. When running the coherent processes with the ^4He target, it is not necessary to detect the protons¹, so the rate of accidental hits can then be highly reduced by increasing the detection threshold, thus making the chamber blind to the protons². In this configuration, considering that our main contribution to occupancy are quasi-elastic protons, we are confident that the ALERT can work properly at $10^{35} \text{ cm}^{-2}\text{s}^{-1}$.

We are currently planning to use the electronics used by the MVT of CLAS12, known as

¹This running condition is specific to the proposal “Partonic Structure of Light Nuclei” in the ALERT run group.

²The CLAS *eg6* run period was using the RTPC in the same fashion.

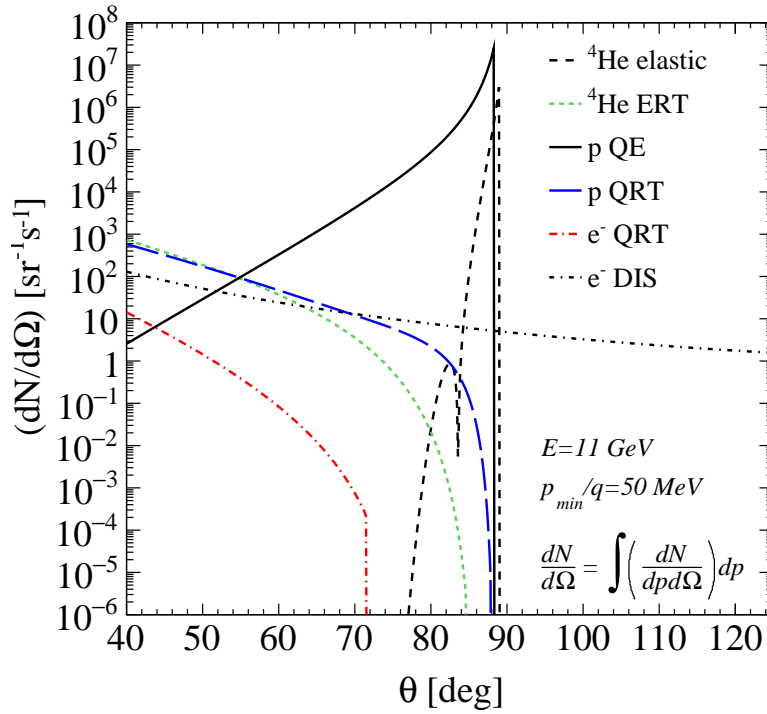


Figure 3.6: The rates for different processes as function of angle. The quasi-elastic radiative tails (QRT), ${}^4\text{He}$ elastic radiative tail (ERT), and DIS contributions have been integrated over momenta starting at $p/q = 50 \text{ MeV}/c$, where q is the electric charge of the particle detected.

the DREAM chip [60]. Its dynamic range and time resolution correspond to the needs of our drift chamber. To ensure that it is the case, tests with a prototype will be performed at the IPN Orsay (see section 3.5).

3.3.2 The Scintillator Array

The scintillator array will serve two main purposes. First, it will provide a useful complementary trigger signal because of its very fast response time, which will reduce the random background triggers. Second, it will provide particle identification, primarily through a time-of-flight measurement, but also by a measurement of the particle total energy deposited and path length in the scintillator which is important for doubly charged ions.

The length of the scintillators cannot exceed roughly 40 cm to keep the time resolution below 150 ps. It must also be segmented to match with tracks reconstructed in the drift chamber. Since ${}^3\text{He}$ and ${}^4\text{He}$ will travel at most a few mm in the scintillator for the highest anticipated momenta (~ 400 MeV/c), a multi-layer scintillator design provides an extra handle on particle identification by checking if the range exceeded the thickness of the first scintillator layer.

The initial scintillator design consists of a thin (2 mm) inner layer of 60 bars, 30 cm in length, and 600 segmented outer scintillators (10 segments 3 cm long for each inner bar) wrapped around the drift chamber. Each of these thin inner bars has SiPM³ detectors attached to both ends. A thicker outer layer (18 mm) will be further segmented along the beam axis to provide position information and maintain good time resolution.

For the outer layer, a dual ended bar design and a tile design with embedded wavelength shifting fiber readouts similar to the forward tagger's hodoscope for CLAS12 [61] were considered. After simulating these designs, it was found that the time resolution was insufficient except only for the smallest of tile designs ($15 \times 15 \times 7$ mm³). Instead of using fibers, a SiPM will be mounted directly on the outer layer of a keystone shaped scintillator that is 30 mm in length and 18 mm thick. This design can be seen in Figure 3.7 which shows a full Geant4 simulation of the drift chamber and scintillators. By directly mounting the SiPMs to the scintillator we collect the maximum signal in the shortest amount of time. With the large number of photons we expect, the time resolution of SiPMs will be a few tens of ps, which is well within our target.

³SiPM: silicon photomultiplier.

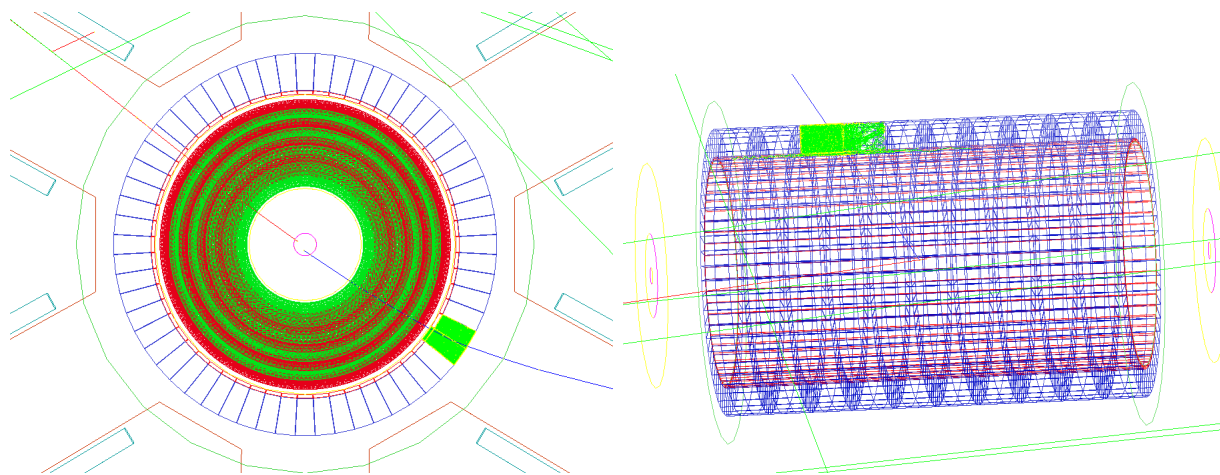


Figure 3.7: Geant4 simulation of a proton passing through the recoil drift chamber and scintillator hodoscope. The view looking downstream (left) shows the drift chamber’s eight alternating layers of wires (green and red) surrounded by the two layers of scintillator (red and blue). Simulating a proton through the detector, photons (green) are produced in a few scintillators. On the right figure, the dark blue rings are graphical feature showing the contact between the adjacent outer scintillators.

The advantage of a dual ended readout is that the time sum is proportional to the TOF plus a constant. The improved separation of different particles can be seen in Figure 3.8. Reconstructing the position of a hit along the length of a bar in the first layer is important for the doubly charged ions because they will not penetrate deep enough to reach the second layer of segmented scintillator.

The front-end electronics for the SiPMs will include preamplifiers and ASICs⁴ which provide both TDC and ADC readouts. The PETIROC-2A[62] ASIC provides excellent time resolution (18 ps on trigger output with 4 photoelectrons detected) and a maximum readout rate at about 40k events/s. Higher readout rates can be handled by using external digitizers by using the analog mode of operation and increase this rate by an order of magnitude. The ASIC also has the advantage of being able to tune the individual over-bias voltages with an 8-bit DAC.

The expected radiation damage to the SiPMs and scintillator material is found to be minimal over the length of the proposed experiment. We used the CLAS12 forward tagger hodoscope technical design report [61] as a very conservative baseline for this comparison. We arrived at an estimated dose of 1 krad after about 4.5 months of running. The damage

⁴ASIC: application-specific integrated circuit.

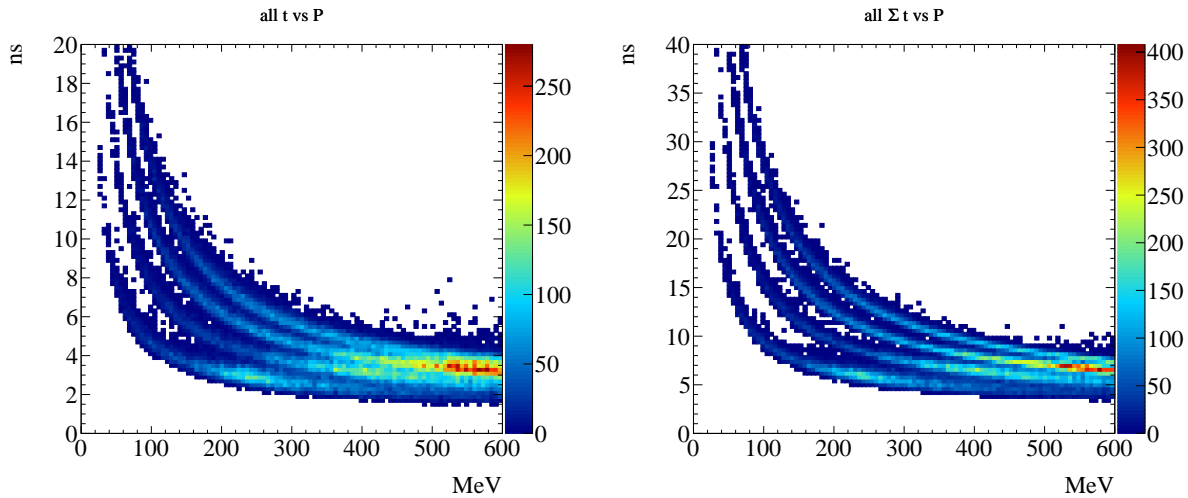


Figure 3.8: Simulated TOF for the various recoil particles vs Momentum. The TOF from just a single readout is shown on the left and the sum of the dual ended readout is shown on the right.

to the scintillator at 100 times these radiation levels would not be problematic, even for the longest lengths of scintillator used [63]. Accumulated dose on the SiPMs leads to an increased dark current. Similarly than for scintillators, we do not expect it to be significant over the length of the experiment. The interested reader is referred to the work on SiPMs for the Hall-D detectors [64, 65]. A front-end electronics prototype will be tested for radiation hardness but we expect any damage to negligible [66].

3.3.3 Target Cell

The design of the proposed ALERT target will be very similar to the eg6 target shown in Figure 3.9. The target parameters are shown in Table 3.3 with the parameters of other existing and PAC approved targets. Note that, the proposed target has an increased radius of 6 mm compared to all the others which have 3 mm radius. This increase compared to the previous CLAS targets has been made in order to compensate for the expected increase of beam size at 11 GeV. The BONuS12 target is still presently proposed to be 3 mm in radius, if such a target is operated successfully in JLab, we will definitely consider using a smaller radius as well, but we prefer to propose here a safer option that we know will work fine.

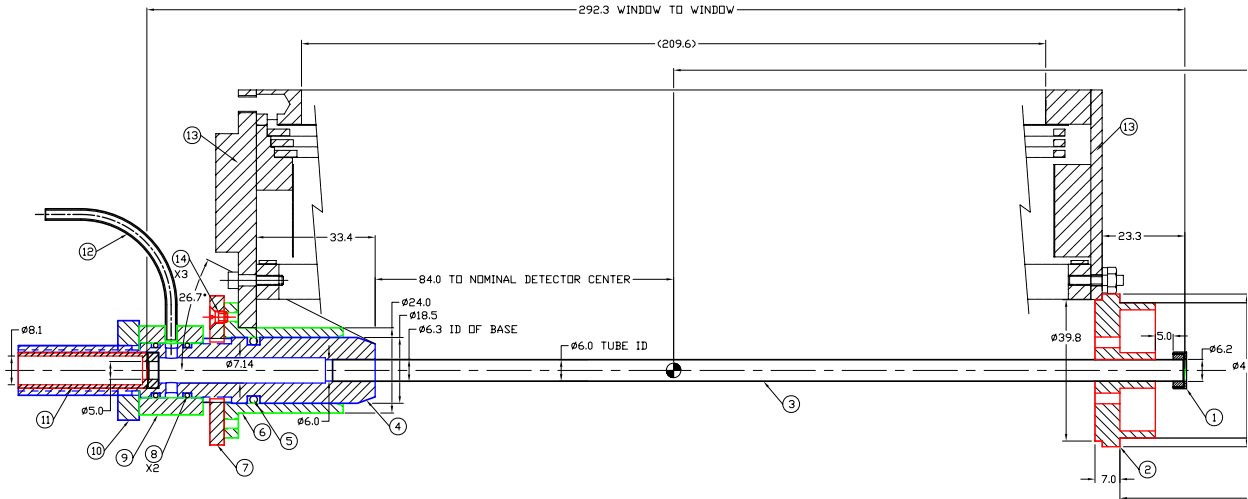


Figure 3.9: The eg6 target design drawing.

Table 3.3: Comparison of various straw targets used at JLab. The "JLab test targets" correspond to recent tests performed in JLab for the BONuS12 target, they have been tested for pressure but have never been tested with beam.

Experiment	Length	Kapton wall thickness	Pressure
CLAS target (eg6)	30 cm	27 μm	6.0 atm
BONuS12 (E12-06-113) target	42 cm	30 μm	7.5 atm
JLab test target 1	42 cm	30 μm	3.0 atm
JLab test target 2	42 cm	50 μm	4.5 atm
JLab test target 3	42 cm	60 μm	6.0 atm
ALERT proposed target	35 cm	25 μm	3.0 atm

3.4 Simulation of ALERT and reconstruction

The general detection and reconstruction scheme for ALERT is as follows. We fit the track with the drift chamber and scintillator position information to obtain the momentum over the charge. Next, using the scintillator time-of-flight, the particles are separated and identified by their mass-to-charge ratio, therefore leaving a degeneracy for the deuteron and α particles. The degeneracy between deuteron and α particles can be resolved in a few ways. The first and most simple way is to observe that an α will almost never make it to the second layer of scintillators and therefore the absence (presence) of a signal would indicate the particle is an α (deuteron). Furthermore, as will be discussed below, the measured dE/dx will differ for ${}^4\text{He}$ and ${}^2\text{H}$, therefore, taking into account energy loss in track fitting alone can provide separation. Additionally taking further advantage of the measured total energy deposited in the scintillators can help separate the α s and deuterons.

3.4.1 Simulation of ALERT

The simulation of the recoil detector has been implemented with the full geometry and material specifications in GEANT4. It includes a 5 Tesla homogeneous solenoid field and the entire detector filled with materials as described in the previous section. In this study all recoil species are generated with the same distributions: flat in momentum from threshold up to 40 MeV (~ 250 MeV/c) for protons and about 25 MeV for other particles; isotropic angular coverage; flat distribution in z -vertex; and a radial vertex coordinate smeared around the beam line center by a Gaussian distribution of sigma equal to the expected beam radius (0.2 mm). For reconstruction, we require that the particle reaches the scintillator and obtain the acceptance averaged over the z -vertex position shown in Figure 3.10.

3.4.2 Track Fitting

The tracks are obtained using a helix fitter giving the coordinates of the vertex and the momentum of the particle. The energy deposited in the scintillators could also be used to help determine the kinetic energy of the nucleus, but is not implemented in the studies we performed here. The tracking capabilities of the recoil detector are investigated assuming a spatial resolutions of 200 μm for the drift chamber. The wires are strung in the z -direction with a stereo angle of 10° . The resulting difference between generated and reconstructed

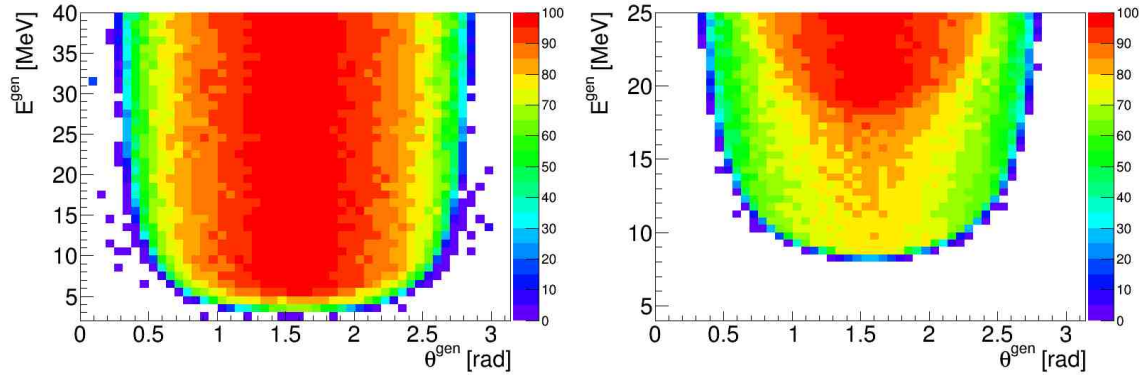


Figure 3.10: Simulated recoil detector acceptance percentage, for protons (left) and ${}^4\text{He}$ (right), when requiring energy deposition in the scintillators arrays.

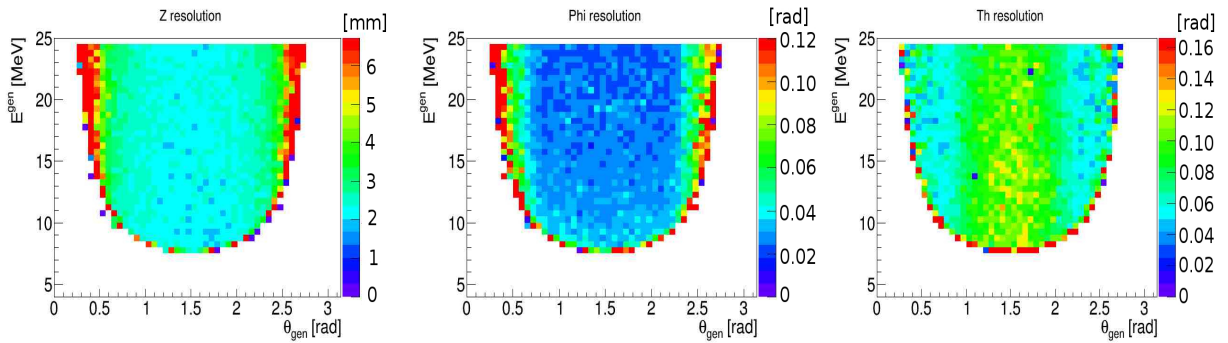


Figure 3.11: Resolutions for simulated ${}^4\text{He}$: z -vertex resolution in mm (left), azimuthal (center) and polar (right) angle resolutions in radians for the lowest energy regime when the recoil track reaches the scintillator.

variables from simulation is shown in Figure 3.11 for ${}^4\text{He}$ particles. The momentum resolution for both protons and ${}^4\text{He}$ is presented in Figure 3.12.

3.4.3 Particle identification in ALERT

The particle identification scheme is investigated using the GEANT4 simulation as well. The scintillators have been designed to ensure a 150 ps time resolution. To determine the dE/dx resolution, measurements will be necessary for the scintillators and for the drift chamber as this depends on the detector layout, gas mixture, electronics, voltages... Nevertheless,

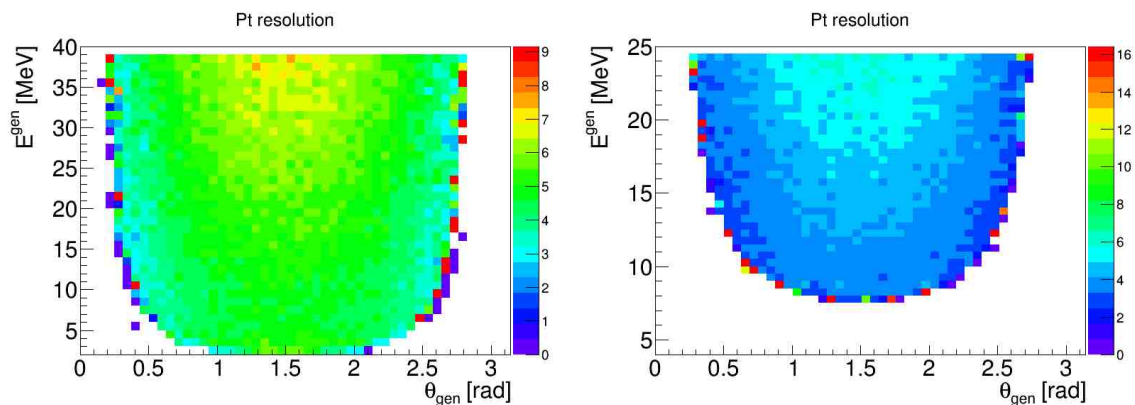


Figure 3.12: Simulated momentum resolutions (in %) as a function of energy and polar angle for protons (left) and ${}^4\text{He}$ (right) integrated over all z , when the recoil track reaches the scintillators array.

from [67], one can assume that with 8 hits in the drift chamber and the measurements in the scintillators, the energy resolution should be at least 10%. Under these conditions, a clean separation of three of the five nuclei is shown in Figure 3.13 solely based on the time of flight measured by the scintillator compared to the reconstructed momentum from the drift chamber. We then separate ${}^2\text{H}$ and α using dE/dx in the drift chamber and in the scintillators.

To quantify the separation power of our device, we simulated an equal quantity of each species. We obtained a particle identification efficiency of 99% for protons, 95% for ${}^3\text{He}$ and 98% for ${}^3\text{H}$ and around 90% for ${}^2\text{H}$ and α with equally excellent rejection factors. It is important to note that for this analysis, only the energy deposited in the scintillators was used, not the energy deposited in the drift chamber nor the path length in the scintillators, thus these numbers are very likely to be improved when using the full information⁵. This analysis indicates that the proposed reconstruction and particle identification schemes for this design are quite promising. Studies, using both simulation software and prototyping, are ongoing to determine the optimal detector parameters to minimize the detection threshold while maximizing particle identification efficiency. The resolutions presented above have been implemented in a fast Monte-Carlo used to evaluate their impact on our measurements.

⁵The uncertainty remains important about the resolutions that will be achieved for these extra information. So we deemed more reasonable to ignore them for now.

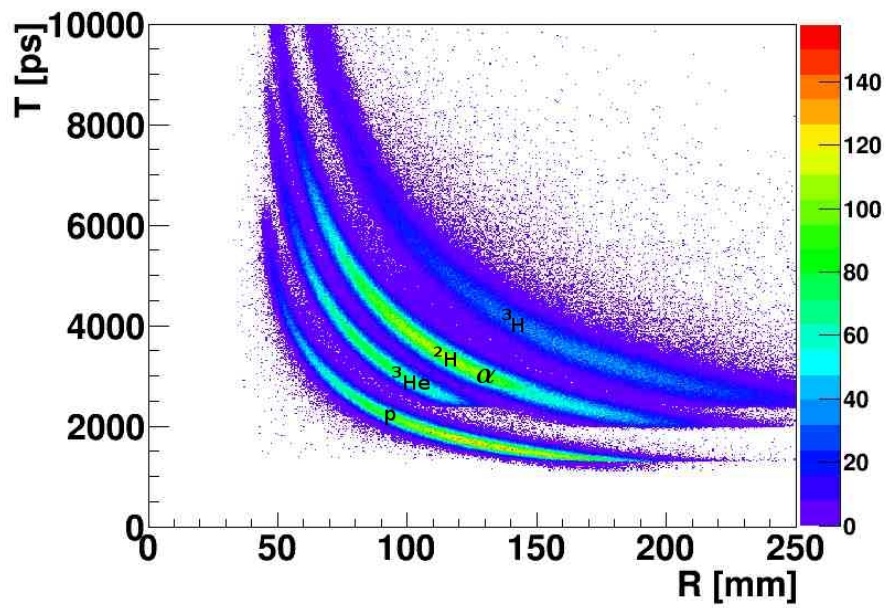


Figure 3.13: Simulated time of flight at the scintillator versus the reconstructed radius in the drift chamber. The bottom band corresponds to the proton, next band is the ^3He nuclei, ^2H and α are overlapping in the third band, the uppermost band is ^3H . ^2H and α are separated using dE/dx .

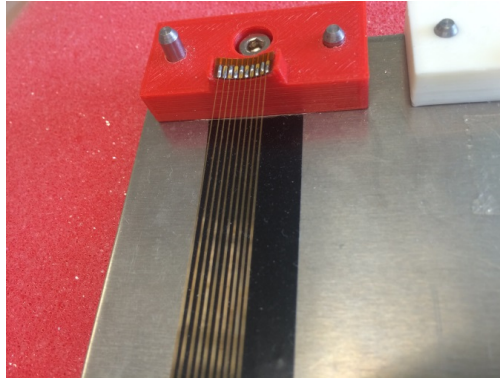


Figure 3.14: Welded wires on a curved structure with a 2 mm gap between each wire.

3.5 Drift chamber prototype

Since the design of the drift chamber presents several challenges in term of mechanical assembly, we decided to start prototyping early. The goal is to find a design that will be easy to install and to maintain if need be, while keeping the amount of material at a minimum. This section presents the work done in Orsay to address the main questions concerning the mechanics that needed to be answered:

- How to build a stereo drift chamber with a 2 mm gap between wires?
- Can we have frames that can be quickly changed in case of a broken wire?
- How to minimize the forward structure to reduce the multiple scattering, while keeping it rigid enough to support the tension due to the wires?

For the first question, small plastic structures realized with a 3D printer were tested and wires welded on it, as shown in Figure 3.14. This demonstrated our ability to weld wires with a 2 mm gap on a curved structure.

To limit issues related to broken wires, we opted for a modular detector made of identical sectors. Each sector covers 20° of the azimuthal angle (Figure 3.15) and can be rotated around the beam axis to be separated from the other sectors. This rotation is possible due to the absence of one sector, leaving a 20° dead angle. Then, if a wire breaks, its sector can be removed independently and replaced by a spare. Plastic and metallic prototype sectors were made with 3D printers to test the assembling procedure and we have started the construction

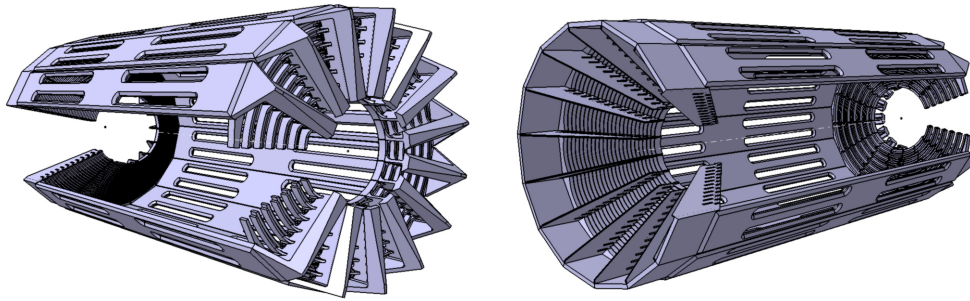


Figure 3.15: Upstream (left) and downstream (right) ends of the prototype detector in computer assisted design (CAD) with all the sectors included.

of a full size prototype of one sector. The shape of each sector is constrained by the position of the wires. It has a triangular shape on one side and due to the stereo angle, the other side looks like a pine tree with branches alternatively going left and right from a central trunk (Figure 3.16).

Finally, the material used to build the structure will be studied in details with future prototypes. Nevertheless, most recent plans are to use high rigidity plastic in the forward region and metal for the backward structure (as in Figure 3.17). The prototypes are not only designed to check the mechanical requirements summarized above but also to verify the different cell configurations, and to test the DREAM electronics (time resolution, active range, noise).

3.6 Technical contributions from the research groups

The effort to design, build and integrate the ALERT detector is led by four research groups, Argonne National Lab (ANL), Institut de Physique Nucléaire d’Orsay (IPNO), Jefferson Lab and Temple University (TU).

Jefferson Lab is the host institution. ANL, IPNO and TU have all contributed technically to CLAS12. ANL was involved in the construction of the high-threshold Cherenkov counters (HTCC) for CLAS12. ANL has a memorandum of understanding (MOU) with JLab on taking responsibility for the HTCC light collection system including testing the photomultipliers and the magnetic shielding. For the RICH detector for CLAS12, ANL developed full GEANT-4 simulations in addition to the tracking software. ANL also developed the

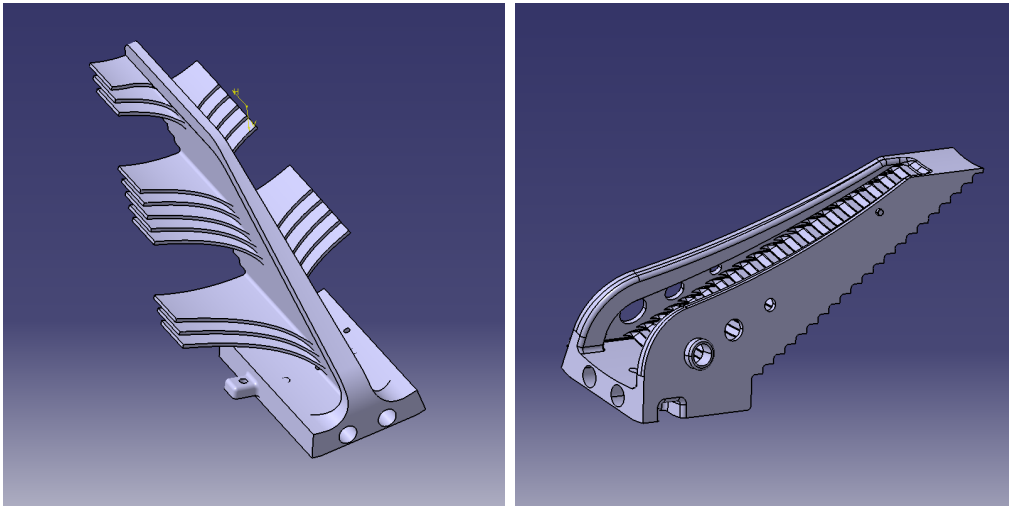


Figure 3.16: Close up on the CAD of the upstream piece (left) and downstream piece(right) of the drift chamber. Note that the design of the pieces has been optimized in comparison of what is shown in Figure 3.15.

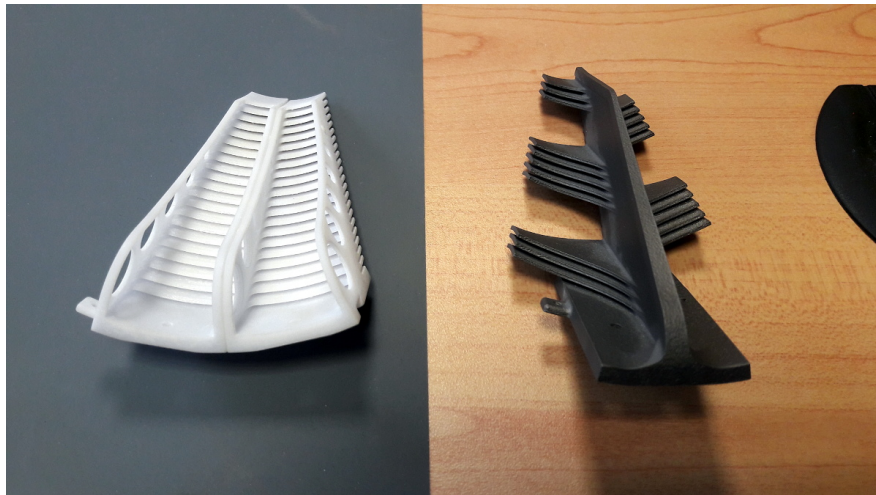


Figure 3.17: Prototypes for the mechanical parts of the drift chamber made out of plastic for the forward part and titanium for the backward.

mechanical design of the detector support elements and entrance and exit windows in addition to the front-end electronics cooling system. IPNO took full responsibility for the design and construction of CLAS12 neutron detector (CND). The CND was successfully delivered to Jefferson Lab. TU played an important role in the refurbishment of the low threshold Cherenkov counters (LTCC), which was completed recently. All 216 photomultipliers have been coated with wavelength shifting material (p-Terphenyl) at Temple University, which resulted in a significant increase in the number of photoelectrons response.

The three institutions have already shown strong technical commitment to JLab 12 GeV upgrade, with a focus on CLAS12 and this proposal is a continuation of this commitment.

3.6.1 Argonne National Laboratory and Temple University

The ANL medium energy group is responsible for the ALERT scintillator system, including scintillation material, light collection device and electronics. First results of simulations have led to the design proposed here. This work will continue to integrate the scintillator system with the wire chamber. ANL will collaborate closely with Temple University to test the light detection system. Both institutions will be responsible to assemble and test the detector.

Argonne will provide the electronics and technical support required to integrate the scintillator detector system into the CLAS12 DAQ. The effort will minimize the effort required on the part of the Hall B staff.

3.6.2 Institut de Physique Nucléaire d'Orsay

The Institut de Physique Nucléaire d'Orsay is responsible for the wire chamber and the mechanical structure of the detector design and construction. As shown in the proposal, this work has already started, a first prototype is being built to test different cell forms, wire material, wire thickness, pressure, etc. This experience will lead to a complete design of the ALERT detector integrating the scintillator built at ANL, the gas distribution system and the electronic connections.

In partnership with *CEA Saclay*, IPN Orsay will also test the use of the DREAM front-end chip for the wire chamber. Preliminary tests were successful and will continue. The

integration of the chip with CLAS12 is expected to be done by the *CEA Saclay*, since they use the same chip to readout the CLAS12 MVT. Adaptations to the DAQ necessary when the MVT will be replaced by ALERT will be performed by the staff of IPN Orsay.

3.6.3 Jefferson Laboratory

We expect Jefferson Lab to help with the configuration of the beam line. This will include the following items.

Beam Dump Upgrade The maximum beam current will be around 1000 nA for the production runs at $10^{35} \text{ cm}^{-2}\text{s}^{-1}$, which is not common for Hall-B. To run above 500 nA the “beam blocker” will need to be upgraded to handle higher power. The beam blocker attenuates the beam seen by the Faraday cup. This blocker is constructed of copper and is water cooled. Hall B staff have indicated that this is a rather straightforward engineering task and has no significant associated costs [68].

Straw Target We also expect JLab to design and build the target for the experiment as it will be a very similar target as the ones build for CLAS BONuS and eg6 runs. See section 3.3.3 for more details.

Mechanical Integration We also expect Jefferson Laboratory to provide assistance in the detector installation in the Hall. This will include providing designers at ANL and IPNO with the technical drawings required to integrate ALERT with CLAS12. We will also need some coordination between designers to validate the mechanical integration.

CLAS12 DAQ Integration We also will need assistance in connecting the electronics of ALERT to the CLAS12 data acquisition and trigger systems. This will also include help integrating the slow controls into the EPICs system.

Chapter 4

Proposed Measurements

The proposed measurements of coherent DVCS and ϕ electroproduction off ${}^4\text{He}$ and their analyses are discussed in this chapter. For DVCS, the scattered electron, the real photon and the recoiling ${}^4\text{He}$ nucleus will all be detected. For coherent ϕ production, we require the detection of the scattered electron, the recoiling ${}^4\text{He}$ nucleus, and either a kaon pair for the identification of the ϕ meson through its invariant mass or a single kaon, and in that case, the missing kaon will be reconstructed through missing momentum and energy. For each process we first discuss an empirical model of the existing data and use this information in a Monte Carlo event generator. The kinematic coverage and projected statistical and systematic uncertainties are presented. In section 4.3 the impact parameter distributions from these two models is presented.

4.1 Exclusive Coherent DVCS

DCVS is the hard exclusive production of a real photon in lepton scattering. For coherent production, we have

$$e(\mathbf{P}_e) + {}^4\text{He}(\mathbf{P}_{4\text{He}}) \rightarrow e(\mathbf{P}'_e) + {}^4\text{He}(\mathbf{P}'_{4\text{He}}) + \gamma(\mathbf{P}_\gamma) \quad (4.1)$$

where $\mathbf{P}_e(\mathbf{P}'_e)$ is the four-momentum of the incoming (outgoing) electron. $\mathbf{P}_{\gamma^*} = \mathbf{P}_e - \mathbf{P}'_e$ is the four-momentum of the virtual photon and $\mathbf{P}_{4\text{He}}(\mathbf{P}'_{4\text{He}})$ is the four-momentum ${}^4\text{He}$ nucleus in the initial (final) state. The photon virtuality is $Q^2 = 4EE' \sin^2(\theta/2)$, where E and E' are

the energy of the incoming and outgoing electron respectively. The four-momentum transfer to the nucleus is:

$$t = (\mathbf{P}_{4\text{He}} - \mathbf{P}'_{4\text{He}})^2 = (\mathbf{P}_{\gamma^*} - \mathbf{P}_\gamma)^2. \quad (4.2)$$

Other variables of interest are ϕ the angle between the lepton scattering angle and photon production plane, $\nu = E - E'$ is the energy of the virtual photon. The kinematical cuts on the detected electron are:

- $Q^2 > 1 \text{ GeV}^2$: to ensure that the interaction occurs at the partonic level and the applicability of factorization in the DVCS handbag diagram.
- $-t > -t_{min}$: the transferred momentum squared to the recoil ${}^4\text{He}$ has to be greater than a minimum value defined by the kinematics of the beam and the scattered electron as:

$$t_{min} = -Q^2 \frac{2(1-x_A)(1-\sqrt{1+\varepsilon^2}) + \varepsilon^2}{4x_A(1-x_A) + \varepsilon^2}, \quad (4.3)$$

For all events, the scattered electron and the real photon will be detected in the CLAS12 spectrometer while the recoiling ${}^4\text{He}$ nucleus will be detected in the ALERT detector. For both CLAS12 and ALERT, we use a FastMC package based on GEANT4 to simulate detector's acceptance. The different CLAS12 detector's resolutions were taken from CLAS12 fastMC. While for ALERT, we used parametrization of the resolutions obtained from the GEANT4 simulations described in section 3.4.

Figure 4.1 shows the correlations between Q^2 , x_B and $-t$ variables which are determined by the acceptance of CLAS12 for electrons and ALERT for the recoiling ${}^4\text{He}$ nuclei. Figure 4.2 shows the correlation between the azimuthal angle ϕ and the polar angle θ in the laboratory frame for all detected particles from the coherent DVCS channel. The electron's ϕ versus θ distribution show the six CLAS12 sectors. Figure 4.3 presents the resolutions for the kinematic variables Q^2 , x_B , t and ϕ .

We define the additional four-vectors:

$$\mathbf{P}_X^{e^4\text{He}\gamma} = \mathbf{P}_{\gamma^*} + \mathbf{P}_{4\text{He}} - (\mathbf{P}_\gamma + \mathbf{P}'_{4\text{He}}) \quad (4.4)$$

$$\mathbf{P}_X^{e^4\text{He}} = \mathbf{P}_{\gamma^*} + \mathbf{P}_{4\text{He}} - \mathbf{P}'_{4\text{He}} \quad (4.5)$$

$$\mathbf{P}_X^{e\gamma} = \mathbf{P}_{\gamma^*} + \mathbf{P}_{4\text{He}} - \mathbf{P}_\gamma \quad (4.6)$$

In order to access the beam spin asymmetry, one need to identify exclusive DVCS-BH events. To ensure exclusivity, only events with a good electron, one real photon and a recoiling ${}^4\text{He}$

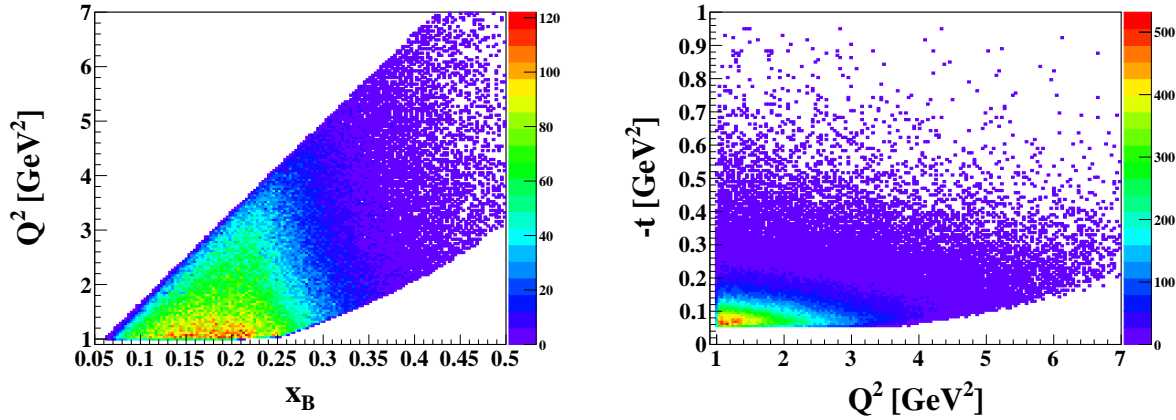


Figure 4.1: Left: correlation between Q^2 and x_B . Right: correlation between $-t$ and Q^2 for coherent DVCS off ${}^4\text{He}$.

are selected as coherent events. To reduce even more the contribution of non-exclusive events, the following kinematical cuts have to be applied:

- For exclusive coherent DVCS, the virtual photon, the emitted real photon and the recoil helium have to be coplanar. The coplanarity angle ($\Delta\phi$) defined as the difference in angle between these two planes: the first defined by the virtual photon and the recoiling ${}^4\text{He}$ and the second defined by the real photon and the virtual one.
- Missing energy, mass and transverse momentum ($p_X^T = \sqrt{(p_X^x)^2 + (p_X^y)^2}$) cuts on $\mathbf{P}_X^{e^4\text{He}\gamma}$.
- Missing mass cuts on the $e^4\text{He}X$ and $e\gamma X$ systems, which are defined as $(\mathbf{P}_X^{e^4\text{He}})^2$ and $(\mathbf{P}_X^{e\gamma})^2$ respectively.
- Cone angle cut between the measured real photon and the missing particle in the $e^4\text{He}X$ configuration. It is defined as:

$$\theta(\gamma, e^4\text{He}X) = \cos^{-1} \left(\frac{\vec{\mathbf{P}}_\gamma \cdot \vec{\mathbf{P}}_X^{e^4\text{He}}}{|\vec{\mathbf{P}}_\gamma| |\vec{\mathbf{P}}_X^{e^4\text{He}}|} \right). \quad (4.7)$$

Even with all the previously presented exclusive cuts, the selected events are not all true DVCS events. In our kinematic region, the main contamination comes from the exclusive electroproduction of π^0 ($e^4\text{He} \rightarrow e^4\text{He}\pi^0 \rightarrow e^4\text{He}\gamma\gamma$), in which one of the two photons from the π^0 decay passes the requirements for the DVCS events. These events can however be

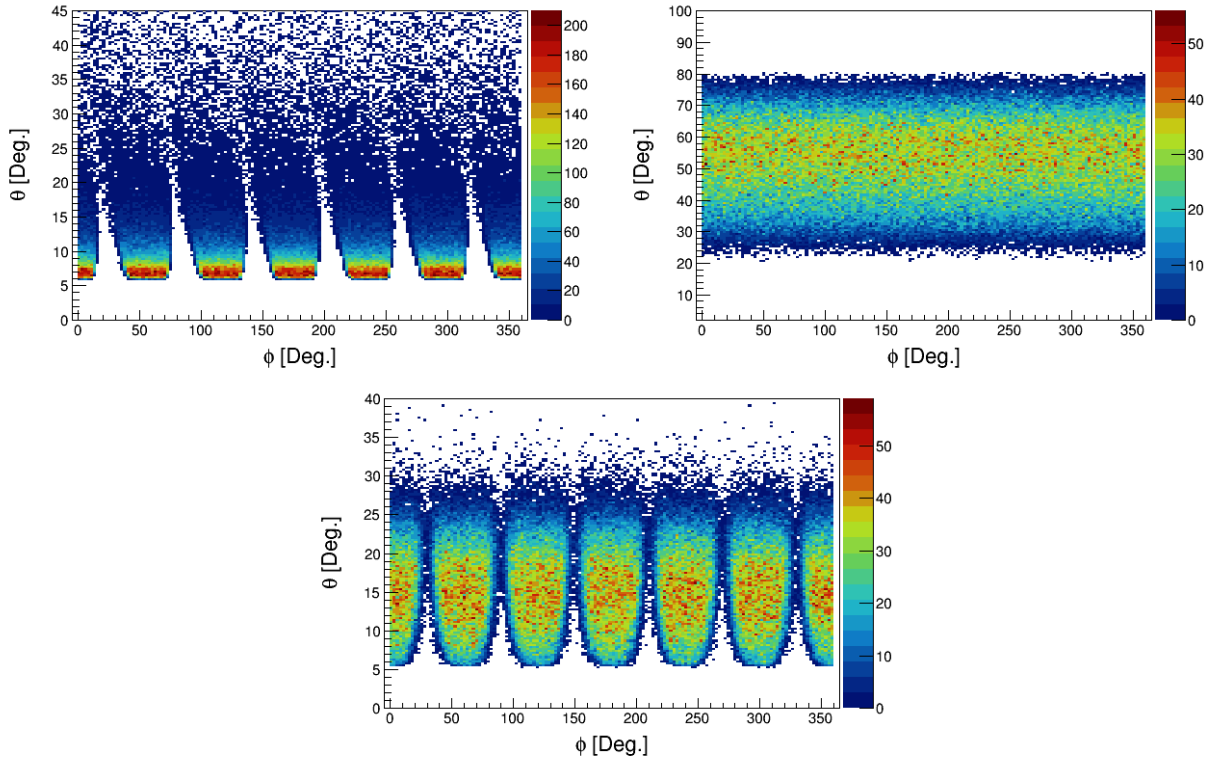


Figure 4.2: The angles θ and ϕ in the lab frame for all detected particles in coherent DVCS off ${}^4\text{He}$. Top-left: the electron, top-right: the ${}^4\text{He}$ nucleus, and bottom: the real photon.

subtracted to obtain the true number of DVCS events based on the experimentally measured number of $e^4\text{He}\pi^0$ events.

Figure 4.4 illustrates the contributions of exclusive π^0 , with only one photon of the decay is detected, events to the coherent DVCS data sample. The number of simulated π^0 events is three times the number of the simulated single photon production events. The dependencies of the contamination from π^0 versus the exclusive distributions are shown in different panels of figure 4.4. The black histograms are the total simulated events (DVCS and π^0 events), while the blue histograms are for the simulated DVCS events only, and the red histograms are for the simulated π^0 events where only one photon of the π^0 two-photon decay is detected due to CLAS acceptance and may contaminate the DVCS sample. Figure 4.5 illustrates the effectiveness of the exclusivity cuts on reducing the background contamination to the coherent DVCS sample.

As mentioned previously, and as seen from the ratio of black to blue curves in figure 4.4, the simulated π^0 events were three times the number of the DVCS events. The true π^0 to

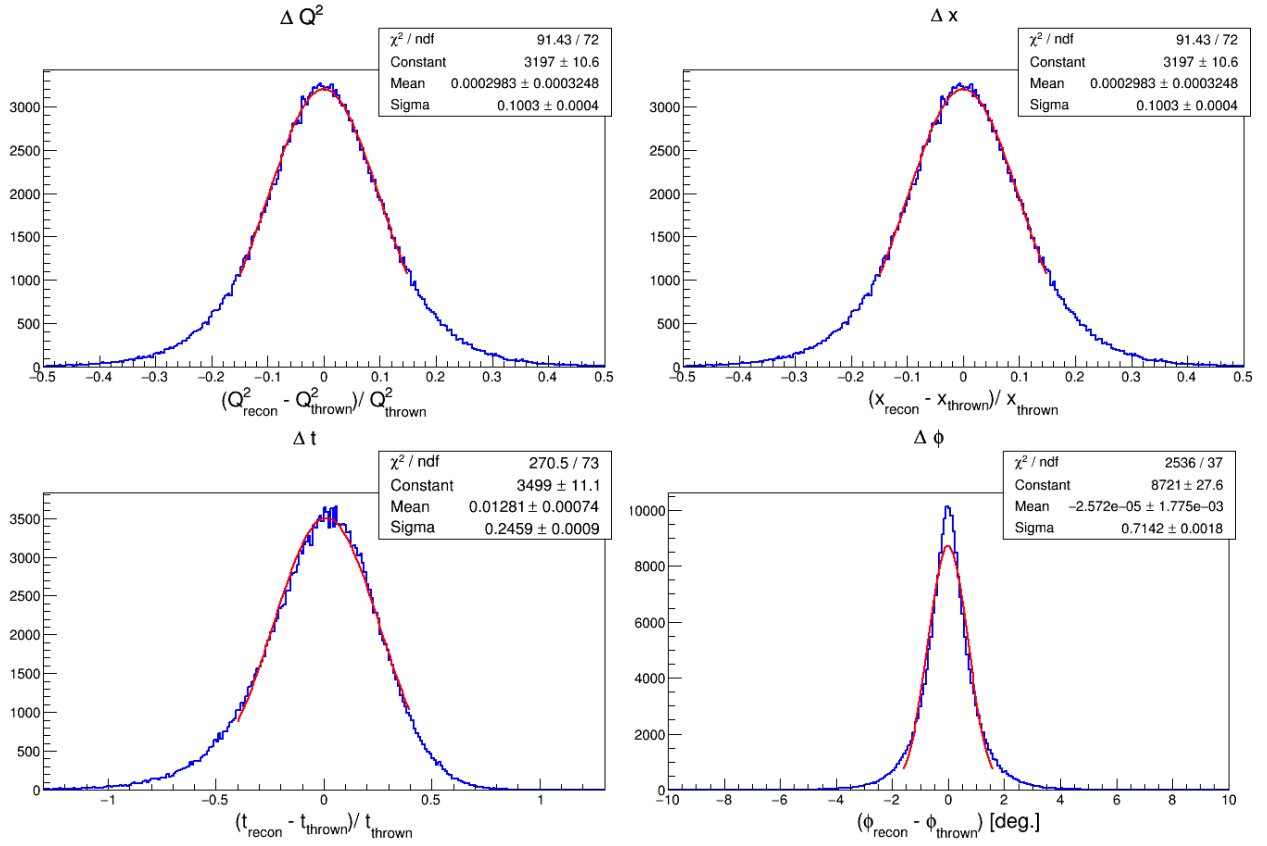


Figure 4.3: CLAS12 and ALERT resolutions for Q^2 , x_B , t and ϕ .

coherent DVCS production ratio has been measured in eg6-experiment [14] to be 5% to 20% as can be seen in figure 4.6.

Figure 4.5 shows the remaining π^0 events after the exclusivity cuts that contaminate the DVCS sample. The true number of the coherent DVCS events can be formulated as:

$$N_{e^4\text{He}\gamma}^{\text{True}} = N_{e^4\text{He}\gamma}^{\text{Exp.}} - N_{e^4\text{He}\pi^0(\gamma)}^{\text{Exp.}}, \quad (4.8)$$

where $N_{e^4\text{He}\gamma}^{\text{True}}$, $N_{e^4\text{He}\gamma}^{\text{Exp.}}$ and $N_{e^4\text{He}\pi^0(\gamma)}^{\text{Exp.}}$ are the true number of coherent DVCS events, the experimentally measured number of $e^4\text{He}\gamma$ events and the contamination number, respectively. The contamination can be calculated by using real data and simulation. We define, for each kinematic bin and for each beam helicity state

$$N_{e^4\text{He}\pi^0(\gamma)}^{\text{Exp.}} = \frac{N_{e^4\text{He}\pi^0(\gamma)}^{\text{Sim.}}}{N_{e^4\text{He}\pi^0(\gamma)}^{\text{Sim.}}} * N_{e^4\text{He}\pi^0(\gamma)}^{\text{Exp.}}, \quad (4.9)$$

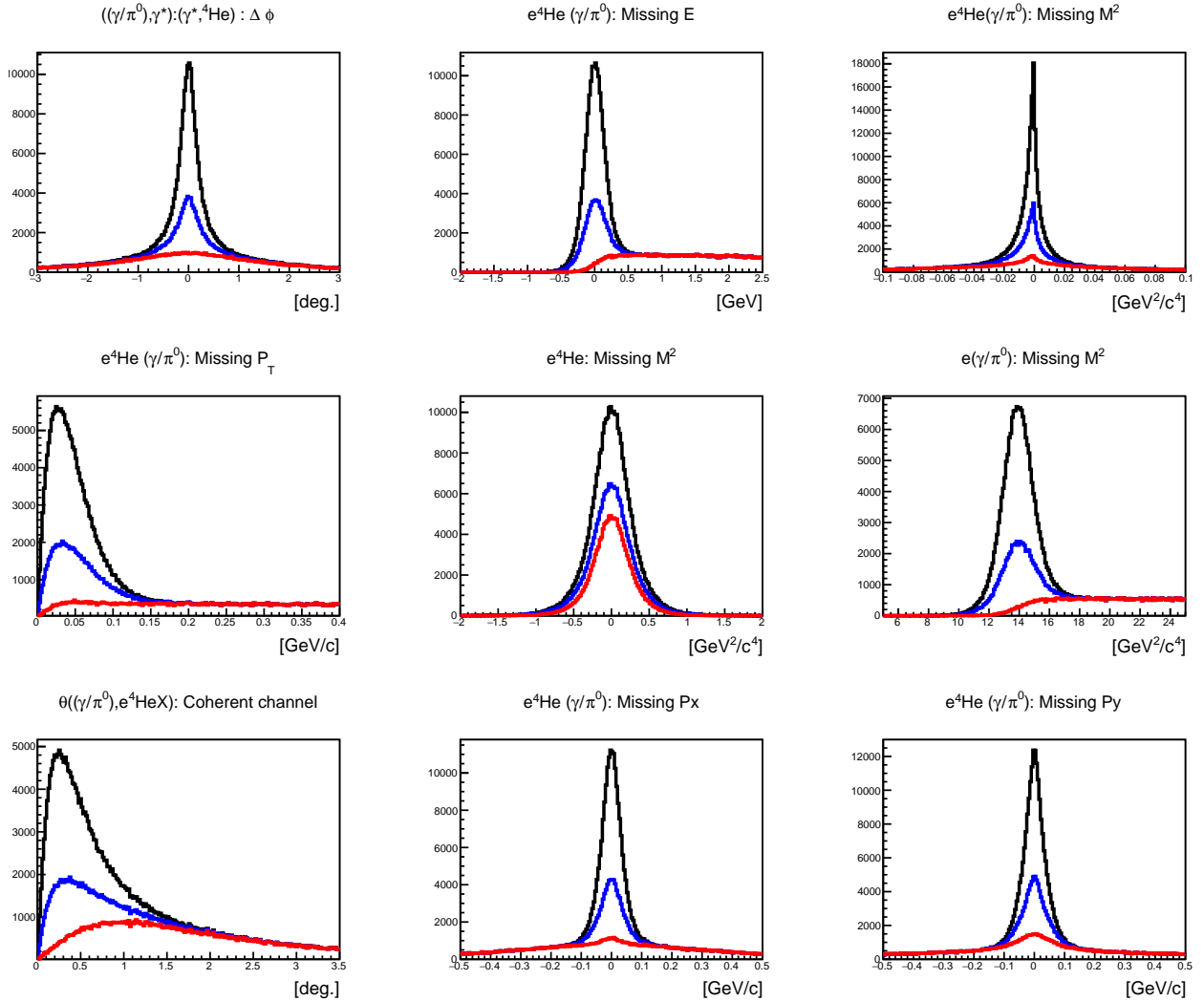


Figure 4.4: Contribution of non-exclusive (π^0) events to coherent DVCS sample. The blue curves represent the DVCS events. The black curves are the sum of the contributions from exclusive and non-exclusive events. The red curves show the π^0 events where only one photon of the π^0 two-photon decay is detected.

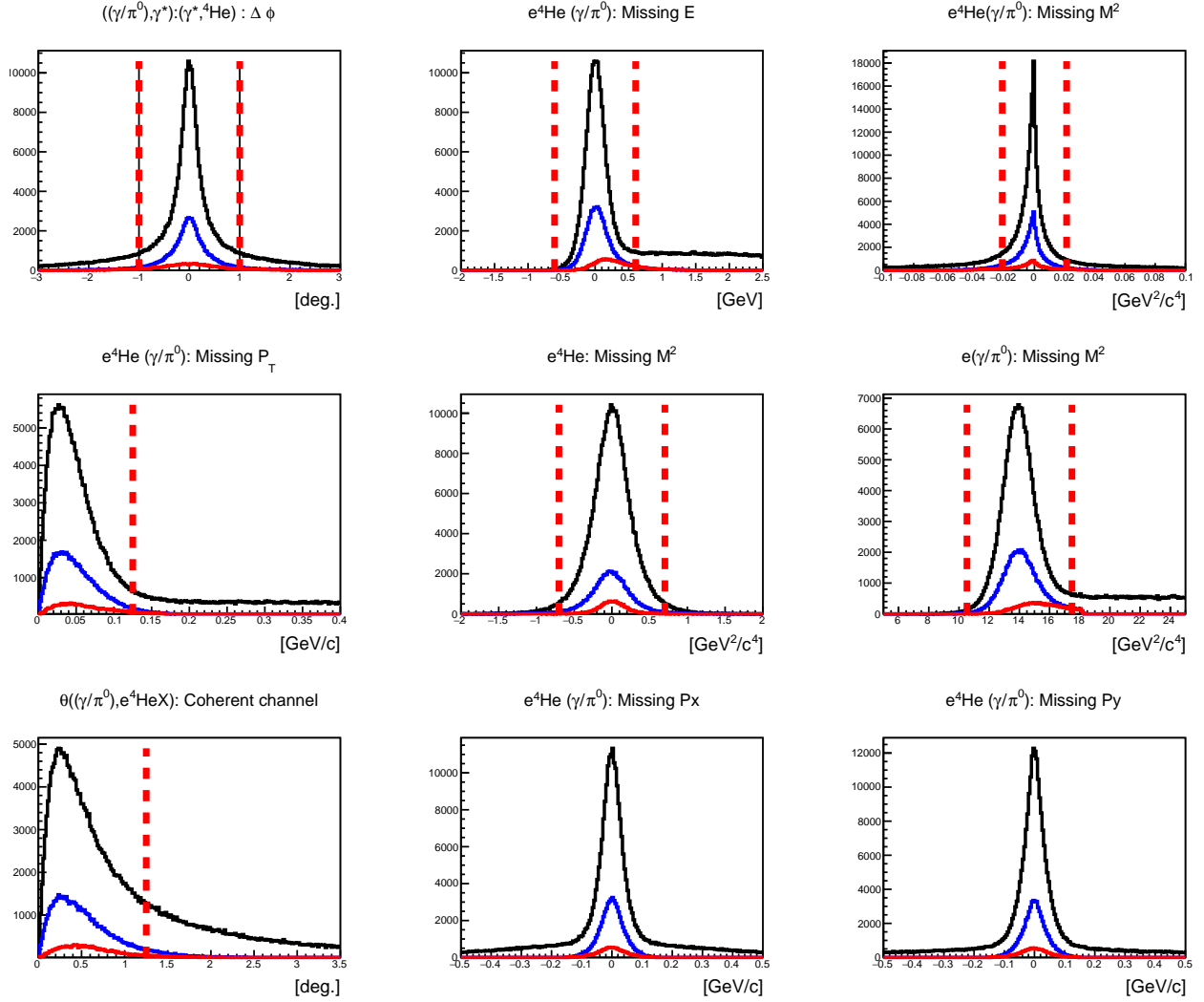


Figure 4.5: The effectiveness of the exclusivity cuts on reducing the background contamination to the coherent DVCS sample. The black curves are for the exclusive and non-exclusive events before exclusivity cuts. The blue curves are for the coherent DVCS events which satisfied the exclusivity conditions except for the cuts on the variable being displayed. The red histograms are for the π^0 background contamination that satisfied the exclusivity conditions. The red vertical lines represent 3σ cuts on each exclusive variable. The missing momentum in x and y directions in the configuration $e^4\text{He}\gamma X$, are shown for information. See the text for the definition of the shown exclusive variables.

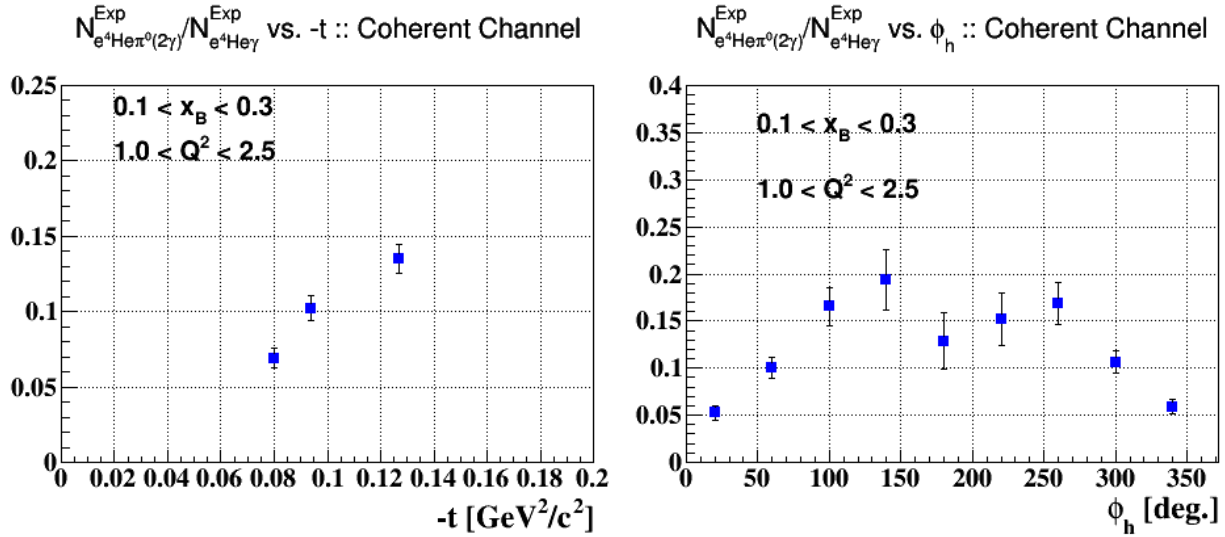


Figure 4.6: The π^0 to coherent DVCS production yield versus four-momentum transfer ($-t$) integrated over the photon angle ϕ (left), and versus ϕ (right) integrated over t as determined from CLAS-eg6 analysis [14]. Both plots are for $1.0 \text{ GeV}^2 < Q^2 < 2.5 \text{ GeV}^2$ and $0.1 < x_B < 0.3$.

where $N_{e^4\text{He}\pi^0(\gamma\gamma)}^{\text{Exp.}}$ is the number of measured $e^4\text{He}\pi^0$ events, for which both photons of the π^0 have been detected. The quantity $\frac{N_{e^4\text{He}\pi^0(\gamma)}^{\text{Sim.}}}{N_{e^4\text{He}\pi^0(\gamma\gamma)}^{\text{Sim.}}}$ is the acceptance ratio for detecting an $e^4\text{He}\gamma$ event that originates from an $e^4\text{He}\pi^0$ event. It can be derived from Monte-Carlo simulations by generating and simulating $e^4\text{He}\pi^0$. $N_{e^4\text{He}\pi^0(\gamma)}^{\text{Sim.}}$ is the number of such events passing the DVCS requirements, while $N_{e^4\text{He}\pi^0(\gamma\gamma)}^{\text{Sim.}}$ is the number of simulated $e^4\text{He}\pi^0$ events passing the exclusivity cuts for $e^4\text{He}\pi^0$ events.

Figure 4.7 shows the coherent acceptance ratio as a function of ϕ_h using the CLAS12-ALERT setup. The mean value of the acceptance ratio for the coherent channel is around 8%.

The polarized beam of CEBAF and the large acceptance of CLAS will allow us to extract the beam spin asymmetry A_{LU} for various bins in Q^2 , x_B , and t and ϕ for both the coherent DVCS and the π^0 electroproduction processes. The beam spin asymmetry in each bin is defined as:

$$A_{LU} = \frac{1}{P_B} \frac{N^+ - N^-}{N^+ + N^-}. \quad (4.10)$$

where P_B is the beam polarization, and N^+ and N^- are the number of events detected with

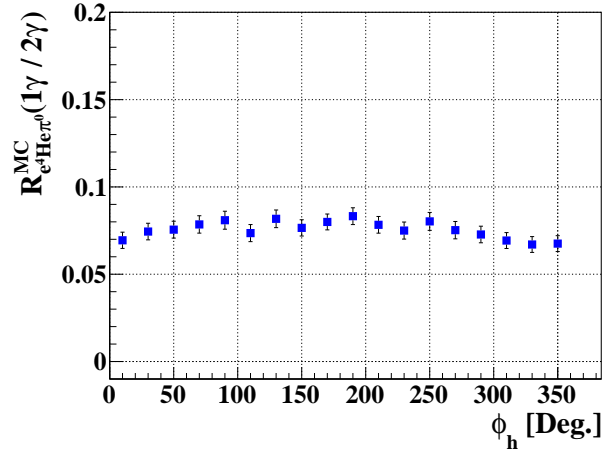


Figure 4.7: The coherent DVCS acceptance ratio as a function of ϕ integrated over $t = 0.06 \text{ GeV}^2$ to 0.2 GeV^2 , $Q^2 = 1.0 \text{ GeV}^2$ to 2.5 GeV^2 , and $x_B = 0.1$ to 0.3 using both CLAS12 and ALERT detectors.

positive and negative electron helicity, respectively. The statistical uncertainty of A_{LU} is

$$\sigma_{A_{LU}} = \frac{1}{P_B} \sqrt{\frac{1 - (P_B A_{LU})^2}{N}} \quad (4.11)$$

where $N(= N^+ + N^-)$ is the total number of measured events.

4.1.1 Event Generator

In order to make projections of our results, we have used the following parametrization of the cross section which parameters were calibrated to reproduce the DVCS and exclusive π^0 electroproduction data from CLAS at 6 GeV [69]:

$$\frac{d^4\sigma}{dQ^2 dx_B dt d\phi} \propto \left(\frac{Q_0^2}{Q^2}\right)^\alpha \frac{1}{1 + \left(\frac{x_B - x_c}{c}\right)^2} \frac{1}{(1 + bt)^\beta} (1 - d(1 - \cos(\phi))). \quad (4.12)$$

This parametrization is the product of four factors which reproduce the DVCS and π^0 , characteristics as follows:

- the Q^2 -dependent term with: Q_0^2 the minimum allowed value and α a parameter which controls the shape of the distribution.

- the x_B term accounts for the dependence of the cross section on the parton distribution functions, with x_c the mean value of the Bjorken variable x_B .
- the t term accounts for the t -dependence of the elastic form factors of the helium and of the proton, via the parameters b and β .
- the ϕ term accounts for the cross section dependence on this angle, via the parameter d .

To reflect the change in the center of mass energy due to the higher beam energy of this proposal compared to E08-024 experiment, the parameter x_c (the mean value of x_B) is calculated from the DIS mean kinematic values, while the parameters b and β were scaled with respect to the center of mass energy change from 6 GeV to 11 GeV. Table 4.1 shows the values of the parameters used for the cross section parametrization of the four channels of interest: $e^4\text{He}\gamma$, $e^4\text{He}\pi^0$, $ep\gamma$, and $ep\pi^0$. Figure 4.8 shows a comparison between the experimentally identified coherent DVCS events from eg6 dataset and the simulated DVCS events as a function of the kinematic variables Q^2 and x_B .

Parameter	Units	$e^4\text{He}\gamma$	$e^4\text{He}\pi^0$	$ep\gamma$	$ep\pi^0$
Q_0^2	GeV ² /c	1.0	1.0	1.0	1.0
α		2.5	3.0	1.5	1.5
b	GeV ² /c	-6.0	-8.8	-1.408	-1.408
β		6.5	7.3	4.0	1.5
x_c		0.27	0.3	0.2	0.5
c		0.2	0.3	0.2	0.5
d		0.4	0	0.4	0

Table 4.1: Values of the parameters used in DVCS event generator.

4.1.2 Projections

The projected precisions of the beam-spin asymmetries and Compton form factor for DVCS on ^4He are presented in this section. Based on the Impulse Approximation model [22], the real and the imaginary parts of the ^4He CFF were calculated and fed into our event generator to produce coherent DVCS events with beam-spin asymmetries following the

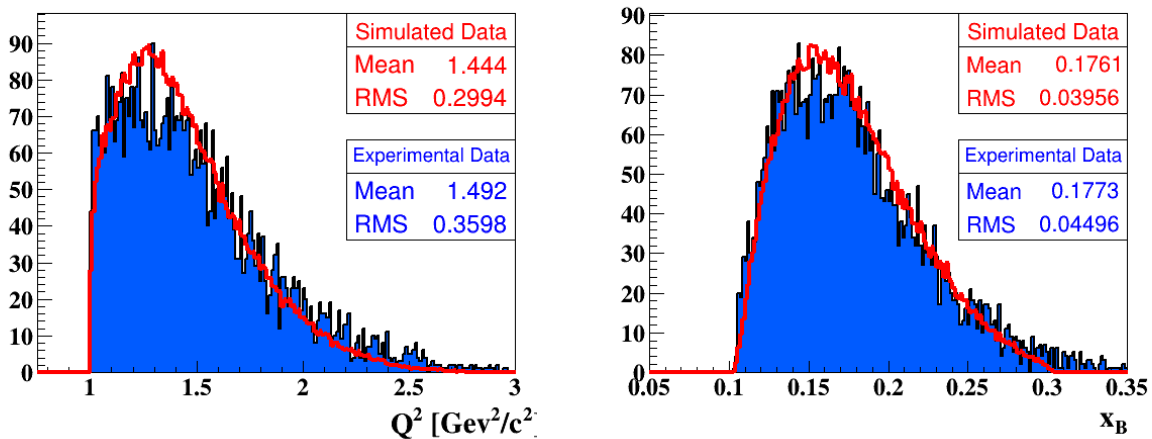


Figure 4.8: Comparison between the simulated $e^4He\gamma$ DVCS events (in red lines) and the experimental DVCS events from eg6 (in shaded blue) with 6 GeV beam as a function of the kinematic variables: Q^2 and x_B [14].

formalism presented in chapter 2. Figure 4.9 presents the t dependence of the real and the imaginary parts of the ^4He CFF at different values of x_B .

Figure 4.10 shows the proposed binning in x_B versus $-t$ space. The simulated data is integrated over the full Q^2 range. For the BSA A_{LU} dependence on $-t$, the data has been binned into three bins in x_B , 7 bins in $-t$ and 12 bins in ϕ . The statistical error bars are calculated for 20 days at a luminosity of $0.75 \times 10^{34} \text{ cm}^{-2}\text{s}^{-1}$ per nucleus (jointly with Tagged EMC proposal request) and 10 days at a luminosity of $1.5 \times 10^{34} \text{ cm}^{-2}\text{s}^{-1}$ per nucleus specifically dedicated to this proposal. The assumed beam polarization is 80%. Figure 4.11 shows the reconstructed beam-spin asymmetries as a function of the angle ϕ for two bins in $-t$ at a fixed x_B value presenting a high and a low statistic bins. The projected precision of A_{LU} at ϕ equal to 90° for the different bins is presented in figure 4.12. The projected uncertainties on the reconstructed real and imaginary parts of the CFF are shown in figure 4.13.

For the purpose of validating our projection results, that are extracted based on the parametrized cross section from CLAS-EG6 experiment, we performed an additional exercise. In Appendix B, we extracted our projections based on generating and simulating pure coherent BH events, which dominates most of the accessible phase-space of JLAB. In conclusion, our projections are well reproduced, within the statistical error bars, by the well-known pure BH process.

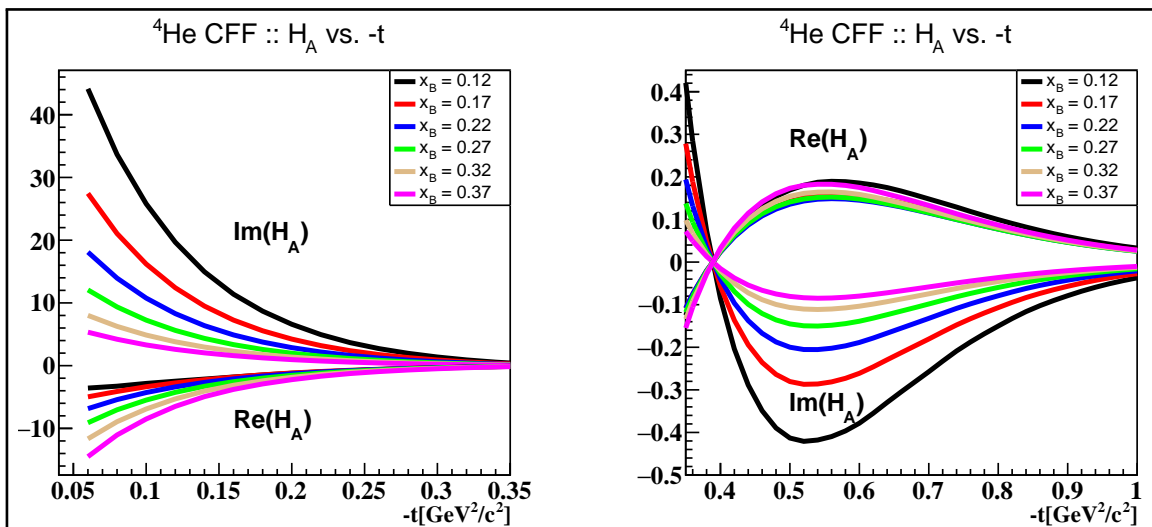


Figure 4.9: From the impulse approximation model, the imaginary and the real part of the ${}^4\text{He}$ CFF as a function of $-t$, low $-t$ on the left and high $-t$ on the right, at fixed x_B values.

4.1.3 Systematic uncertainties

It is particularly convenient to use the BSA A_{LU} as a DVCS observable, because most of the experimental systematic uncertainties, such as normalization and efficiencies that appear in the cross sections cancel out in the asymmetry ratio. However, some systematic uncertainties remain and they still contribute to the measured A_{LU} . The main known sources of systematic uncertainties are: the DVCS selection cuts, the fitting sensitivity to our binning, the beam polarization and the background (non exclusive π^0) acceptance ratio. In the following, we present estimates of the contribution from each source based on our prior knowledge during CLAS-eg6 DVCS analysis [14] and our simulation studies of the proposed ALERT detector.

In order to evaluate the systematic uncertainties stemming from the DVCS selection cuts, the eg6-analysis was repeated with changing the width of the exclusive cuts. The resulting systematic uncertainty to the A_{LU} asymmetry was around 8% for the coherent DVCS channel. Because of the important improvement we expect with ALERT in terms of resolutions, we expect this uncertainty to be reduced to 5%.

Regarding the sensitivity of the fit results to our binning, the eg6 data were binned into two different bins in ϕ and the reconstructed asymmetries were compared. The associated systematic uncertainty for A_{LU} at $\phi = 90^\circ$ was found to be of 5.1%. For the proposed measurements, we expect to achieve higher statistics and therefore we reduced the expected

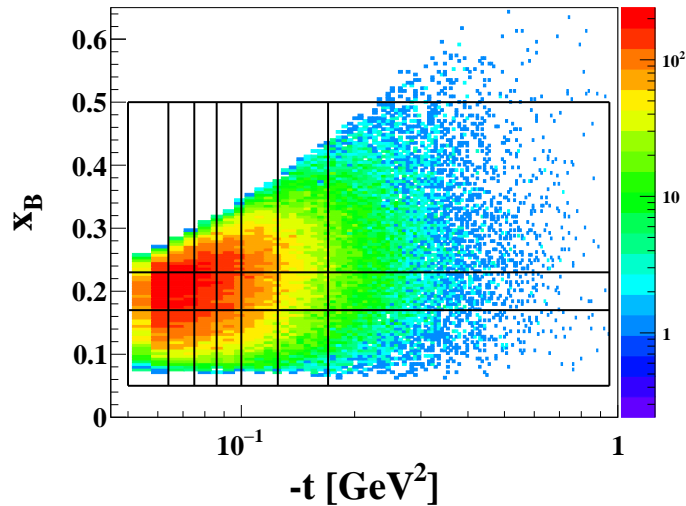


Figure 4.10: Data binning in x_B vs $-t$ space.

systematics to 3%.

The beam polarization will be measured during the experiment by the Hall B Møller polarimeter. This polarimeter measures the angular distribution of the Møller electrons to obtain the beam polarization. The precision of the Hall B Møller polarimeter was measured to be around 3.5% [70], which is expected to be improved with the upgrade. We assume therefore a 3.5% systematic uncertainty on the measured asymmetries similar to what was achieved during 6 GeV run.

To estimate the systematic uncertainty associated with the calculated acceptance ratio (R), two techniques can be used. The first is via repeating the analysis by implementing R differently, while the second technique is by using two generating models to calculate R. In CLAS-eg6 analysis both methods were investigated. A maximum variation of 0.6% has been observed on the coherent A_{LU} at $\phi = 90^\circ$. An upper limit of 1% is assumed for the proposed measurements.

The total systematic uncertainty on the measured A_{LU} at $\phi = 90^\circ$ is the quadratic sum of the previously described individual uncertainties. Table 4.2 summarizes the systematic uncertainties for both CLAS-eg6 and the proposed measurements.

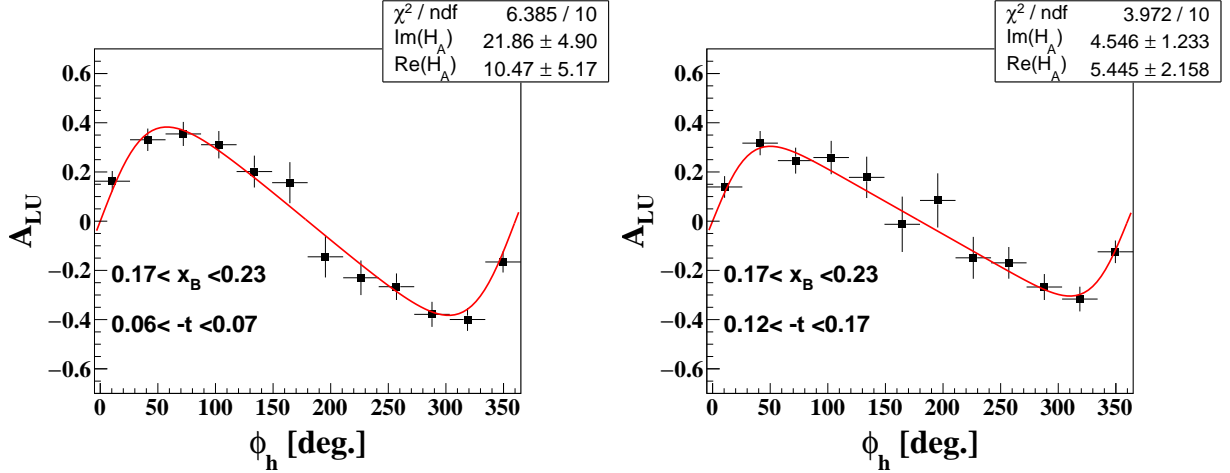


Figure 4.11: The coherent beam-spin asymmetry projections as a function of the angle ϕ between the leptonic and the hadronic planes, for two different bins $-t$ at the same x_B range, integrated over Q^2 range. The red solid curves represent a fit to the data in the full form of the asymmetry, equation 2.14, with the real and the imaginary parts of the CFF as the free parameters of the fit.

Systematic source	CLAS-EG6	Proposed experiment	Systematic type
DVCS cuts	8%	5%	bin to bin
Data binning	5.1%	3%	bin to bin
Beam polarization	3.5%	3.5%	Normalization
Acceptance ratio	0.6%	1%	bin to bin
Total	10%	7%	bin to bin

Table 4.2: The systematic uncertainties on the measured coherent beam-spin asymmetries at $\phi = 90^\circ$ from CLAS-eg6 and the proposed experiment.

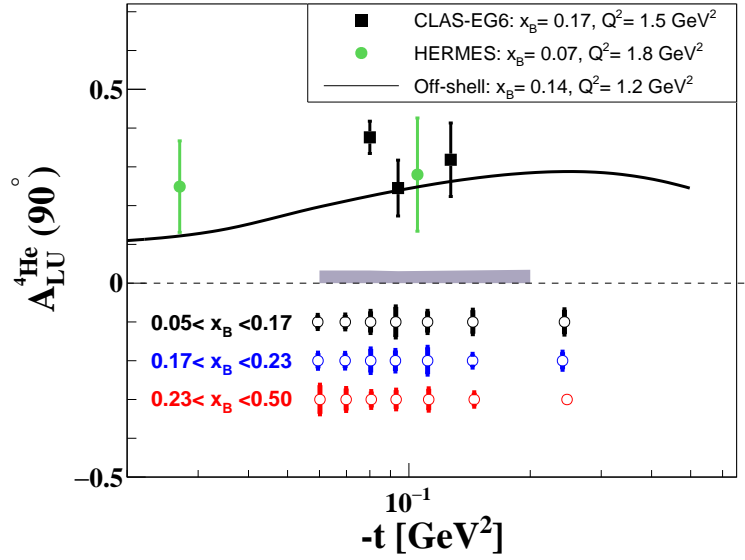


Figure 4.12: Projected precision for the $A_{LU}(90^\circ)$, from the fit, for coherent DVCS on ^4He versus $-t$ compared to the previous measurements from CLAS-eg6 (black squares), HERMES (green circles) and spectral function calculations (LT curves).

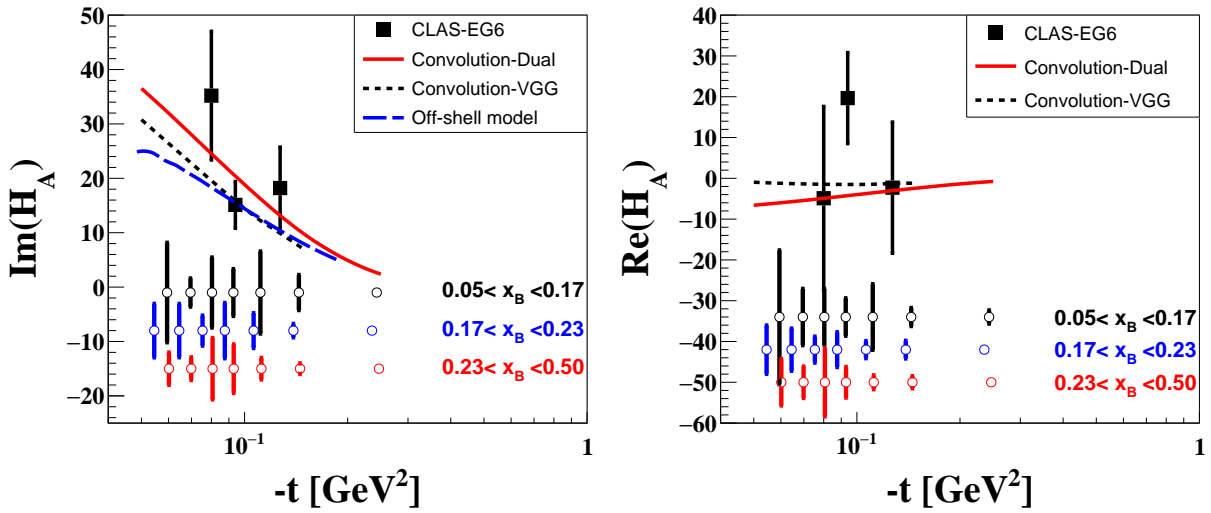


Figure 4.13: The projected statistical uncertainties for the imaginary (top) and real (bottom) parts of the CFF H_A , from the fits, as a function of $-t$ at fixed ranges in x_B

4.2 Exclusive ϕ Electroproduction

The CLAS12 detector will be used to detect one electron along with either a single kaon or a kaon pair, while the ALERT detector will detect the recoiling ${}^4\text{He}$. The detected electron is constrained to the forward CLAS12 acceptance, and Figure 4.14 shows the expected kinematic coverage after acceptance. The CLAS12 detector acceptance was simulated using the java-based fastMC, with resolution smearing taken from the older fortran fastMC. ALERT detector acceptance was taken from the above sections and 351 simulation results.

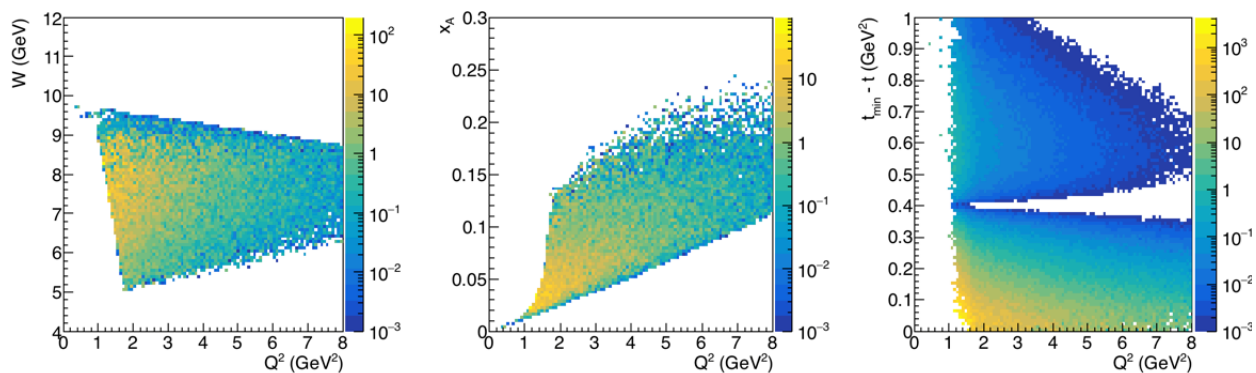


Figure 4.14: Total cross-section weighted kinematic distributions for electron, kaon, and ${}^4\text{He}$ coincidence events from ϕ production simulations. Z-axis units are in nb.

In the case of a single kaon, the missing kaon will be reconstructed through missing momentum and energy. The missing 4-vector will be constrained to have a kaon mass, and the reconstructed 4-vector of the kaon and the missing kaon will be constrained to have an invariant mass of the ϕ mass. Figure 4.15 shows the reconstructed mass of a missing K^- after smearing the electron and K^+ with fastMC resolution smearing, and the detected ${}^4\text{He}$ with a momentum resolution in the ALERT detector of $\Delta p < 10\%$. A cut can then be made on the missing kaon mass from 0.2 to 0.8 GeV^2 to help eliminate background. The ALERT detector resolution drives both the missing kaon mass resolution and the resolution of the t -variable calculation. Figure 4.16 shows the expected $(t - t_{min})$ -bin migration after resolution effects.

4.2.1 Production and Background Rates

In Figure 4.17, the expected counts per day for the primary decay channel is shown versus t . In this calculation, the total luminosity is assumed to be 7.5×10^{33} nuclei/cm²/s, and the kaon and alpha detection efficiency is set at 50% in addition to the simulated acceptance as

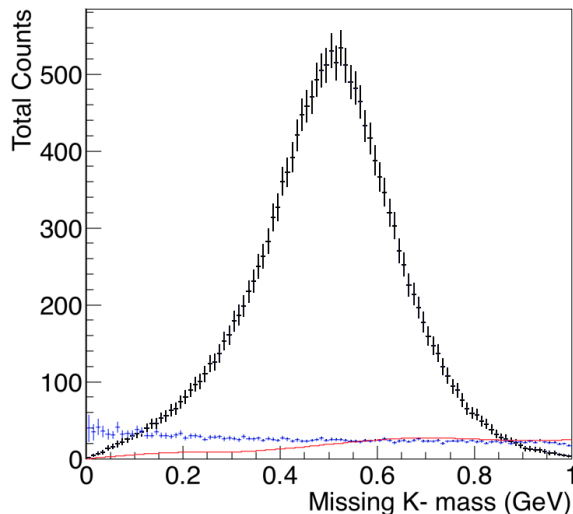


Figure 4.15: The black histogram shows the expected K^- mass resolution from reconstruction using the electron and K^+ detected in CLAS12, and ${}^4\text{He}$ detected in ALERT with counts for proposed running time. The light-blue histogram presents the estimated background from coherent $\omega \rightarrow \pi^+\pi^-\pi^0$ and $\rho \rightarrow \pi^+\pi^-$, with a misidentified K^+ and a production cross-section 1000 times the ϕ cross-section. The red histogram estimates a misidentified ${}^3\text{He}$ or ${}^2\text{H}$ incoherent background using PYTHIA. See text for details.

an additional safety margin on the expected counts. In addition to the $\phi \rightarrow K^+ K^-$ channel, we can gain additional statistics from the $\phi \rightarrow K_L^0 K_S^0$ channel, with $K_S^0 \rightarrow \pi^+ \pi^-$. In this case, the $\pi^+ \pi^-$ pair detection is assumed to have an efficiency of 70% in addition to the simulated acceptance.

Kaon PID will be performed through a combination of the TOF and veto from the LTCC, as proposed in PR12-12-007[25]. At kaon momenta < 5 GeV, the TOF will provide a $1\text{-}\sigma$ or better separation of kaons and pions. In combination with the charged pion momentum threshold of 2.5 GeV/c for the LTCC, kaon PID is not expected to be an issue. An additional cross-check of kaon identification can be performed with the CLAS12 RICH detector.

Background pion rates are expected to be small when the ALERT detector is required to tag a recoiling ${}^4\text{He}$ in the event; in this case, most pion background will come from non- ϕ meson production which can be cleaned up through missing mass cuts on the missing Kaon and reconstructed ϕ . For estimation of this background, phase-space for $\rho \rightarrow \pi^+ \pi^-$ and $\omega \rightarrow \pi^+ \pi^- \pi^0$ was generated. Since a comprehensive cross-section calculation and parameterization for ρ/ω electroproduction off ${}^4\text{He}$ is non-trivial and somewhat outside the scope of the analysis, the cross-section for both ρ and ω is estimated to be 1000 times the ϕ cross-section.

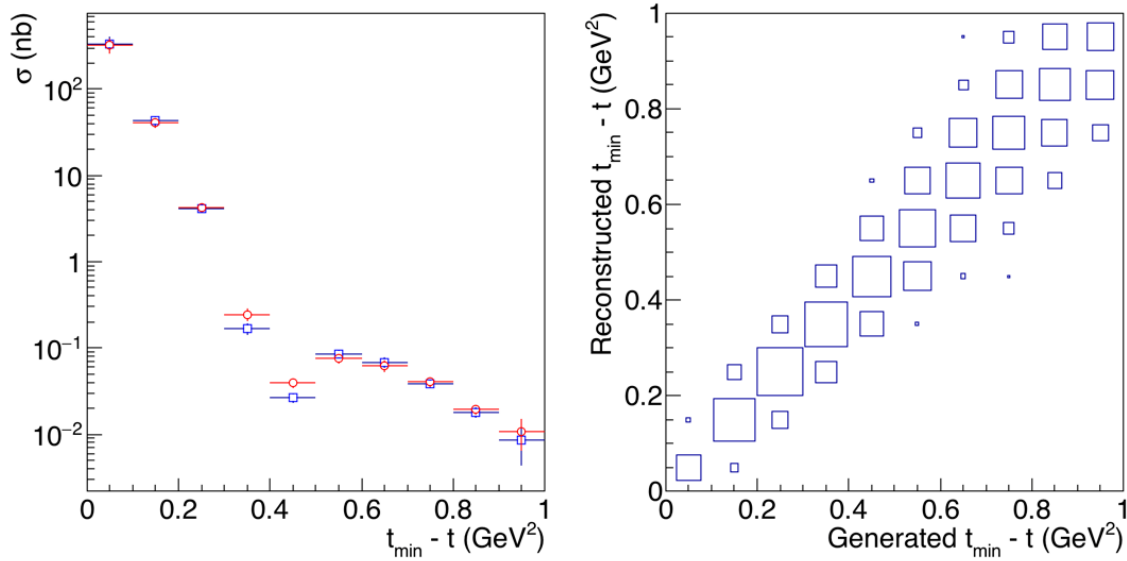


Figure 4.16: Quantification of t bin migration effects are shown in these two plots. The left plot shows cross-section versus reconstructed $t_{min} - t$ with red-circles, and the input generated $t_{min} - t$ with blue squares. On the right, reconstructed versus generated $t_{min} - t$ is plotted, which illustrates the expected bin-migration.

This factor of 1000 is a conservative estimate based on the ratio of rho/omega to phi production cross-sections off the proton at JLab6 energies, which are on the order of a few hundred times larger. Misidentification of the pions or protons as kaons is simulated according to the expected TOF separation at low-momentum, and with a conservative 95% rejection in the LTCC above 3 GeV momentum for pions. The results are shown in Figure 4.15. Another possible source of contamination will come from misidentification of ^4He in the ALERT detector. described above, should still provide a very clean separation of background.

A PYTHIA simulation for $\gamma + N \rightarrow X$ was performed, forcing a re-scattering between the recoil nucleon and the residual nucleus in ^4He . Re-scattering is required since a residual ^3He nucleus, with a residual momentum equal to its fermi-momentum from being bound in a ^4He , is almost completely outside ALERT's momentum acceptance. If the re-scattered ^3He or ^2H enters ALERT acceptance, it is assumed to have a ^4He misidentification probability of 10% (upper limit of expected misidentification). True kaons and misidentified protons or pions are also accepted in CLAS12 as described above and the total rate is calculated assuming the experiment's production luminosity. The total rate per day using worst-case estimates is calculated to be approximately 25 (or less than one-tenth the production rate), averaged over the entire accepted phase-space. This should not greatly impact the ϕ identification. The estimated counts from this background are also shown in Figure 4.15 for comparison to

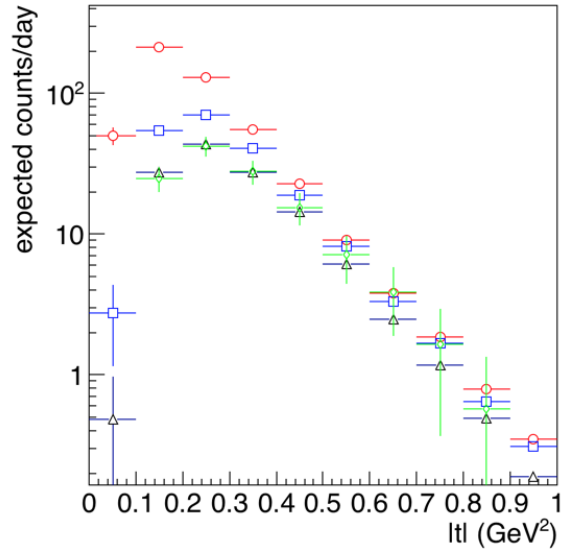


Figure 4.17: Expected counts per day for coherent ϕ production. Three analysis channels that will be investigated include the fully exclusive $K^+ K^-$ (black-triangles), missing K^- (red-circles), missing K^+ (blue-squares), and missing K_L^0 with $K_S^0 \rightarrow \pi^+ \pi^-$ (green-diamonds).

the signal peak.

4.2.2 Event Generator

Event generation for ϕ production off ${}^4\text{He}$ is done in two steps. First, the cross-section for ϕ production off a proton target is generated, and then the charge form-factor of ${}^4\text{He}$ is folded in, while the corresponding charge form-factor for the proton is divided out. The phase-space for generation is created by sampling uniformly in Q^2 , x_B , and t .

Since the cross-section must first be calculated off the proton, the relevant value for t must be recalculated. For this we define a new variable t_p which is calculated assuming a target proton with a momentum uniformly distributed up to the ${}^4\text{He}$ fermi-momentum in the initial state, and a scattered proton with 1/4 the momentum of the recoiling ${}^4\text{He}$ with a uniformly distributed fermi-momentum in the final state. The cross-section is then given by:

$$\frac{d\sigma_{{}^4\text{He}e}(t)}{dt} = \frac{d\sigma_p(t_p)}{dt} \left(\frac{A F_{C,{}^4\text{He}}(t)}{F_{C,p}(t_p)} \right)^2 \quad (4.13)$$

where A is the nucleon number of ${}^4\text{He}$, and F_C the charge form factor of ${}^4\text{He}$ is parametrized

using the world data through its first minimum in t following: $F_{C,^4He} = (1 - (2.5t)^6)e^{11.7t}$. The calculation of the ϕ production cross-section off the proton follows the exact formalism as put forth by the accepted CLAS12 proposal PR12-12-007 [25] and discussed in section 2.3. The differential cross-section for the case of an unpolarized electron is

$$\frac{d^3\sigma}{dx_B dQ^2 dt} = \Gamma(x_B, Q^2, E) \left(\frac{d\sigma_T}{dt}(W, Q^2, t) + \varepsilon \frac{d\sigma_L}{dt}(W, Q^2, t) \right), \quad (4.14)$$

where the virtual photon flux is defined using the Hand [71] convention

$$\Gamma = \frac{\alpha}{2\pi} \frac{E'}{E} \frac{K}{Q^2} \frac{1}{1 - \varepsilon} \quad (4.15)$$

and $K = \nu - Q^2/2M$. The transverse cross-section is parameterized in W and Q^2 to fit world data as shown in Figure 2.9. The ratio of longitudinal to transverse cross-section is also fit to world data as a function of Q^2 and is shown in Figure 2.8. The t -dependence is incorporated as an exponential with a slope that depends on W . The exact functional forms for each of these is omitted here for brevity, but can be found in PR12-12-007 [25]. The total calculated cross-section for ϕ electroproduction off ^4He follows that formalism, except everywhere $d\sigma/dt$ enters the calculation, the calculation of Eqn. 4.13 is used instead. The plots of the cross-section versus world data from PR12-12-007 are shown in Figures 2.8 and 2.9.

4.2.3 Projections

The extraction of gluon GPDs will need the cross-section calculated in bins of Q^2 , x_V and $t_{min} - t$. The variable x_V is similar to x_A but takes into account the production of a vector meson with mass greater than zero, and is useful for direct comparison between DVMP and DVCS. A summary of the many different notations for x calculation using different target masses and vector masses is shown below:

$$x_V = \frac{Q^2 + M_V^2}{W^2 + Q^2 + M_{^4He}^2} = \left(\frac{Q^2 + M_V^2}{Q^2} \right) x_A \quad (4.16)$$

$$x_{Vp} = \frac{Q^2 + M_V^2}{W^2 + Q^2 + M_p^2} = \left(\frac{Q^2 + M_V^2}{Q^2} \right) x_B \quad (4.17)$$

The exact binning will depend on total run-time, but a feasible binning for the requested beam-time is shown in Figure 4.18. In this binning configuration, the largest occupancy bins

will have greater than 1000 signal events. The smaller occupancy bins can have 100 or less events, and may be folded together where necessary. Additionally, an identical binning to the DVCS analysis can be performed for a more direct comparison of results; the data are expected to overlap in much of the t , Q^2 and $x_{V,A}$ phase-space.

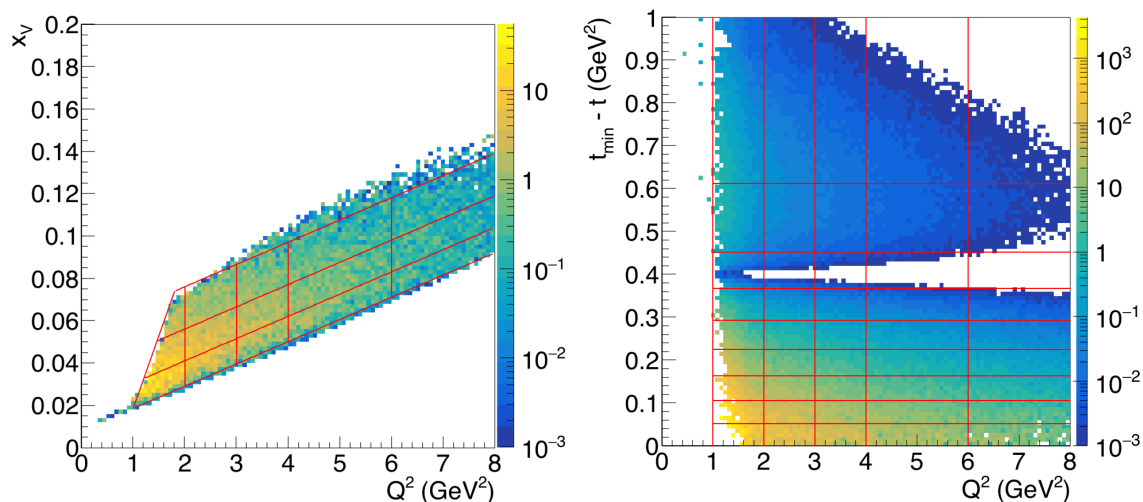


Figure 4.18: A possible binning over the accepted phase-space for gluon GPD extraction with ϕ production.

As discussed in section 2.3.1, to extract the ratio R , it is necessary to boost to the ϕ -helicity frame and fit the $\cos(\theta)$ distribution of one of the decay kaons, as described in Eqn. 2.21. The resolution of this θ distribution is highly dependent on the ALERT momentum resolution of the ^4He . Shown in Figure 4.19 is the extraction of r_{00}^{04} for a bin with $[0.02 < t - t_{min} < 0.04 \text{ GeV}^2]$, $[0.025 < x_V < 0.05]$, and $[1.5 < Q^2 < 2.0 \text{ GeV}^2]$. The two panels show the effect of resolution on the extraction; the left plot has standard CLAS12 resolutions plus a 5% momentum resolution for the ^4He detected by ALERT, and the right plot shows the same except a resolution of 10% in ALERT. The general characteristic of increasing resolution, is a flattening of the $\cos\theta$ distribution. Additional constraints may be able to improve the momentum resolution of the ALERT detector and even correct the θ distributions. For comparison, an R extraction in a less populated bin is shown in Figure 4.20.

Once R is extracted, the gluon GPD is defined as the square-root of the normalized longitudinal differential cross-section:

$$|\langle H_g \rangle|(t) \propto \sqrt{\frac{d\sigma_L}{dt}(t_{min} - t) / \frac{d\sigma_L}{dt}(0)} \quad (4.18)$$

This normalization of the cross-section to the $t = t_{min}$ point simplifies the analysis and

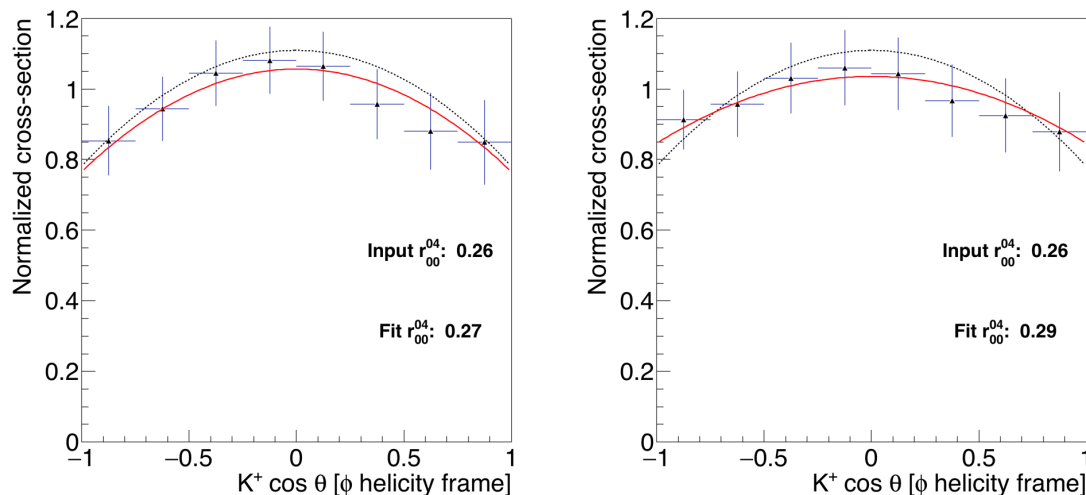


Figure 4.19: A fit to the $\cos(\theta)$ distribution of the K^+ in the reconstructed ϕ -helicity frame within a bin of values $[0.02 < t_{min} - t < 0.04 \text{ GeV}^2]$, $[0.025 < x_V < 0.05]$, and $[1.5 < Q^2 < 2.0 \text{ GeV}^2]$. This is an example of an extraction for an intermediate occupancy bin which is calculated to have a few hundred events during the run period. The dashed line shows the distribution that was generated. The data are then fitted after acceptance and resolution smearing for comparison to the generated values. Uncertainty on the parameter r_{00}^{04} for the fit on both panels is 0.03 (just over 10%). The left plot assumes a momentum resolution of 5% for the ALERT detection of ${}^4\text{He}$, and the right plot assumes a momentum resolution of 10% .

cancels some of the systematic effects that would otherwise increase the uncertainty. As an example, consider the gluon transverse density profile is shown in Figure 4.22 which is a result of the Hankel transform (2.3). The extraction is performed on the simulated events with all acceptance, smearing, and background effects included. The binning choice reflects that of the example extraction performed above for DVCS: x_{Vp} between 0.18 and 0.25, with an additional Q^2 cut between 2.0 and 3.0 GeV^2 . A second transformation is performed on the generated cross-section before any acceptance or resolution effects. The difference between this pre-acceptance/smearing transformation and the post acceptance/smearing transformation is used to estimate the total systematic uncertainty on the transverse profile calculation. The combined systematic and statistical uncertainty is shown in the width of the band for the gluon density calculation in Figure 4.22.

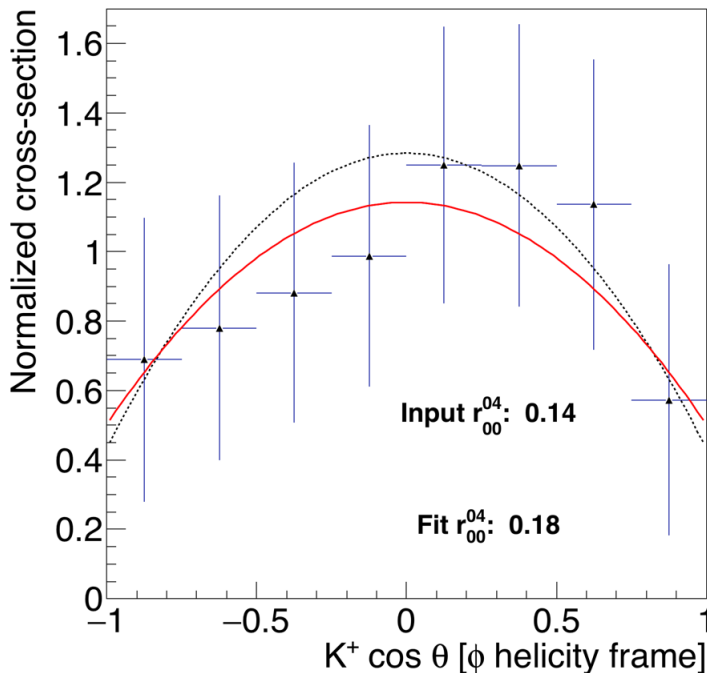


Figure 4.20: A fit to the $\cos(\theta)$ distribution of the K^+ in the reconstructed ϕ -helicity frame within a bin of values $[0.1 < t_{min} - t < 0.15 \text{ GeV}^2]$, $[0.04 < x_V < 0.07]$, and $[3.0 < Q^2 < 4.0 \text{ GeV}^2]$. This is a low occupancy bin, expected to have around 100 events over the run period, and is shown for comparison to the high statistics fit from Figure 4.19. The dashed line shows the distribution that was generated. The data are then fitted after acceptance and resolution smearing for comparison to the generated values. Uncertainty on the parameter r_{00}^{04} for the fit shown above is 0.08 (just under 50%). An ALERT detector momentum resolution of 10% is assumed.

4.3 Parton Distributions in the Transverse plane

Using equation (2.3) the quark and gluon transverse density profiles of ^4He are extracted from the GPDs H_A and H_g , respectively. Projections are shown in Figure 4.21 and Figure 4.22.

The projected uncertainties on the quark density profiles shown in Figure 4.21 were determined using the statistical uncertainties on \mathcal{H}_A (see Figure 4.13). The uncertainties on the density profiles are calculated by varying the extracted t -dependent GPD within the projected uncertainties. The red lines on Figure 4.21 represent the density profiles extracted from the model.

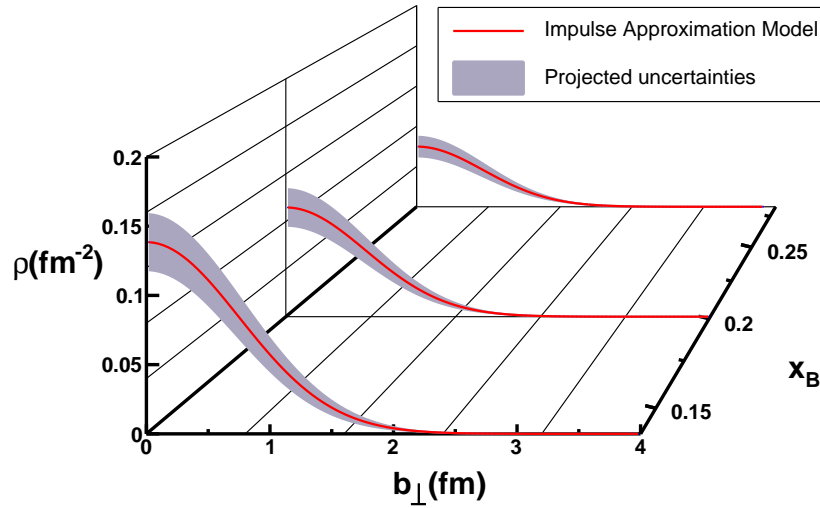


Figure 4.21: The statistical uncertainties of the parton density profiles as a function of the impact parameter, b_{\perp} , based on the \mathcal{H}^A CFF extracted from the Impulse Approximation (IA) at the mean x_B values in the different bins.

An noteworthy feature of the 2-dimensional Fourier transform is the low- b sensitivity to the high- t part of the GPDs. That is, higher momentum transfers are more sensitive to smaller distances. Investigating the location of the first diffractive minimum in F_C for ${}^4\text{He}$ is important for the discussion of the comparison between charge and gluon densities. The requested beam-time for this experiment provides just the required statistics to quantitatively discern the location of the first diffractive minimum, if it exists, within the t range available. Figure 4.23 shows the expected $\sqrt{t_{min} - t}$ spectrum for the gluon profile extraction, with uncertainties that reflect statistics and systematics after all acceptance and resolution smearing and the same binning used to extract the gluon density in Figure 4.22 above: $0.18 < x_{Vp} < 0.25$, and $2.0 < Q^2 < 3.0 \text{ GeV}^2$. The red line shows a fit used to find the diffractive minimum. Fewer statistics would still allow a high precision gluonic RMS radius calculation, where low- t events are most important. Higher statistics would allow us to better locate a diffractive minimum if additional nuclear effects reduce the sharpness of the minimum.

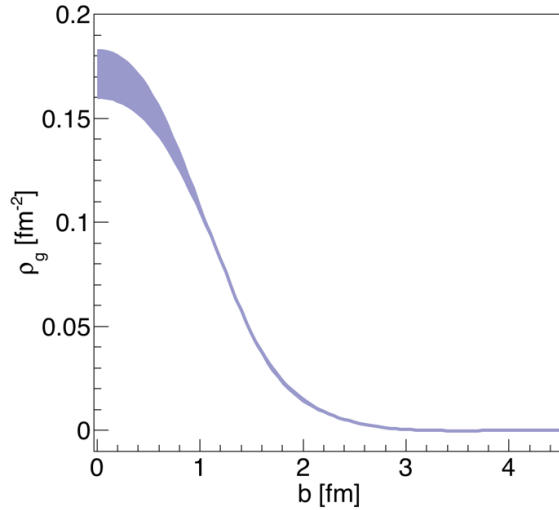


Figure 4.22: An example of the calculated average gluon density for an x_{Vp} bin between 0.18 and 0.25, and a Q^2 bin between 2.0 and 3.0 GeV^2 . The band represents the combined statistical and systematic uncertainties.

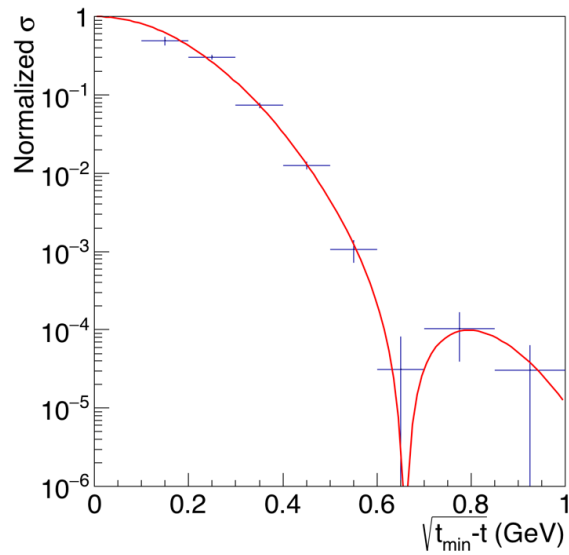


Figure 4.23: The normalized cross-section as a function of $\sqrt{t_{min} - t}$ for an x_{Vp} bin between 0.18 and 0.25, and a Q^2 bin between 2.0 and 3.0 GeV^2 . Total running time for this experiment provides adequate statistics to locate the first diffractive minimum if it exists from ϕ production within ALERT t acceptance. The graph points have uncertainties that include all statistical and resolution/bin-smearing effects. The red line is a fit to the graph with a similar form of $|F_C|^2$ for the ${}^4\text{He}$ nucleus.

Summary and Answers to PAC44

Answers to PAC44 issues

Issues:

The Drift Chamber/scintillator technology needs to be demonstrated. We observe that a strong program of prototype studies is already underway.

Answer: We feel the technology has no major unknowns, wire chambers and scintillators have been used for decades as detectors of low energy nuclei and their properties have been well established. We present in the proposal a conceptual design demonstrating the feasibility of the detector, it is common practice to work on the optimization of a certain number of parameters after the proposal is approved. In particular, because it is easier to fund and man a project that has an approved status than a future proposal. Nevertheless, we remain open to discuss the topic in more depth if the committee has any concerns.

The TAC report voiced concerns about the length of the straw cell target and the substantial effort needed to integrate the DAQ for this detector into the CLAS12 DAQ.

Answer: The TAC and PAC44 raised concerns about the target cell. We have added extra discussion in section 3.3.3, which includes a table of existing or planned targets that are similar to the one we proposed. In summary, our proposed target is twice as wide as the ones used in the 6 GeV era for the BONuS and eg6 run and should therefore cause no issues. Note that the experiment 12-06-113 (BONuS12) is approved with a longer and thinner target. Their design will be reviewed by JLab for their experiment readiness review (ERR) before the PAC45 meeting. The result of this review should settle the question, but in any case, we propose a safer solution based on the successful experiments of the 6 GeV era.

The TAC and PAC44 raised issues regarding integration of ALERT into the CLAS12 DAQ. First, they raised a concern that the resources necessary for this integration are not clearly identified. We have added text in section 3.6.3 outlining the resources provided by each group and the technical support they are expected to provide. Secondly, they mentioned a concern about the “substantial effort needed to integrate the DAQ for this detector into the CLAS12 DAQ”. We want to emphasize that the read-out systems for ALERT are already being used in the CLAS12 DAQ to readout Micromegas detectors. Therefore, we will use and build on the experience gained from these systems.

The proposal does not clearly identify the resources (beyond generic JLAB/CLAS12 effort) necessary for DAQ integration which may be a substantial project.

Answer: As mentioned above, we do not feel this contribution is major, nevertheless we made this part clearer in the proposal.

During review the collaboration discovered an error in converting the luminosity to beam current. This resulted in a revision that will either require doubling the current or the target density. The beam current change would require changes to the Hall B beam dump, while raising the target density could impact the physics reach of the experiment by raising the minimum momentum threshold.

Answer: During the PAC44 proposal submission process the wrong beam current was requested. It was a factor of 2 too low. This increased beam current brought into contention the issue of possible Hall B beam current limits. We chose to use the higher beam current in this new version. Based on discussions with the Hall-B and accelerator staff, the only necessary upgrade necessary to run at 1 μ A is with the Hall-B beam blocker.

The precise interplay between final state interactions (FSI) and the tails of the initial state momentum distribution in DVCS on ^4He was a topic of some debate. The collaboration makes an argument that the excellent acceptance of the apparatus allows novel constraints that allow selection of kinematic ranges where FSI is suppressed. While the originally suggested method to unambiguously identify areas of FSI was revised during the review, the committee remains unconvinced that the new kinematic selections suggested do not also cut into interesting regimes for the initial state kinematics. The committee believes that this is model dependent and would like to see more quantitative arguments than were provided in this version of the proposal.

Answer: We acknowledge there was an overstatement of the possibilities of the Tagged-DVCS proposal on this topic, this has been corrected. We now show a reduction, in opposition to the complete suppression previously claimed, in events that differ from the PWIA result. This finding is based on a simulation using a simple model of FSIs together with a Monte-Carlo event generator.

Summary:

The committee was generally enthusiastic about the diverse science program presented in this proposal; in particular the tagged EMC studies and the unique study of coherent GPD's on the ^4He nucleus. However, the substantial modifications made in the proposal during review indicate that it could be substantially improved on a reasonably short time scale. We would welcome a new proposal that addresses the issues identified by the committee and by the collaboration.

Answer: We hope that the new proposals will answer all the questions raised by the PAC44 and will make the physics case even more compelling.

We also note that there are multiple experiments, proposed and approved, to study the EMC effect, including several with novel methods of studying the recoil system. We appreciate the comparisons of recoil technologies in this proposal and would welcome a broader physics discussion of how the proposed measurements contribute to a lab-wide strategy for exploring the EMC effect.

Answer: While no strategy document has been drafted after them, we want to point out to the PAC that the community of physicist interested by the partonic structure of nuclei meets regularly, with often a large focus on what can be done at JLab (see workshops at Trento¹, Miami², MIT³, and Orsay⁴ for example). Nonetheless, we added in the tagged EMC proposal summary an extension about the 12 GeV approved experiments related to the EMC effect. This short annex will hopefully clarify the context and the uniqueness of the present experiments.

¹New Directions in Nuclear Deep Inelastic Scattering <http://www.ectstar.eu/node/1221>

²Next generation nuclear physics with JLab12 and EIC <https://www.jlab.org/indico/event/121/>

³Quantitative challenges in EMC and SRC Research and Data-Mining http://web.mit.edu/schmidta/www/src_workshop/

⁴Partons and Nuclei <https://indico.in2p3.fr/event/14438/>

Summary and Beam Time Request

We are proposing an experimental program that will provide data, for the first time, required for a global analysis that will extract partonic GPDs in a dense nucleus, in this case GPD $H_{4\text{He}}$ for both quarks and gluons together in ^4He . The DVCS process has been the hallmark of the 3-D investigation of the nucleon structure at large x at Jefferson Lab. This investigation was extended successfully to the ^4He nucleus in the 6 GeV era albeit with limited kinematic leverage and statistics. This proposal will not only provide Compton form factors for the quarks contributions but also uses the electroproduction of ϕ to explore the contribution of gluons at large x , in tandem with that of the quarks.

This program will be a precursor of physics to be explored at a future EIC, namely 3-D imaging of spin zero nuclei. Other mesons will be accessible in the same data stream of this proposed experiment extending the physics reach of this proposal. For example, a flavor decomposition of these form factors will be possible by investigating the deep exclusive production of pseudoscalar and vector mesons with masses below the ϕ meson, like π^0 , ρ , ω . Given the limited energy reach of Jefferson Lab, the most promising access to the gluonic structure of nucleon and nuclei is by using the ϕ meson production as a probe as was done in proposal E12-12-007. Of course a future EIC will allow the use of heavier mesons such as the J/Ψ and the Υ for a "cleaner" gluonic probe, nevertheless we believe that at large x the strange quark contribution could be separated from that of the gluons in a global analysis where DVCS and DVMP data from different pseudoscalar and vector mesons, thus this coherent proposal.

In order to achieve the statistical uncertainties presented in this proposal, we request 20 days of running with 11 GeV electron beam at a luminosity of $3 \times 10^{34} \text{ cm}^{-2}\text{s}^{-1}$ per nucleon (same beam time request as the tagged EMC proposal) and 10 days at $6 \times 10^{34} \text{ cm}^{-2}\text{s}^{-1}$ per nucleon with helium target (specific to this proposal), both with 80% longitudinally polarized beam. We will also need 5 days of commissioning of the ALERT detector at 2.2 GeV with helium and hydrogen targets.

Relation to other proposals

Our proposal has no direct relation to other approved proposals, except that similar measurements have been proposed and approved for the proton. These are the first coherent DVCS and DVMP measurements that are proposed for a ^4He target.

Appendix A

Twist-2 $e^4He \rightarrow e^4He \gamma$ cross section

Following the definitions of reference [32], the variables that appear in equations 2.9 to 2.11 are defined as:

$\mathcal{P}_1(\phi)$ and $\mathcal{P}_2(\phi)$ are BH propagators and defined as:

$$\mathcal{P}_1(\phi) = \frac{(k - q')^2}{Q^2} = -\frac{1}{y(1 + \varepsilon^2)} [J + 2K \cos(\phi)] \quad (\text{A.1})$$

$$\mathcal{P}_2(\phi) = \frac{(k - \Delta)^2}{Q^2} = 1 + \frac{t}{Q^2} + \frac{1}{y(1 + \varepsilon^2)} [J + 2K \cos(\phi)] \quad (\text{A.2})$$

with,

$$J = \left(1 - y - \frac{y\varepsilon^2}{2}\right) \left(1 + \frac{t}{Q^2}\right) - (1 - x_A)(2 - y) \frac{t}{Q^2} \quad (\text{A.3})$$

$$K^2 = -\delta t (1 - x_A) \left(1 - y - \frac{y^2\varepsilon^2}{4}\right) \left\{ \sqrt{1 + \varepsilon^2} + \frac{4x_A(1 - x_A) + \varepsilon^2}{4(1 - x_A)} \delta t \right\} \quad (\text{A.4})$$

$$\delta t = \frac{t - t_{min}}{Q^2} = \frac{t}{Q^2} + \frac{2(1 - x_A) \left(1 - \sqrt{1 + \varepsilon^2}\right) + \varepsilon^2}{4x_A(1 - x_A) + \varepsilon^2} \quad (\text{A.5})$$

where t_{min} represents the kinematic boundary of the process and defined as:

$$t_{min} = -Q^2 \frac{2(1 - x_A)(1 - \sqrt{1 + \varepsilon^2}) + \varepsilon^2}{4x_A(1 - x_A) + \varepsilon^2} \quad (\text{A.6})$$

The Fourier coefficients, in equations 2.9, 2.10 and 2.11, of a spin-0 target are defined as:

$$c_0^{BH} = \left[\left\{ (2-y)^2 + y^2(1+\varepsilon^2)^2 \right\} \left\{ \frac{\varepsilon^2 Q^2}{t} + 4(1-x_A) + (4x_A + \varepsilon^2) \frac{t}{Q^2} \right\} + 2\varepsilon^2 \left\{ 4(1-y)(3+2\varepsilon^2) + y^2(2-\varepsilon^4) \right\} - 4x_A^2(2-y)^2(2+\varepsilon^2) \frac{t}{Q^2} + 8K^2 \frac{\varepsilon^2 Q^2}{t} \right] F_A^2(t) \quad (\text{A.7})$$

$$c_1^{BH} = -8(2-y)K \left\{ 2x_A + \varepsilon^2 - \frac{\varepsilon^2 Q^2}{t} \right\} F_A^2(t) \quad (\text{A.8})$$

$$c_2^{BH} = 8K^2 \frac{\varepsilon^2 Q^2}{t} F_A^2(t) \quad (\text{A.9})$$

where $F_A(t)$ is the electromagnetic form factor of the ^4He . At leading twist, the $|\mathcal{T}_{DVCS}|^2$ writes as a function of only one CFF according to

$$c_0^{DVCS} = 2 \frac{2-2y+y^2+\frac{\varepsilon^2}{2}y^2}{1+\varepsilon^2} \mathcal{H}_A \mathcal{H}_A^* \quad (\text{A.10})$$

and the interference amplitude coefficients are written as:

$$s_1^{INT} = F_A(t) \Im m(\mathcal{H}_A) S_{++}(1), \quad (\text{A.11})$$

with

$$S_{++}(1) = \frac{-8K(2-y)y}{1+\varepsilon^2} \left(1 + \frac{1-x_A + \frac{\sqrt{1+\varepsilon^2}-1}{2}t - t_{min}}{1+\varepsilon^2} \frac{t-t_{min}}{Q^2} \right) \cdot F_A(t) \quad (\text{A.12})$$

$$c_0^{INT} = F_A(t) \Re e(\mathcal{H}_A) C_{++}(0), \quad (\text{A.13})$$

with

$$C_{++}(0) = \frac{-4(2-y)(1+\sqrt{1+\varepsilon^2})}{(1+\varepsilon^2)^2} \left\{ \frac{\widetilde{K}^2(2-y)^2}{Q^2 \sqrt{1+\varepsilon^2}} + \frac{t}{Q^2} \left(1 - y - \frac{\varepsilon^2}{4} y^2 \right) (2-x_A) \left(1 + \frac{2x_A(2-x_A + \frac{\sqrt{1+\varepsilon^2}-1}{2} + \frac{\varepsilon^2}{2x_A}) \frac{t}{Q^2} + \varepsilon^2}{(2-x_A)(1+\sqrt{1+\varepsilon^2})} \right) \right\} \quad (\text{A.14})$$

$$c_1^{INT} = F_A(t) \Re e(\mathcal{H}_A) C_{++}(1), \quad (\text{A.15})$$

with

$$\begin{aligned}
C_{++}(1) &= \frac{-16K(1-y+\frac{\varepsilon^2}{4}y^2)}{(1+\varepsilon^2)^{5/2}} \left\{ \left(1 + (1-x_A) \frac{\sqrt{1+\varepsilon^2}-1}{2x_A} + \frac{\varepsilon^2}{4x_A} \right) \frac{x_A t}{Q^2} - \frac{3\varepsilon^2}{4.0} \right\} \\
&- 4K \left(2 - 2y + y^2 + \frac{\varepsilon^2}{2}y^2 \right) \frac{1 + \sqrt{1+\varepsilon^2} - \varepsilon^2}{(1+\varepsilon^2)^{5/2}} \left\{ 1 - (1-3x_A) \frac{t}{Q^2} \right. \\
&\quad \left. + \frac{1 - \sqrt{1+\varepsilon^2} + 3\varepsilon^2 x_A * t}{1 + \sqrt{1+\varepsilon^2} - \varepsilon^2} \frac{t}{Q^2} \right\}
\end{aligned} \tag{A.16}$$

Appendix B

Projections using Bethe-Heitler cross sections

As it has been shown in equation 2.8, the amplitude of the photon-leptoproduction cross section is decomposed into three terms: the pure DVCS scattering amplitude (\mathcal{T}_{DVCS}), the pure BH amplitude (\mathcal{T}_{BH}), and the interference amplitude ($\mathcal{I}_{BH^*DVCS}^\lambda$). Within the accessible phase-space of JLAB, the measured cross section is mostly dominant by the well known BH reaction. Herein, we perform an exercise of extracting projections of our results based on generating and simulating pure BH events for the purpose of validating our projection results that were extracted based on the parametrized cross section from CLAS-EG6 experiment.

The statistical error bars that are shown in the following figures were calculated using the same beam time and luminosities listed in section 4.1.2. Figure B.1 shows the kinematical correlations for the reconstructed BH events. For binning the data and extracting the projections, we have performed the same binning that was shown in figure 4.10. Figure B.2 represents the same binning laid over the reconstructed BH events. Figure B.3 shows the reconstructed beam-spin asymmetries as a function of the angle ϕ for two bins in $-t$ at a fixed x_B value presenting a high and a low statistic bins. The projected precision of A_{LU} at ϕ equal to 90° for the different bins is presented in figure B.4. The projected uncertainties on the reconstructed real and imaginary parts of the CFF are shown in figure B.5. Finally, figure B.6 shows the projected uncertainties on the quark density profiles using the statistical error bars on the imaginary part of the ^4He CFF presented in figure B.5.

In summary, this exercise has proven that the parametrized cross section that has been used to extract our projections in section 4.1.2 is valid and our projections are well reproduced, within

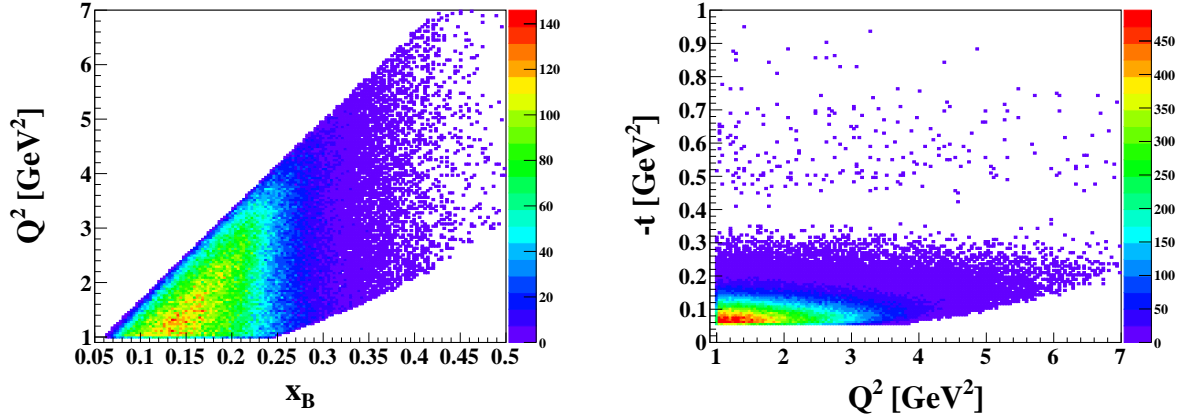


Figure B.1: Correlation between Q^2 and x_B (on the left) and between $-t$ and Q^2 for pure coherent BH off ${}^4\text{He}$.

the statistical error bars, by the well-known pure BH process. The slight differences between the results presented in 4.1.2 and here are associated to the fact that the parametrized cross section was extracted based on real data from CLAS-EG6 that includes both processes, BH and DVCS.

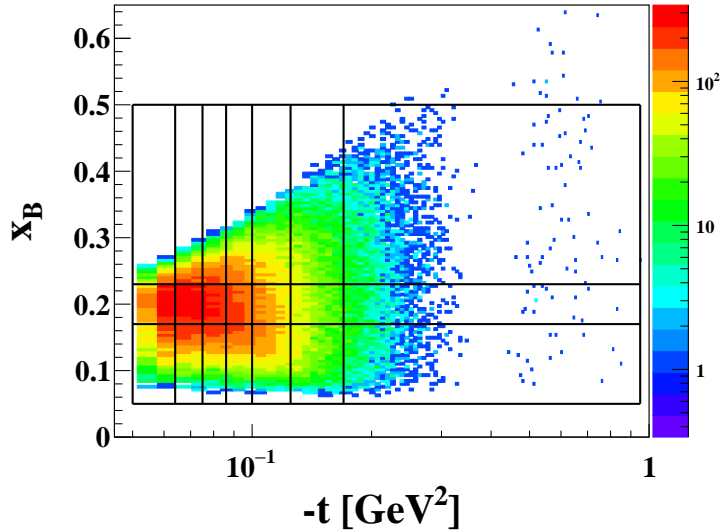


Figure B.2: Data binning in x_B vs $-t$ space for the reconstructed pure coherent BH off ${}^4\text{He}$.

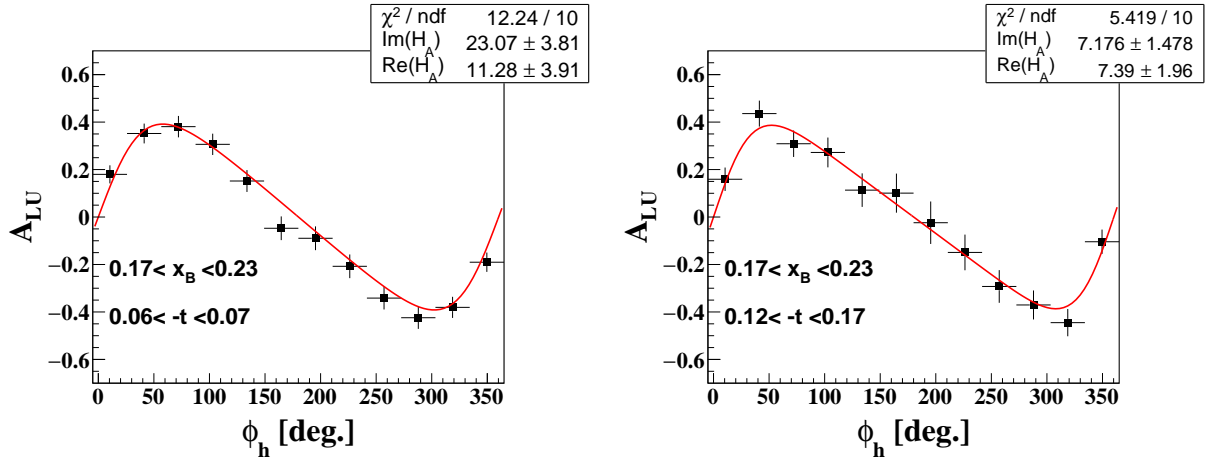


Figure B.3: The coherent beam-spin asymmetry projections as a function of the angle ϕ between the leptonic and the hadronic planes, for two different bins $-t$ at the same x_B range, integrated over Q^2 range. The red solid curves represent a fit to the data in the full form of the asymmetry, equation 2.14, with the real and the imaginary parts of the CFF as the free parameters of the fit.

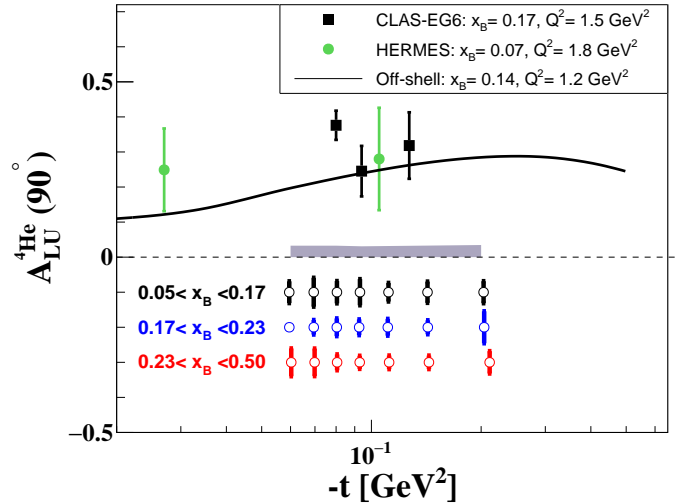


Figure B.4: Projected precision for the $A_{LU}(90^\circ)$, from the fit, for coherent DVCS on ^4He versus $-t$ compared to the previous measurements from CLAS-eg6 (black squares), HERMES (green circles) and spectral function calculations (LT curves).

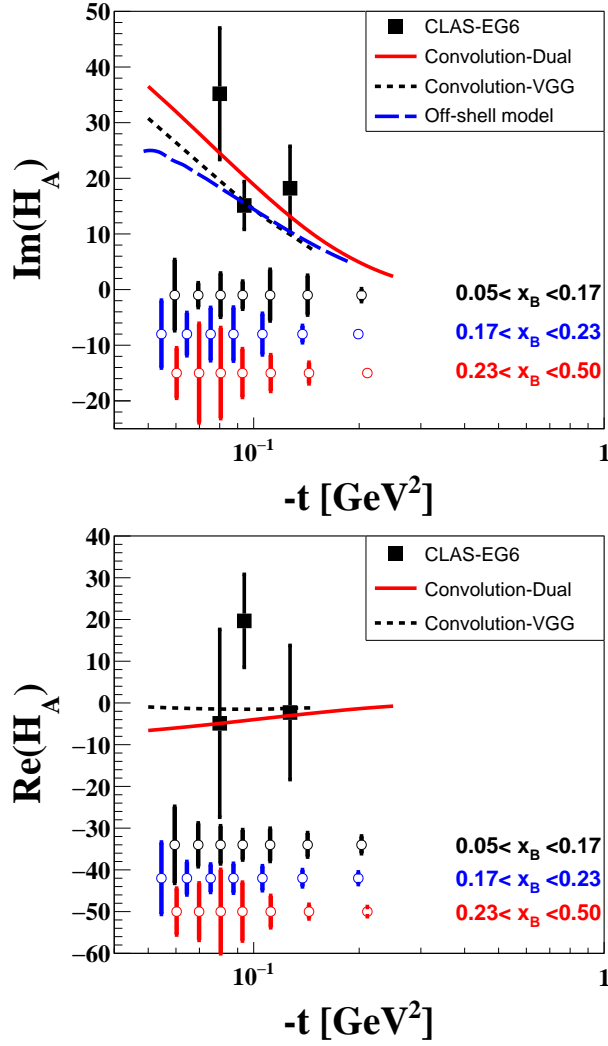


Figure B.5: The projected statistical uncertainties for the imaginary (top) and real (bottom) parts of the CFF H_A , from the fits, as a function of $-t$ at fixed ranges in x_B

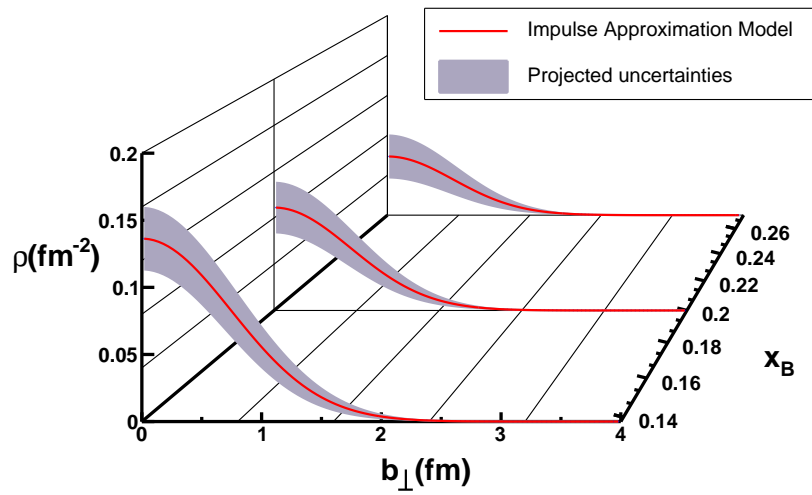


Figure B.6: The statistical uncertainties of the parton density profiles as a function of the impact parameter, b_{\perp} , based on the \mathcal{H}^A CFF extracted from the Impulse Approximation (IA) at the mean x_B values in the different bins.

Bibliography

- [1] J. J. Aubert *et al.*, “The ratio of the nucleon structure functions F_{2_n} for iron and deuterium,” *Phys. Lett.*, vol. B123, pp. 275–278, 1983.
- [2] G. A. Miller and J. R. Smith, “Return of the emc effect.,” *Phys.Rev.*, vol. C65, p. 015211, 2002.
- [3] A. W. Thomas, “New insight into nuclear structure from qcd,” *Annalen Phys*, vol. 13, pp. 731–739, 2004.
- [4] S. Liuti and S. K. Taneja, “Nuclear medium modifications of hadrons from generalized parton distributions,” *Phys. Rev.*, vol. C72, p. 034902, 2005.
- [5] A. H. Rezaeian and H.-J. Pirner, “The nuclear matter stability in a non-local chiral quark model,” *Nucl. Phys.*, vol. A769, pp. 35–52, 2006.
- [6] Z.-m. He, X.-x. Yao, C.-g. Duan, G.-l. Li, and H.-g. Peng, “Double Q^{*2} rescaling model and the nuclear effect of the parton distribution functions,” *Eur. Phys. J.*, vol. C4, pp. 301–306, 1998.
- [7] A. Accardi, D. Grunewald, V. Muccifora, and H. J. Pirner, “Atomic mass dependence of hadron production in deep inelastic scattering on nuclei,” *Nucl. Phys.*, vol. A761, pp. 67–91, 2005.
- [8] A. Accardi, D. Grunewald, V. Muccifora, and H. Pirner, “Erratum: Atomic mass dependence of hadron production in deep inelastic scattering on nuclei,” 2005.
- [9] A. Kirchner and D. Mueller, “Deeply virtual Compton scattering off nuclei,” *Eur. Phys. J.*, vol. C32, pp. 347–375, 2003.
- [10] M. Burkardt, “Impact parameter dependent parton distributions and off-forward parton distributions,” *Phys. Rev.*, vol. D62, p. 071503, 2000.
- [11] M. Diehl, “Generalized parton distributions in impact parameter space,” *Eur.Phys.J.*, vol. C25, pp. 223–232, 2002.
- [12] A. V. Belitsky and D. Mueller, “Nucleon hologram with exclusive lepton production,” *Nucl. Phys.*, vol. A711, pp. 118–126,, 2002.

- [13] M. Burkardt, “Transverse deformation of parton distributions and transversity decomposition of angular momentum,” *Phys. Rev.*, vol. D72, p. 094020, 2005.
- [14] M. Hattawy *et al.* (EG6 Working Group), “Deeply Virtual Compton Scattering off ^4He ,” *CLAS internal analysis note*, 2016.
- [15] M. V. Polyakov, “Generalized parton distributions and strong forces inside nucleons and nuclei,” *Phys. Lett.*, vol. B555, pp. 57–62, 2003.
- [16] J. Gomez *et al.*, “Measurement of the A-dependence of deep inelastic electron scattering,” *Phys.Rev.*, vol. D49, pp. 4348–4372, 1994.
- [17] F. E. Close, R. G. Roberts, and G. G. Ross, “The Effect of Confinement Size on Nuclear Structure Functions,” *Phys. Lett.*, vol. B129, p. 346, 1983.
- [18] O. Nachtmann and H. J. Pirner, “Color Conductivity in Nuclei and the EMC Effect,” *Z. Phys.*, vol. C21, p. 277, 1984.
- [19] R. L. Jaffe, F. E. Close, R. G. Roberts, and G. G. Ross, “On the Nuclear Dependence of Electroproduction,” *Phys. Lett.*, vol. B134, p. 449, 1984.
- [20] F. E. Close, R. G. Roberts, and G. G. Ross, “Factorization Scale Independence, the Connection between Alternative Explanations of the EMC Effect and QCD Predictions for Nuclear Properties,” *Nucl. Phys.*, vol. B296, p. 582, 1988.
- [21] S. Liuti and S. K. Taneja, “Microscopic description of deeply virtual Compton scattering off spin-0 nuclei,” *Phys. Rev.*, vol. C72, p. 032201, 2005.
- [22] V. Guzey and M. Strikman, “DVCS on spinless nuclear targets in impulse approximation,” *Phys. Rev.*, vol. C68, p. 015204, 2003.
- [23] V. Guzey and M. Siddikov, “On the A-dependence of nuclear generalized parton distributions,” *J. Phys.*, vol. G32, pp. 251–268, 2006.
- [24] S. Scopetta, “Generalized parton distributions of He-3,” *Phys. Rev.*, vol. C70, p. 015205, 2004.
- [25] F. X. Girod, M. Guidal, A. Kubarovsky, V. Kubarovsky, P. Stoler, C. Weiss, *et al.* Proposal to Jefferson Lab PAC39, Exclusive Phi Meson Electroproduction with CLAS12: PR12-12-007, 2012.
- [26] A. Accardi *et al.*, “Electron Ion Collider: The Next QCD Frontier - Understanding the glue that binds us all,” 2012.
- [27] A. V. Belitsky and A. V. Radyushkin, “Unraveling hadron structure with generalized parton distributions,” *Phys. Rept.*, vol. 418, pp. 1–387, 2005.
- [28] M. Burkardt, “Impact parameter space interpretation for generalized parton distributions,” *Int. J. Mod. Phys.*, vol. A18, pp. 173–208, 2003.

- [29] M. Guidal, H. Moutarde, and M. Vanderhaeghen, “Generalized Parton Distributions in the valence region from Deeply Virtual Compton Scattering,” *Rept. Prog. Phys.*, vol. 76, p. 066202, 2013.
- [30] R. F. Frosch, J. S. McCarthy, R. E. Rand, and M. R. Yearian, “Structure of the he^4 nucleus from elastic electron scattering,” *Phys. Rev.*, vol. 160, pp. 874–879, Aug 1967.
- [31] A. L. H. A. C. Camsonne, “Jlab measurement of the 4He charge form factor at large momentum transfers,” *Phys. Rev. Lett.*, vol. 112, p. 132503, Apr 2014.
- [32] A. V. Belitsky and D. Mueller, “Refined analysis of photon leptonproduction off spinless target,” *Phys. Rev.*, vol. D79, p. 014017, 2009.
- [33] A. Airapetian *et al.*, “Nuclear-mass dependence of azimuthal beam-helicity and beam-charge asymmetries in deeply virtual Compton scattering,” *Phys. Rev.*, vol. C81, p. 035202, 2010.
- [34] M. Mazouz *et al.*, “Deeply Virtual Compton Scattering off the neutron,” *Phys. Rev. Lett.*, vol. 99, 2007.
- [35] A. V. Belitsky, D. Mueller, A. Kirchner, and A. Schafer, “Twist-three analysis of photon electroproduction off pion,” *Phys. Rev.*, vol. D64, p. 116002, 2001.
- [36] V. Guzey, “Neutron contribution to nuclear DVCS asymmetries,” *Phys. Rev.*, vol. C78, p. 025211, 2008.
- [37] M. Guidal, M. V. Polyakov, A. V. Radyushkin, and M. Vanderhaeghen, “Nucleon form-factors from generalized parton distributions,” *Phys. Rev.*, vol. D72, p. 054013, 2005.
- [38] J. O. Gonzalez-Hernandez, S. Liuti, G. R. Goldstein, and K. Kathuria, “Interpretation of the flavor dependence of nucleon form factors in a generalized parton distribution model,” *Phys. Rev. C*, vol. 88, p. 065206, Dec 2013.
- [39] A. Aktas *et al.*, “Measurement of event shape variables in deep-inelastic scattering at HERA,” *Eur. Phys. J.*, vol. C46, pp. 343–356, 2006.
- [40] S. V. Goloskokov and P. Kroll, “The Role of the quark and gluon GPDs in hard vector-meson electroproduction,” *Eur. Phys. J.*, vol. C53, pp. 367–384, 2008.
- [41] M. Diehl, W. Kugler, A. Schafer, and C. Weiss, “Exclusive channels in semi-inclusive production of pions and kaons,” *Phys. Rev.*, vol. D72, p. 034034, 2005. [Erratum: *Phys. Rev.*D72,059902(2005)].
- [42] L. Favart, M. Guidal, T. Horn, and P. Kroll, “Deeply Virtual Meson Production on the nucleon,” 2015.
- [43] K. Schilling and G. Wolf, “How to analyze vector meson production in inelastic lepton scattering,” *Nucl. Phys.*, vol. B61, pp. 381–413, 1973.

- [44] K. Schilling, P. Seyboth, and G. E. Wolf, “On the Analysis of Vector Meson Production by Polarized Photons,” *Nucl. Phys.*, vol. B15, pp. 397–412, 1970. [Erratum: *Nucl. Phys.*B18,332(1970)].
- [45] K. Lukashin *et al.*, “Exclusive electroproduction of phi mesons at 4.2-GeV,” *Phys. Rev.*, vol. C63, p. 065205, 2001.
- [46] J. P. Santoro *et al.*, “Electroproduction of $\phi(1020)$ mesons at $1.4 < Q^2 < 3.8\text{GeV}^2$ measured with the CLAS spectrometer,” *Phys. Rev.*, vol. C78, p. 025210, 2008.
- [47] R. L. Dixon, R. Galik, D. Larson, A. Silverman, M. Herzlinger, S. D. Holmes, F. M. Pipkin, S. Raither, and R. L. Wagner, “Spectrometer study of ϕ meson electroproduction,” *Phys. Rev.*, vol. D19, p. 3185, 1979.
- [48] D. G. Cassel *et al.*, “Exclusive ρ^0 , ω and ϕ Electroproduction,” *Phys. Rev.*, vol. D24, p. 2787, 1981.
- [49] A. Borissov. in Proceedings of Meson 2000 Workshop, Cracow, Poland, May 19 through 23, 2000.
- [50] M. Arneodo *et al.*, “Exclusive rho0 and phi muoproduction at large q^{*2} ,” *Nucl. Phys.*, vol. B429, pp. 503–529, 1994.
- [51] S. Chekanov *et al.*, “Exclusive electroproduction of phi mesons at HERA,” *Nucl. Phys.*, vol. B718, pp. 3–31, 2005.
- [52] F. D. Aaron *et al.*, “Diffractive Electroproduction of rho and phi Mesons at HERA,” *JHEP*, vol. 05, p. 032, 2010.
- [53] “CLAS12 Technical Design Report,” 2008.
- [54] H. Fenker *et al.*, “BoNus: Development and use of a radial TPC using cylindrical GEMs,” *Nucl. Instrum. Meth.*, vol. A592, pp. 273–286, 2008.
- [55] M. Amarian *et al.*, “The Structure of the Free Neutron at Large x-Bjorken (PR12-06-113),” *A proposal to PAC 30*, 2006.
- [56] J. Peyré, B. Genolini, and J. Poutas, “A Full-Scale Prototype for the Tracking Chambers of the ALICE Muon Spectrometer,” 1998.
- [57] T. Abe *et al.*, “Belle II Technical Design Report,” 2010.
- [58] E. Etzion *et al.*, “The Certification of ATLAS Thin Gap Chambers Produced in Israel and China,” 2004.
- [59] S. Biagi, “Monte Carlo simulation of electron drift and diffusion in counting gases under the influence of electric and magnetic fields,” *Nucl. Instrum. Meth.*, vol. A421, pp. 234–240, 1999.

- [60] C. Ciofi degli Atti *et al.*, “The readout system for the clas12 micromegas vertex tracker,” in *2014 19th IEEE-NPSS Real Time Conference*, pp. 1–11, May 2014.
- [61] T. C. Collaboration, “Clas12 forward tagger (ft) technical design report.” <https://www.jlab.org/Hall-B/clas12-web/docs/ft-tdr.2.0.pdf>, 2012. Online; accessed 29 January 2016.
- [62] “Petiroc-2a.” <http://www.weeroc.com/en/products/petiroc-2>. Accessed: 2017-05-15.
- [63] C. Zorn, “A pedestrian’s guide to radiation damage in plastic scintillators,” *Nucl. Phys. Proc. Suppl.*, vol. 32, pp. 377–383, 1993.
- [64] Y. Qiang, C. Zorn, F. Barbosa, and E. Smith, “Radiation Hardness Tests of SiPMs for the JLab Hall D Barrel Calorimeter,” *Nucl. Instrum. Meth.*, vol. A698, pp. 234–241, 2013.
- [65] Y. Qiang, C. Zorn, F. Barbosa, and E. Smith, “Neutron radiation hardness tests of SiPMs,” *AIP Conf. Proc.*, vol. 1560, pp. 703–705, 2013.
- [66] S. Ahmad. Private communication, May 2017. Weeroc SAS.
- [67] K. Emi *et al.*, “Study of a dE/dx measurement and the gas-gain saturation by a prototype drift chamber for the BELLE-CDC,” *Nucl. Instrum. Meth.*, vol. A379, pp. 225–231, 1996.
- [68] S. Stepanyan and A. P. Freyberger. Private communication, May 2017.
- [69] F. X. Girod, *Deeply Virtual Compton Scattering (Beam Spin Asymmetries) for the study of Generalized Parton Distributions*. PhD thesis, Université Louis Pasteur, Strasbourg, France [Institution Report No. DAPNIA-06-18-T], 2006.
- [70] J. M. Grames *et al.*, “Unique electron polarimeter analyzing power comparison and precision spin-based energy measurement,” *Phys. Rev. ST Accel. Beams*, vol. 7, p. 042802, Apr 2004.
- [71] L. N. Hand, “Experimental investigation of pion electroproduction,” *Phys. Rev.*, vol. 129, pp. 1834–1846, 1963.